モザイク型NRD導波路デバイスの最適設計

Doctoral Thesis

Optimal Design of Mosaic-like NRD Guide Devices

Tahir Bashir

Muroran Institute of Technology

March 2023

Contents

Chapter 1

Background

In this chapter, first, we discuss microwave and millimeter-wave band and its applications in our communication system for the motivation. Then, planar and non-planar technologies, its advantages and limitations. After that, we discuss the importance of NRD technology over these technologies. In this chapter, we also review the literature of NRD guide to clarify how distinct our research work from the previous work on NRD technology.

1.1 Research Motivation

Over the last two decades, there has been an incredible increase in the number of new communication systems. Novel solutions have been rapidly developed and deployed in an emerging technology, and the number of potential applications for telecommunication systems has increased dramatically. There are no longer any new systems that can be placed in the traditional RF frequency band because it is almost full. Therefore, it is assumed that new technologies are deployed in the microwave and millimeter-wave bands [1]. The microwaves cover the frequencies from 300 MHz to 30 GHz, while the millimeter-wave cover the range from 30 GHz to around 300 GHz. Many industrial, commercial, and military systems use the microwave spectrum today due to the well-established technology of microwave circuits and systems. However, millimeter waves are gaining attention due to a lack of free, sufficiently large frequency windows in the microwave band, which are required by novel broadband systems.

Furthermore, millimeter waves have some uniquely different and attractive characteristics that set them apart from the RF and microwave regions [2]. The ability

to reuse frequencies, high capacity, high resolution, and quasi-optical propagation are the most significant ones. Compared to the microwave, millimeter wave devices are lighter and smaller. Technology that enables the capability to develop components and integrated circuits that are small in size, compact, and offer low transmission losses is necessary for the practical realization of millimeter-wave systems. Additionally, it should be able to integrate waveguide components into integrated systems, which is typically difficult. Along with technical aspects, commercial considerations are crucial to the application of a given technology [3]. Low manufacturing costs and relatively simple mass production are the most important commercial factors. Several technologies are currently in use that meet some of the above criteria. In general, microwave and millimeter wave technologies can be divided into two categories are planar and non-planar technologies [4]. Microwave integrated circuits, monolithic microwave integrated circuits, and miniaturized hybrid microwave integrated circuits are the three types of planar technologies [5], [6]. They enable the development of integrated circuits. Multi-layer technologies have recently received a lot of attention [7]. Passive components are typically made using the microstrip line, coplanar waveguide, and slot line, as well as their derivatives.

Classical planar technologies were originally designed for microwave circuits. It allows for the simple mounting of circuit elements in series. On the other hand, microstrip line, has high transmission loss, high dispersion, and difficulty of deploying elements. Alternative guiding structures have been proposed as a result of the limitations of microstrip line. The two that are currently most used are slot line and coplanar designs, both of which make it simpler. Planar structures have many advantages in general, including a high degree of integration, ease of mounting active two- and three-port devices, small and compact circuit sizes, and well-established technology. However, planar technologies have a limitation at millimeter waves [4]. Since conducting losses rises and reach high values at frequencies beyond 20 GHz, the loss factors of the guides become intolerably high. Additionally, improperly designed circuits can result in radiation losses, leakage at discontinuities, and substantially degraded circuit characteristics. Metallic rectangular waveguides, groove guides, and coaxial lines are well-known non-planar technologies, but they also have large millimeter-wave conducting losses and are bulky to integrate in

integrated circuits. As a result, they are limited to specific applications requiring a low level of integration. Non-planar technologies based on dielectric guides are gaining popularity as an alternative. Their low transmission losses are one of their main advantages over planar structures. Image guides, inverted strip image guides, and rib image guides are some of the dielectric guides that have been proposed. These guides have been used to design various components and used in a variety of systems. The fundamental disadvantage of the dielectric guides, however, is a very high level of radiation losses at discontinuities and bends. This feature restricts their application to the research field.

This scenario has changed as a result of the development of the non-radiative dielectric waveguide (NRD-guide) [8]. The structure is an H-guide modification [9]. The plate separation of the H-guide and NRD-guide is different. For the NRD-guide and H-guide, the distance is either less than or larger than half a free space wavelength. The majority of the NRD-guide technology development is currently in the research stage. We do our best to investigate the literature of NRD guide as follow.

1.2 Research Status of NRD Guide

Several NRD guide components have been reported so far for microwave and millimeter-wave circuit system applications. At 50 GHz, the dispersion characteristics, transmission loss, coupling coefficient, and measurement setup with several NRD-based circuit components, including T-junction, right angle corner, 90^0 and 180^0 bends, and directional coupler, are reported [8]. An NRD-based T-junction with a dielectric stub and thin metal patches with an output power of around -4 dB at 35 GHz has been proposed [10]. The coupling theory was used to analyze the losses in NRD bends (90^0 and 180^0) at 50 GHz, with bending loss less than 0.3 dB has been presented [11]. Following a detailed examination of operational principles, propagating modes, losses, behavior of transmitting waves in bending structures, practical significance, and the confirmation of NRD as a low-loss guide in [8], [10], [11], the authors proposed several NRD circuit elements at an operating frequency of 35 GHz, including a matched terminator, directional coupler, circulator, beam lead diode, gun diode oscillator, transmitter, and receiver. At 50 GHz, an NRD guide filter, a four-way power divider, and an NRD leaky-wave antenna

were fabricated [12]. In millimeter-wave and terahertz applications, a substrate integrated non-radiative dielectric waveguide (SINRD) for printed circuit boards has been developed [13]. The hybrid planar non-radiative waveguide is presented and confirmed as a building block for millimeter-wave circuits, with an experimental prototype based on hybrid technology that includes active and passive components. This novel technique will be greatly useful in the development of future millimeter-wave integrated circuit systems [14]. Using mode coupling theory, a technique for designing circular and racetrack-shaped NRD guiding ring resonators was successfully devised, and a low loss, small-sized ring resonator with radii less than 3.5 mm was built at 60 GHz with band rejection performance of more than 30 dB [15]. At a frequency of 77 GHz, a new sort of NRD-based directional coupler using two separate NRD guides interconnected with a bridge is presented and fabricated [16]. At 60 GHz, a first tunable liquid crystal filter based on NRD technology is presented, with fractional bandwidth and tunability of 1% and 2.5%, respectively [17]. Furthermore, over the tuning range, the filter insertion loss ranges between 4.9 dB and 6.2 dB.

At 60 GHz, an NRD guide single mixer was developed by combining two types of band-pass filters and insertion losses were measured to be 0.3 dB and 0.5 dB at 59 GHz and 60 GHz, respectively [18]. A flexible transmission line using a high permittivity LSE-NRD guide were proposed at 60 GHz [19]. Due to flexibility in design the developed transmission line has a capability to change in another shape. In order to investigate the loss performance authors, measure the transmission loss of the 180°bend and the S-shaped curve. The NRD guide semiconductor devices were optimized through analysis of the NRD guide beam-lead diode mount using electromagnetic field simulator [20]. In order to confirm the validity of the design technique the developed devices were fabricated and compared the simulation results with fabricated ones at 60 GHz.

NRD based two different types of p-i-n diode devices, including amplitude shift keying switches and phase shift keying switches, at 77 GHz have been reported for radar applications [21]. The developed devices have low insertion loss and isolation about 2.5 dB and 25 dB respectively. In addition, the BPSK modulator have also been developed and tested for use with spread spectrum radar systems in the considered frequency range. An NRD guide-based multi-channel TV signal

distribution system has been developed with a millimeter-wave transmitter and receiver [22]. The development of broadband methods for NRD guide circuit were the main focus. By utilizing them, the distribution test of TV signals with more than 100 channels can be completed successfully. A novel class of integrated high-speed amplitude shift keying (ASK) transceiver based on NRD technology has been developed at 60 GHz [23]. The main focus of the authors was to developed a high speed ASK modulator. In order to show the performance, they tested a pair of NRD-guide transceivers and achieved 400-Mb/s data-transmission. Another NRD based high speed PCM transceiver has been developed and tested and achieved a bit rate of more than 300 Mbps at 60 GHz [24]. A filter-based duplexer using NRD have been proposed for a wireless broad-band asymmetric digital subscriber line at 60 GHz [25]. The isolation and insertion loss between a transmitter and receiver port were measured to be more than 45 dB and 3 dB at 60 GHz. To account for non-symmetric curved sections, a correction factor obtained through experimentation has been used in the theoretical study of the dispersion properties of coupled NRD-guides and the scattering coefficients of NRD guide directional couplers. In the Ka-band, experimental 3 dB and 10 dB NRD-guide couplers were developed [26].

Numerical solution that treats coupled NRD guides terminated in a general reflection coefficient have been developed. The performance of two types of coupled lines which includes series and parallel coupled, in which the input and output ports are on different and same lines respectively. There were provided comparisons between calculated and measured properties. The analysis uses flow diagrams to explain the characteristics of a guide ended in the conditions of the arbitrary port [27]. This kind of coupler is used in filter design [28]. A two-pole bandpass filter with a maximum flat response and a 3 dB bandwidth of 1 GHz at a center frequency of 50 GHz was the first NRD filter to be reported [29]. An alternate design with below-cutoff narrow dielectric strips connecting adjacent resonators in place of the air gaps also achieved satisfactory performance [30]. This kind of filter has been investigated rigorously using a network method and mode matching theory. Experimental findings were compared with numerical examples [31]. The authors designed 3-pole bandpass and bandstop filters with a center frequency of 49.5 GHz using Teflon circular post resonators. The insertion and transmission loss

of bandpass and bandstop filter was measured to be 0.3 dB and 30 dB respectively [32].

Fabricated ring resonators exhibit band rejections as high as 30 dB [31]. This result is much greater than the 15 dB rejection reported for an image line structure [33] because NRD guidance is nonradiative. The theoretical designed of transition between NRD guide to air filled rectangular waveguide were described in [34]. By inserting a thin NiCr film in the E-plane and employing multilayer resistive film [29], matched terminations for NRD guides have been achieved. A return loss of greater than 20 dB from 34 to 36 GHz was attained, which has been found to be more reliable [35]. An NRD-guide circulator operating at 50 GHz has been developed. This fabricated circulator had an insertion loss of less than 0.3 dB and a 20 dB isolation bandwidth of about 2.6 GHz. The circulator was developed using an analysis based on an equivalent circuit model [36]. At the intersection of three dielectric strips inside the circulator, ferrite disc resonators were placed. Making non-reciprocal devices by substituting longitudinally magnetized ferrite for the NRD structure isotropic dielectric is another technique. The dispersion of the first few propagation modes in the structure has been calculated numerically and is shown [37].

For a slot array fed by an NRD waveguide, a set of theoretical design equations and structure has been studied [38], [39]. The metal plates close to the edge of the dielectric strip can be truncated to create an antenna with a simple configuration. A transverse equivalent network was used to analyze that structure and produce a closed-form dispersion relation. For the phase and leakage constants, numerical values have been presented, along with experimental verification [40]-[42]. There have been two rod antennas reported for use with NRD guides [43], [44]. Both achieve impedance and mode matching using a tapered section. The reported gains for a 120 mm length at 9.5 GHz and a 150 mm length at 11.5 GHz were 15.9 dB and 17.8 dB, respectively. A diode implanted on a quartz substrate directly in the guided field E-plane worked as the beam-lead mixer, reported in [43]. The same method used to design the mixer mentioned above has also been used to develop a p-i-n diode pulse modulator [35]. A stripline based gun diode oscillator has been developed [44]. The diode is placed to feed slots etched in the stripline ground planes while the other couples to a dielectric stub that works as a resonator, one slot

couples to the output waveguide. At approximately 10 GHz, the maximum output power obtained was 8.3 mW.

The majority of the research work on NRD guide were presented in millimeter wave band in the frequency range of 35 GHz to 94 GHz. In systems where frequency reuse is critical, the frequency around 60 GHz has been chosen where maximum attenuation has been observed of millimeter waves. Some Japanese designed systems are reported to operate at 50 GHz. As we discussed in the above section from both perspectives, a number of NRD guide devices and circuit components have been designed, fabricated, and used in some practical applications. Additionally, some basic research about the advancement of NRD guide theory has also been presented in the literature. In the evaluation mentioned above, we found that commercially available simulation software is used to design NRD circuit components without using any optimization techniques. Therefore, the performance of most of the NRD devices were not really high and compact in size. In order to achieve the desired properties, modern communication systems require more efficient, high-performance, and compact guide devices, which cannot be achieved without the use of efficient simulation and optimization methods.

After detailed investigation of NRD guide background, we discover that numerical modeling, computations, and optimal design techniques constitute another vast research domain in the area of NRD guides, opening many researcher directions and challenges. By considering this domain, our thesis presents efficient simulation methods and optimal design techniques for the NRD guide devices with the ultimate goal of realizing a high performance compact millimeter-wave circuit. The purpose, scope, and contribution of this thesis on the NRD platform are discussed in the next chapter.

Chapter 2

Non-Radiative Dielectric Waveguide

In this chapter, first, we present a brief introduction of non-radiative dielectric waveguide (NRD guide), operational principle and propagating modes. Then we discuss the advantages and limitations of NRD guide. Finally, we discuss the purpose of our research work and contribution on NRD platform.

2.1 Introduction

NRD guide has been proposed as a millimeter waveguide by T. Yoneyama [8]. The idea behind an NRD-guide is based on the concept that if the waveguide is placed in a region of space where electromagnetic waves cannot exist, undesirable radiation at dielectric waveguide discontinuities can be suppressed. A below-cutoff parallel plate waveguide can be used to create such a space. In addition to be very effective at suppressing radiation in the dielectric waveguide, the cutoff nature of the parallel plate waveguide never even slightly degrades the dielectric waveguide inherent low loss quality. As a result, the NRD-guide can be molded into sharp bends to make compact millimeter wave circuits.

NRD structure consists of a dielectric sandwiched between metal parallel plates with height a and width b as shown in Fig. 2.1. In the traditional parallel plate waveguide, waves whose half wavelength is greater than the plate separation is attenuated and cannot be guided. As a result, the NRD guide plate spacing is less than half of the operating wavelength $\lambda/2$. If the dielectric strip is placed between metal plates, the electromagnetic waves can freely propagate along strip. However, radiated waves can be suppressed by cut-off nature of the parallel plate guide. In general, a propagation loss of millimeter wave in the metal become larger

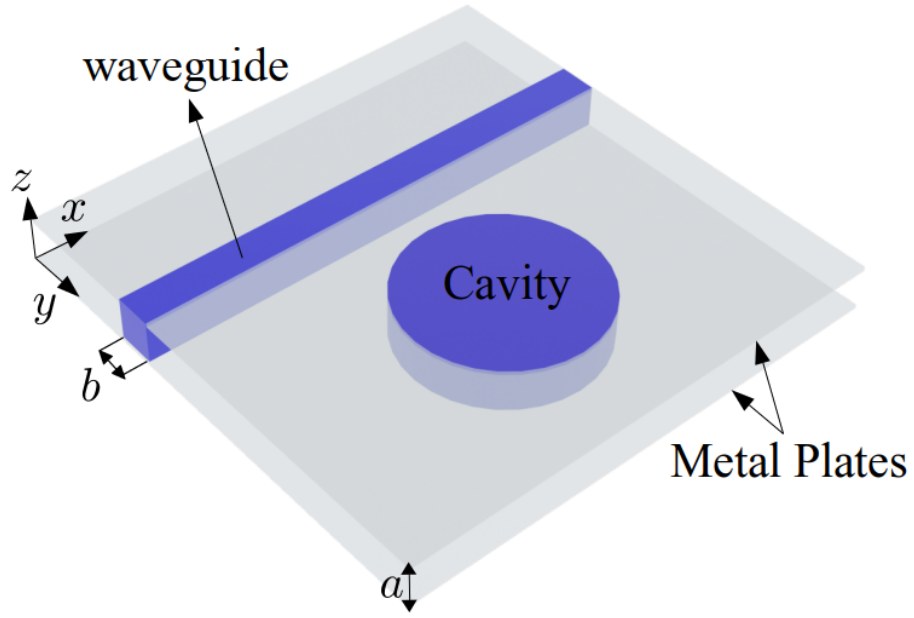

Figure 2.1: Image of NRD guide

compared with that of microwave. However, in the NRD guide, the current flowing through the metal is small, and most of the electromagnetic energy flows through the dielectric. As a result, propagation loss is small. Prior to the development of the NRD guide, the H-guide, a comparable structure, was proposed [20]. Although the H-guide resembles an NRD-guide, the plate spacing is greater than half of the operating wavelength. Although the H-guide has very low transmission losses, its use in actual circuits is severely constrained by the parasitic radiation on bends and discontinuities. When the frequency is raised to a level where the non-radiation requirement $b < \lambda/2$ no longer holds, the NRD guide transforms into the H-guide. Since its invention, a number of modifications to the basic NRD guide structure have been proposed such as asymmetrical grooved NRD guide and hyper NRD or groove NRD guide as shown in Fig. 2.2. The depth of a groove is different in the AGNRD-guide and hyper NRD guide. The spectrum of guided modes is slightly modified as a result of the hyper NRD deeper guide groove than the AGNRD- guide. NRD guides usually support two orthogonal modes. One is LSM_{01} mode whose electric field is parallel to the metal and the other is LSE_{01} mode whose electric field is perpendicular to the metal. Figure 2.3 shows the filed lines of LSM_{01} and LSE_{01} mode. Both modes are non-radiative in nature, cannot propagate within air region

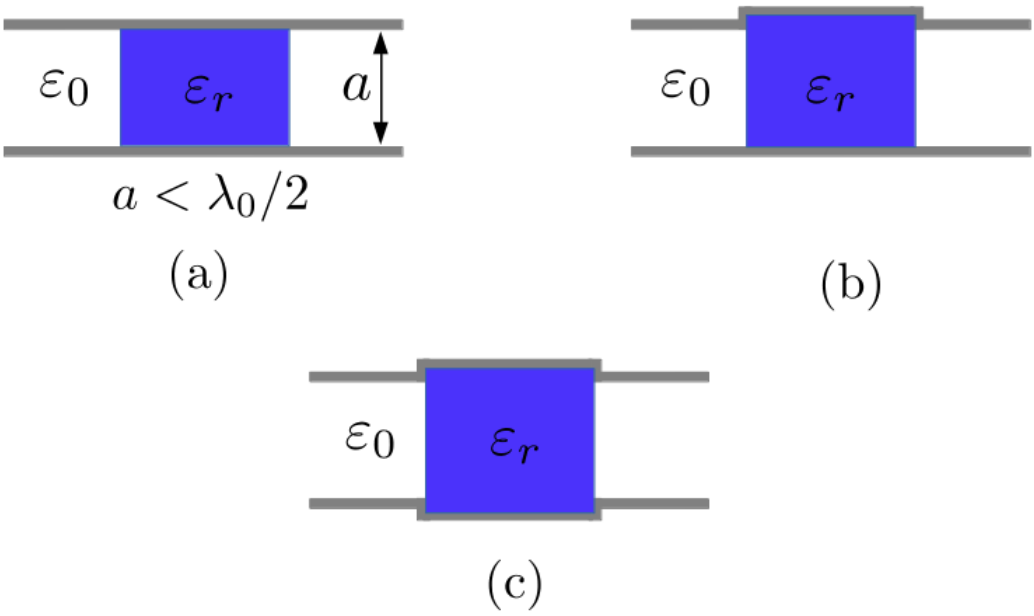

Figure 2.2: Types of non-radiative dielectric waveguide (a) NRD guide (b) AGNRD guide (c) hyper or groove NRD guide

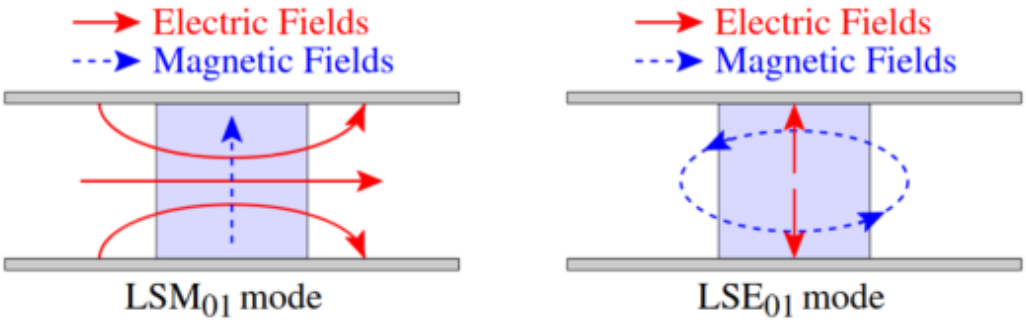

Figure 2.3: Propagating modes in NRD guide

sandwiched metal parallel plates, and can be used as a non-radiative waveguide. LSM$_{01}$ mode whose polarization is parallel to the metal is usually used in NRD guide, in contrasted to microstrip line, which supports polarization perpendicular to the metal.

2.2 Advantages and limitations of NRD Guide

Due to non-radiative nature NRD guide have a several advantages such as no radiation loss at bends and discontinuities due to a parallel plate waveguide cut-off property, the NRD-guide has attracted a lot of interest. Additionally, relatively low transmission loss is experienced. Compared to the similar insulated image guide, the NRD guide is less lossy. Completely integrated circuits that can also readily incorporate NRD-guide structures can be developed using the NRD-guide technology. Moreover, integration with planar technologies such as microstrip line or coplanar waveguide is possible. One can combine the best features of both technologies using this method.

The NRD-guide technology has drawbacks despite its many advantages. The majority of active elements have hybrid connections to NRD-guide elements. When the circuit is not properly designed and the overall circuit parameters are significantly deteriorated, a serious mismatch between an NRD-guide and an active element circuit can occur. But the more fundamental limitation of the technology is caused by the spacing between the metal plates. According to the NRD-guide operation principle, spacing should be less than half of the wavelength. The spacing decreases as the frequency increases. As a result, mounting into the circuit structure at higher frequencies is extremely difficult.

Recently, hybrid technology combining NRD-guide and planar structures has been proposed as a possible solution to overcome the limitations of NRD-guide technology [5]. This solution allows one to take advantage of the best features of both technologies while effectively eliminating their limitations. The planar and NRD-guide structures in this technology share the same ground plane. The planar structure can be developed using a wide range of techniques such as coplanar waveguide, microstrip, or slot line. The aperture coupling connects the planar structures to the NRD-guide components. The transition between a microstrip line and an NRD-guide can be used as an example of a possible coupling structure [45]. The hybrid technology that is being proposed has several attractive advantages. Two sides of the NRD-guide can be employed, allowing the integrated circuits to be as compact as possible. The placement of different circuit components on opposite sides of the NRD-guide allows for almost complete suppression of unwanted cross-talk

and electromagnetic couplings between components. The flexibility of mounting active devices in planar circuit components is another advantage. Furthermore, it is possible to build multilayered, compact, and space saving structures. Recent studies have demonstrated that this technology has the potential in NRD-guided research and development.

2.3 Purpose and Ultimate Goals of Our Research

Several analysis methods have been developed for conventional technologies such as coplanar waveguides, MMIC and microstrip lines and a lot of circuit components have been proposed for microwave and millimeter-wave application by employing these methods. Furthermore, a lot of these techniques have been included into commercially available simulation softwares. On the other hand, the analysis methods for NRD technology are not developed yet properly. The appropriate selection of analysis methods for NRD guide devices is another challenge. The prior analysis methods were originally developed for other guiding structures such as microstrip and coaxial lines, rectangular waveguides, that supports conventional modes like TE, TM, TEM and quasi-TEM modes and these methods are not effective for the analysis of NRD guiding structures. Because NRD supports the hybrid modes such as LSM and LSE modes. A very few analysis methods have been proposed in the literature for the NRD guide components and all these method deals with whole structure and solve 3D problems [46]-[48].

As a result, the numerical cost is very high because the methods require a massive amount of computer memory and computing resources, especially when investigating large or complex 3D problems. Another way to solve this problem is to develop rigorous 2D simulation methods for the 3D structure. Only guiding devices with a consistent structure are capable of it. Thanks to the NRD guide, whose structure is uniform along the perpendicular to the metal parallel plates. The development of highly efficient and accurate simulation methods for NRD-guide technology needs to be developed.

The main purpose of this study is to develop highly efficient simulation methods and the optimal design approaches for NRD guide devices that can be used for all different types of NRD guiding structures. First, we developed 2D simulation methods for NRD guide devices that are highly efficient and accurate. We have

developed a number of highly efficient optimal design approaches for the material distribution in the design region of NRD guide devices. We consider a number of NRD guide devices to demonstrate the usefulness and accuracy of the developed simulation and optimization approaches. Designing a high-performance compact millimeter-wave circuit based on the NRD guide is the ultimate goal of our study. The advantages of our developed simulation and optimization methods are as follows:

- In comparison to 3D methods, our developed 2D simulation methods are highly efficient for the analysis of NRD guides and can be implemented on an average PC, and the computational time is greatly reduced. When compared to 3D simulation methods, the developed methods have a high level of accuracy.

- The developed optimization approaches are highly efficient and can be applied to any type of NRD guide device, regardless of its structure or functionality. On the other hand, they are also useful for broadband operation to obtain the desired broadband property.

- Our developed methods are applicable for 5G and beyond 5G modeling. The results of several optimal devices ensure that our originally developed simulation and optimization methods, and NRD guide devices meet the criteria required for the practical realization of high-performance compact millimeter-wave circuits.

2.4 Organization of the Thesis

The microwave and millimeter-wave bands are briefly discussed in Chapter 1. Other conventional guiding technologies, their limitations, and the advantages of NRD technology over these are discussed. The literature of the NRD guide is also investigated to differentiate our research work from previous work on the NRD platform.

The second chapter introduces the NRD guide, operation principle, and propagating modes. Then the advantages and limitations of the NRD guide are also discussed. Finally, the purpose and ultimate goals of our research work are highlighted in detail.

The detailed formulation of the two-dimensional full vectorial finite element

method for the efficient analysis of NRD guides is presented in chapter three. To confirm the validity of the developed method, the guided mode and propagation analysis is also conducted.

Chapter four discussed the structure representation of NRD guide-based on mosaic optimization concepts. Then the implementation procedure of optimal design approaches, including direct binary search algorithm and genetic algorithm for NRD guide devices are discussed. Finally, the numerical verification of the developed optimization approaches is presented by considering several NRD guide devices.

Chapter five presents the detailed implementation procedure of binary evolutionary approaches for the NRD guide device. The usefulness and comparative study is also conducted by comparing the convergence behavior of optimization approaches by considering several NRD guide devices. The broadband NRD guides are also presented in this chapter. The practical advantages, limitations, and stability analysis of these optimizations are investigated as well.

In chapter six, the two-dimensional full vectorial finite element method is extended for the analysis of non-reciprocal NRD guides using magnetic material. The usefulness and accuracy is confirmed by the numerical simulation of NRD cross-shaped four-port circulator and three-port isolator using Ni-Zn ferrite post.

Chapter seven presents the detailed formulation of rigorous two-dimensional full-vectorial finite difference time domain method for the analysis of NRD guide devices. Numerical verification is confirmed by considering two NRD waveguides. For more verification, the simulation results of these devices using 2D-FV-FDTD are also compared with 2D-FV-FEM.

Chapter eight summarizes the important findings of this research work and thesis. Some future research directions and recommendations are also provided in this chapter.

Chapter 3

Two Dimensional Full Vectorial FEM for NRD Guide

Previous chapters thoroughly discuss the detailed literature review and introduction to the NRD guide. In this chapter, we present the two-dimensional full vectorial finite element method (2D-FV-FEM) for the efficient analysis of NRD guide devices. The basic formulation of NRD guide analysis, vector finite element analysis of NRD guides with mixed edge/node elements, eigenmodes and incident conditions, and the fundamental equation and its solution for LSE mode are all covered in detail in this chapter along with a discussion of the simulation results of NRD guide that is being used for the analysis. The development of high-performance NRD guide devices requires efficient optimization techniques. Without developing a highly efficient simulation method, efficient optimization approaches cannot be realized. For this purpose, we developed an efficient simulation method.

In order to confirm the validity of the originally developed simulation method, we first investigated guided mode analysis of the NRD guide, followed by propagation analysis using the NRD bending waveguide at 60 GHz. We compare the simulation results of 2D-FV-FEM with 3D-FV-FEM to demonstrate the accuracy and efficiency of the presented method, and excellent accuracy is confirmed by the considered device. When compared to 3D-FV-FEM, the developed simulation method can significantly reduce computational efforts and may have enough potential to be coupled with several optimization approaches to obtain an optimal design of NRD guide devices for microwave and millimeter-wave integrated circuit applications using minimal computational resources.

3.1 Basic Formulation for NRD Guide Analysis

We considered a three-dimensional NRD waveguide whose structure is uniform along the z-direction, which is perpendicular to the metal parallel plates and the direction of propagation is in the x and y planes, as illustrated in Fig. 2.1. In a waveguide made of isotropic material, the electric field $\boldsymbol{E}$ and magnetic field $\boldsymbol{H}$ can be represented as follows:

$$\nabla \times \boldsymbol{E} = -j\omega\mu_0\mu_r\boldsymbol{H} \tag{3.1}$$

$$\nabla \times \boldsymbol{H} = -j\omega\varepsilon_0\varepsilon_r\boldsymbol{E} \tag{3.2}$$

where ω is the angular frequency, ε_0 and μ_0 are the permittivity and permeability of vacuum, respectively, ε_0 and μ_r are the relative permittivity and permeability of the material, respectively. The following form can be used to express the electromagnetic field component in the LSM mode:

$$E_x = \phi_x(x,y)\sin\left(\frac{\pi}{a}z\right),\ E_y = \phi_y(x,y)\sin\left(\frac{\pi}{a}z\right),\ E_z = \phi_z(x,y)\cos\left(\frac{\pi}{a}z\right) \tag{3.3}$$

$$H_x = \psi_x(x,y)\cos\left(\frac{\pi}{a}z\right),\ H_y = \psi_y(x,y)\cos\left(\frac{\pi}{a}z\right),\ H_z = \psi_z(x,y)\sin\left(\frac{\pi}{a}z\right) \tag{3.4}$$

Therefore, (3.1) and (3.2) can be as follows:

$$\frac{\partial\phi_z}{\partial y} - \left(\frac{\pi}{a}\right)\phi_y = -j\omega\mu_0\psi_x \qquad \times\cos\left(\frac{\pi}{a}z\right) \tag{3.5}$$

$$\left(\frac{\pi}{a}\right)\phi_x - \frac{\partial\phi_z}{\partial x} = -j\omega\mu_0\psi_y \qquad \times\cos\left(\frac{\pi}{a}z\right) \tag{3.6}$$

$$\frac{\partial\phi_y}{\partial x} - \frac{\partial\phi_x}{\partial y} = -j\omega\mu_0\psi_z \qquad \times\sin\left(\frac{\pi}{a}z\right) \tag{3.7}$$

$$\frac{\partial\psi_z}{\partial y} + \left(\frac{\pi}{a}\right)\psi_y = j\omega\varepsilon_0\varepsilon_r\phi_x \qquad \times\sin\left(\frac{\pi}{a}z\right) \tag{3.8}$$

$$-\left(\frac{\pi}{a}\right)\psi_x - \frac{\partial\psi_z}{\partial x} = j\omega\varepsilon_0\varepsilon_r\phi_y \qquad \times\sin\left(\frac{\pi}{a}z\right) \tag{3.9}$$

$$\frac{\partial\psi_y}{\partial x} - \frac{\partial\psi_x}{\partial y} = j\omega\varepsilon_0\varepsilon_r\phi_z \qquad \times\cos\left(\frac{\pi}{a}z\right) \tag{3.10}$$

From (3.8), (3.9), and (3.10), if we express φ_x and φ_y using ψ_x, ψ_y, and ψ_z, we can obtained

$$\phi_x = -j\frac{1}{\omega\varepsilon_0\varepsilon_r}\left[\frac{\partial\psi_z}{\partial y} + \left(\frac{\pi}{a}\right)\psi_y\right] \tag{3.11}$$

$$\phi_y = -j\frac{1}{\omega\varepsilon_0\varepsilon_r}\left[-\left(\frac{\pi}{a}\right)\psi_x - \frac{\partial\psi_z}{\partial x}\right] \tag{3.12}$$

$$\phi_z = -j\frac{1}{\omega\varepsilon_0\varepsilon_r}\left[\frac{\partial\psi_y}{\partial x} - \frac{\partial\psi_x}{\partial y}\right] \tag{3.13}$$

and substituting (3.11) and (3.12) into (3.7), we obtained

$$\begin{aligned}\frac{\partial}{\partial x}\left(\frac{1}{\varepsilon_r}\frac{\partial\psi_z}{\partial x}\right) + \frac{\partial}{\partial y}\left(\frac{1}{\varepsilon_r}\frac{\partial\psi_z}{\partial y}\right) + k_0^2\psi_z \\ + \left(\frac{\pi}{a}\right)\left\{\frac{\partial}{\partial x}\left(\frac{1}{\varepsilon_r}\psi_x\right) + \frac{\partial}{\partial y}\left(\frac{1}{\varepsilon_r}\psi_y\right)\right\} = 0\end{aligned} \tag{3.14}$$

It would be a basic equation for ordinary two-dimensional TM wave analysis if the final term on the left-hand side of (3.14) were removed. The magnetic fields x and y components are required. In this case, the three-dimensional optical waveguide eigenmode is a hybrid mode, and the scalar wave solution is equivalent to not being able to analyze. Substituting (3.11) and (3.13) into (3.6) gives

$$\frac{\partial}{\partial x}\left(\frac{1}{\varepsilon_r}\frac{\partial\psi_y}{\partial x}\right) - \left(\frac{\pi}{a}\right)^2\frac{1}{\varepsilon_r}\psi_y + k_0^2\psi_y - \frac{\partial}{\partial x}\left(\frac{1}{\varepsilon_r}\frac{\partial\psi_x}{\partial y}\right) - \frac{\pi}{a}\frac{1}{\varepsilon_r}\frac{\partial\psi_z}{\partial y} = 0 \tag{3.15}$$

Substituting (3.12) and (3.13) into (3.5) gives

$$\frac{\partial}{\partial y}\left(\frac{1}{\varepsilon_r}\frac{\partial\psi_x}{\partial y}\right) - \left(\frac{\pi}{a}\right)^2\frac{1}{\varepsilon_r}\psi_x + k_0^2\psi_x - \frac{\partial}{\partial y}\left(\frac{1}{\varepsilon_r}\frac{\partial\psi_y}{\partial x}\right) - \frac{\pi}{a}\frac{1}{\varepsilon_r}\frac{\partial\psi_z}{\partial x} = 0 \tag{3.16}$$

By simultaneously solving (3.14), (3.15), and (3.16), the NRD guide can be analyzed using a two-dimensional vector solution. However, there is some concern about the possibility of spurious solutions in this vector wave analysis formulation using nodal elements of a three-dimensional optical waveguide. As a result, we will formulate vector wave analysis with mixed edge/nodal elements.

3.2 Vector Finite Element Analysis of NRD Guide with Mixed Edge/Nodal Elements

The vector wave equation can be expressed in the following form if the magnetic field is the unknown variable:

$$\nabla\times\left(\frac{1}{\varepsilon_r}\nabla\times\boldsymbol{\Psi}\right) - k_0^2\boldsymbol{\Psi} = \mathbf{0} \tag{3.17}$$

The functional can be written as

$$F = \iiint \left[(\nabla \times \mathbf{\Psi^*}) \cdot \left(\frac{1}{\varepsilon_r} \nabla \times \mathbf{\Psi} \right) - k_0^2 \mathbf{\Psi^*} . \mathbf{\Psi} \right] dV + \iint \left\{ \mathbf{\Psi^*} \times \left(\frac{1}{\varepsilon_r} \nabla \times \mathbf{\Psi} \right) \right\} . \boldsymbol{i}_n dS \quad (3.18)$$

$$= \iiint \left[(\nabla \times \mathbf{\Psi^*}) \cdot \left(\frac{1}{\varepsilon_r} \nabla \times \mathbf{\Psi} \right) - k_0^2 \mathbf{\Psi^*} . \mathbf{\Psi} \right] dV - \iint \left\{ \mathbf{\Psi^*} . \left(\boldsymbol{i}_n \times \frac{1}{\varepsilon_r} \nabla \times \mathbf{\Psi} \right) \right\} dS \quad (3.19)$$

Here $\mathbf{\Psi} = \boldsymbol{H}$, and $\mathbf{\Phi} = \boldsymbol{E}$. Assume, as in the preceding section, that there is no structural variation and the change in the fields z-direction is represented by the trigonometric functions as in (3.3) and (3.4). If the edge/nodal mixed element is used to discretize the analysis domain as depicted in Fig. 3.1. It is possible to write $\mathbf{\Psi}$ and $\nabla \times \mathbf{\Psi}$ as follows:

$$\mathbf{\Psi} = \begin{bmatrix} \Psi_x \\ \Psi_y \\ \Psi_z \end{bmatrix} = \begin{bmatrix} \{U\}^T \cos\left(\frac{\pi}{a} z\right) & \{0\}^T \\ \{V\}^T \cos\left(\frac{\pi}{a} z\right) & \{0\}^T \\ \{0\}^T & \{N\}^T \sin\left(\frac{\pi}{a} z\right) \end{bmatrix} \quad (3.20)$$

$$\nabla \times \mathbf{\Psi} = \begin{bmatrix} 0 & -\partial/\partial z & \partial/\partial y \\ \partial/\partial z & 0 & -\partial/\partial x \\ -\partial/\partial y & \partial/\partial x & 0 \end{bmatrix} \begin{bmatrix} \{U\}^T \cos\left(\frac{\pi}{a} z\right) & \{0\}^T \\ \{V\}^T \cos\left(\frac{\pi}{a} z\right) & \{0\}^T \\ \{0\}^T & \{N\}^T \sin\left(\frac{\pi}{a} z\right) \end{bmatrix} \begin{bmatrix} \{\psi_t\} \\ \{\psi_z\} \end{bmatrix}$$

$$= \begin{bmatrix} \{V\}^T \left(\frac{\pi}{a}\right) \sin\left(\frac{\pi}{a} z\right) & \frac{\partial \{N\}^T}{\partial y} \sin\left(\frac{\pi}{a} z\right) \\ -\{U\}^T \left(\frac{\pi}{a}\right) \sin\left(\frac{\pi}{a} z\right) & -\frac{\partial \{N\}^T}{\partial x} \sin\left(\frac{\pi}{a} z\right) \\ \left(\frac{\partial \{V\}^T}{\partial x} - \frac{\partial \{U\}^T}{\partial y} \right) \cos\left(\frac{\pi}{a} z\right) & \{0\}^T \end{bmatrix} \begin{bmatrix} \{\psi_t\} \\ \{\psi_z\} \end{bmatrix} \quad (3.21)$$

where $\{U\}$, $\{V\}$ are the shape function vectors for edge elements, $\{N\}$ is the shape function vector for nodal elements. Therefore, the generalization

$$(\nabla \times \mathbf{\Psi}^*) \cdot \left(\frac{1}{\varepsilon_r} \nabla \times \mathbf{\Psi} \right) = \begin{bmatrix} \{\psi_t\}^\dagger & \{\psi_z\}^\dagger \end{bmatrix} \begin{bmatrix} [k_{tt}] & [k_{tz}] \\ [k_{zt}] & [k_{zz}] \end{bmatrix} \begin{bmatrix} \{\psi_t\} \\ \{\psi_z\} \end{bmatrix} \quad (3.22)$$

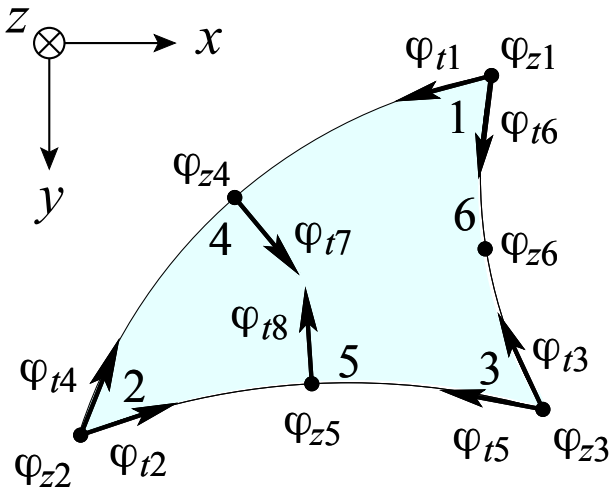

Figure 3.1: Edge/nodal hybrid element with curved boundary

$$
\begin{aligned}
[k_{tt}] &= \frac{1}{\varepsilon_r}\left(\{V\}\{V\}^T + \{U\}\{U\}^T\right)\left(\frac{\pi}{a}\right)^2 \sin^2\left(\frac{\pi}{a}z\right) \\
&\quad + \frac{1}{\varepsilon_r}\left(\frac{\partial\{V\}}{\partial x} - \frac{\partial\{U\}}{\partial y}\right)\left(\frac{\partial\{V\}^T}{\partial x} - \frac{\partial\{U\}^T}{\partial y}\right)\cos^2\left(\frac{\pi}{a}z\right) \\
[k_{tz}] &= \frac{1}{\varepsilon_r}\left(\{V\}\frac{\partial\{N\}^T}{\partial y} + \{U\}\frac{\partial\{N\}^T}{\partial x}\right)\left(\frac{\pi}{a}\right)\sin^2\left(\frac{\pi}{a}z\right) \\
[k_{zt}] &= \frac{1}{\varepsilon_r}\left(\frac{\partial\{N\}}{\partial y}\{V\}^T + \frac{\partial\{N\}}{\partial x}\{U\}^T\right)\left(\frac{\pi}{a}\right)\sin^2\left(\frac{\pi}{a}z\right) \\
[k_{zz}] &= \frac{1}{\varepsilon_r}\left(\frac{\partial\{N\}}{\partial x}\frac{\partial\{N\}^T}{\partial x} + \frac{\partial\{N\}}{\partial y}\frac{\partial\{N\}^T}{\partial y}\right)\sin^2\left(\frac{\pi}{a}z\right)
\end{aligned}
$$

$$
\mathbf{\Psi}^* \cdot \mathbf{\Psi} = \begin{bmatrix} \{\psi_t\}^\dagger & \{\psi_z\}^\dagger \end{bmatrix} \begin{bmatrix} [m_{tt}] & [m_{tz}] \\ [m_{zt}] & [m_{zz}] \end{bmatrix} \begin{bmatrix} \{\psi_t\} \\ \{\psi_z\} \end{bmatrix} \tag{3.23}
$$

$$
\begin{aligned}
[m_{tt}] &= \left(\{U\}\{U\}^T + \{V\}\{V\}^T\right)\cos^2\left(\frac{\pi}{a}z\right) \\
[m_{tz}] &= [0] \\
[m_{zt}] &= [0] \\
[m_{zz}] &= \{N\}\{N\}^T \sin^2\left(\frac{\pi}{a}z\right)
\end{aligned}
$$

The finite element method can be expressed in the following way by performing the volume integral and taking the variation:

$$
\left([K] - k_0^2\,[M]\right)\{\psi\} = \{u\} \tag{3.24}
$$

where $[K]$ and $[M]$ are finite element matrices, and $[u]$ represents the incident conditions.

$$[K] = \begin{bmatrix} K_{tt} & K_{tz} \\ K_{zt} & K_{zz} \end{bmatrix}, [M] = \begin{bmatrix} M_{tt} & 0 \\ 0 & M_{zz} \end{bmatrix} \{\psi\} = \begin{bmatrix} \{\psi_t\} \\ \{\psi_z\} \end{bmatrix}, \{u\} = \begin{bmatrix} \{u_t\} \\ \{u_z\} \end{bmatrix} \quad (3.25)$$

$$[K_{tt}] = \sum_e \iint_e \left[\frac{1}{\varepsilon_r} \left(\{V\}\{V\}^T + \{U\}\{U\}^T \right) \left(\frac{\pi}{a} \right)^2 + \frac{1}{\varepsilon_r} \left(\frac{\partial \{V\}}{\partial x} - \frac{\partial \{U\}}{\partial y} \right) \left(\frac{\partial \{V\}^T}{\partial x} - \frac{\partial \{U\}^T}{\partial y} \right) \right] dxdy \quad (3.26)$$

$$[K_{tz}] = \sum_e \iint_e \left[\frac{1}{\varepsilon_r} \left(\{V\} \frac{\partial \{N\}^T}{\partial y} + \{U\} \frac{\partial \{N\}^T}{\partial x} \right) \left(\frac{\pi}{a} \right) \right] dxdy \quad (3.27)$$

$$[K_{zt}] = \sum_e \iint_e \left[\frac{1}{\varepsilon_r} \left(\frac{\partial \{N\}}{\partial y} \{V\}^T + \frac{\partial \{N\}}{\partial x} \{U\}^T \right) \left(\frac{\pi}{a} \right) \right] dxdy \quad (3.28)$$

$$[K_{zz}] = \sum_e \iint_e \left[\frac{1}{\varepsilon_r} \left(\frac{\partial \{N\}}{\partial x} \frac{\partial \{N\}^T}{\partial x} + \frac{\partial \{N\}}{\partial y} \frac{\partial \{N\}^T}{\partial y} \right) \right] dxdy \quad (3.29)$$

$$[M_{tt}] = \sum_e \iint_e \left[\{U\}\{U\}^T + \{V\}\{V\}^T \right] dxdy \quad (3.30)$$

$$[M_{zz}] = \sum_e \iint_e \{N\}\{N\}^T dxdy \quad (3.31)$$

$$\{u\} = \iint_\Gamma \left\{ \{\boldsymbol{N}\}^* \cdot \left(\boldsymbol{i}_n \times \frac{1}{\varepsilon_r} \nabla \times \boldsymbol{\Psi} \right) \right\} dS \quad (3.32)$$

where Γ is the input boundary. The same equation can be derived from (3.14), (3.15), and (3.16). The absorbing boundary conditions of the perfectly matched layer (PML) are used at the computational domain edge to express a semi-infinite region, $p_i, q_i (i = x, y, z)$, which is defined as follows:

$$p_x = \frac{1}{\varepsilon_r} \cdot \frac{S_x}{S_y}, \quad p_y = \frac{1}{\varepsilon_r} \cdot \frac{S_y}{S_x}, \quad p_z = \frac{1}{\varepsilon_r} \cdot \frac{1}{S_x S_y}$$

$$q_x = \frac{S_y}{S_x}, \quad q_y = \frac{S_x}{S_y}, \quad q_z = S_x S_y$$

where $S_i (i = x, y, z)$ are stretching parameters in the PML region along the i-direction.

3.3 Incident Conditions and Eigenmodes of NRD Guides

To determine the incident conditions, the eigenmode of the uniform waveguide must be determined. We considered an NRD waveguide with structure uniformity

along the x-axis. With the LSM mode propagating in the waveguide at the phase constant β, (3.14).

$$\frac{\partial}{\partial y}\left(\frac{1}{\varepsilon_r}\frac{\partial \psi_z}{\partial y}\right)+\left(\frac{\varepsilon_r k_0^2-\beta^2}{\varepsilon_r}\right)\psi_z+\left(\frac{\pi}{a}\right)\left\{\frac{-j\beta}{\varepsilon_r}\psi_x+\frac{\partial}{\partial y}\left(\frac{1}{\varepsilon_r}\psi_y\right)\right\}=0 \tag{3.33}$$

can be expressed as by taking into account a region with a constant refractive index.

$$\frac{\partial}{\partial y}\left(\frac{1}{\varepsilon_r}\frac{\partial \psi_z}{\partial y}\right)+\left(\frac{\varepsilon_r k_0^2-\beta^2}{\varepsilon_r}\right)\psi_z+\left(\frac{\pi}{a}\right)\frac{1}{\varepsilon_r}\left(-j\beta\psi_x+\frac{\partial \psi_y}{\partial y}\right)=0 \tag{3.34}$$

$$\frac{\partial}{\partial y}\left(\frac{1}{\varepsilon_r}\frac{\partial \psi_z}{\partial y}\right)+\left(k_0^2-\frac{\beta^2+(\pi/a)^2}{\varepsilon_r}\right)\psi_z=0 \tag{3.35}$$

The boundary surface must satisfy the boundary conditions. The following is the eigenvalue equation we obtained by solving (3.35) under boundary condition.

$$\kappa b-2\tan^{-1}\left(\frac{\alpha/\varepsilon_{r,2}}{\kappa/\varepsilon_{r,1}}\right)-m\pi=0$$
$$\left(\kappa=\sqrt{\varepsilon_{r,1}k_0^2-\beta^2},\ \ \alpha=\sqrt{\beta^2-\varepsilon_{r,2}k_0^2}\right) \tag{3.36}$$

where the waveguide dielectric and air regions have corresponding dielectric constants of $\varepsilon_{r,2}$ and $\varepsilon_{r,1}$. The eigenvalue can be obtained by solving (3.36). and the eigenmode amplitude ψ_z can be expressed as follows:

$$\psi_z=\begin{cases} H_0\cos(\kappa(y-y_0)) & (|y-y_0|\le b/2)\\ H_0\cos(\kappa b/2)\exp(-\alpha|y-y_0|) & (|y-y_0|>b/2)\end{cases} \tag{3.37}$$

where H_0 is obtained from the normalization conditions.

$$H_0=\left\{\int_{-\infty}^{\infty}\frac{1}{\varepsilon_r}|\psi_z|^2dy\right\}^{-1/2}=\left\{\frac{2}{\varepsilon_{r,1}}\left(\frac{\sin(\kappa b)}{4\kappa}+\frac{b}{4}\right)+\frac{2}{\varepsilon_{r,2}}\left(\frac{\cos^2(\kappa b/2)}{2\alpha}\right)\right\}^{-1/2} \tag{3.38}$$

After obtaining ψ_z, the following electromagnetic field components are obtained:

$$\psi_x=\frac{1}{j\beta}\left(\frac{\pi}{a}\right)\psi_z \tag{3.39}$$
$$\psi_y=0 \tag{3.40}$$
$$\phi_x=\frac{1}{j\omega\varepsilon_0\varepsilon_r}\frac{\partial \psi_z}{\partial y} \tag{3.41}$$
$$\phi_y=\frac{1}{\omega\varepsilon_0\varepsilon_r\beta}\left\{\left(\frac{\pi}{a}\right)^2+\beta^2\right\}\psi_z \tag{3.42}$$
$$\phi_z=-\frac{1}{j\omega\varepsilon_0\varepsilon_r}\frac{\partial \psi_x}{\partial y}=\frac{1}{\omega\varepsilon_0\varepsilon_r\beta}\left(\frac{\pi}{a}\right)\frac{\partial \psi_z}{\partial y} \tag{3.43}$$

The boundary term on the plane of incidence can be stated using the electric field as follows, presuming that the normal direction is the x-direction:

$$
\begin{aligned}
&\{\boldsymbol{N}\}\cdot\left(\boldsymbol{i}_x\times\frac{1}{\varepsilon_r}\nabla\times\boldsymbol{\psi}\right)=j\omega\varepsilon_0\{\boldsymbol{N}\}\cdot(\boldsymbol{i}_x\times\boldsymbol{\phi}_{\mathrm{in}})\\
&=j\omega\varepsilon_0\begin{bmatrix}\{N\}\cos\left(\frac{\pi z}{a}\right) & \{0\} & \{0\}\\ \{0\} & \{V\}\cos\left(\frac{\pi z}{a}\right) & \{0\}\\ \{0\} & \{0\} & \{N\}\sin\left(\frac{\pi z}{a}\right)\end{bmatrix}\begin{bmatrix}0&0&0\\0&0&-1\\0&1&0\end{bmatrix}\begin{bmatrix}\sin\left(\frac{\pi z}{a}\right)\{N\}^T\{\phi_x\}_{\mathrm{in}}\\ \sin\left(\frac{\pi z}{a}\right)\{V\}^T\{\phi_y\}_{\mathrm{in}}\\ \cos\left(\frac{\pi z}{a}\right)\{N\}^T\{\phi_z\}_{\mathrm{in}}\end{bmatrix}\\
&=j\omega\varepsilon_0\begin{bmatrix}[0] & [0] & [0]\\ [0] & [0] & -\{V\}\{N\}^T\cos^2\left(\frac{\pi z}{a}\right)\\ [0]\ \{N\}\{V\}^T\sin^2\left(\frac{\pi z}{a}\right) & & [0]\end{bmatrix}\begin{bmatrix}\{\phi_x\}_{\mathrm{in}}\\ \{\phi_y\}_{\mathrm{in}}\\ \{\phi_z\}_{\mathrm{in}}\end{bmatrix}
\end{aligned}
\tag{3.44}
$$

On the other hand, when expressed using the magnetic field, it can be written as follows:

$$
\begin{aligned}
&\{\boldsymbol{N}\}\cdot\left(\boldsymbol{i}_x\times\frac{1}{\varepsilon_r}\nabla\times\boldsymbol{\Psi}_{\mathrm{in}}\right)\\
&=\frac{1}{\varepsilon_r}\begin{bmatrix}\{N\}\cos\left(\frac{\pi z}{a}\right) & \{0\} & \{0\}\\ \{0\} & \{V\}\cos\left(\frac{\pi z}{a}\right) & \{0\}\\ \{0\} & \{0\} & \{N\}\sin\left(\frac{\pi z}{a}\right)\end{bmatrix}\begin{bmatrix}0&0&0\\0&0&-1\\0&1&0\end{bmatrix}\\
&\qquad\begin{bmatrix}0 & -\frac{\partial}{\partial z} & \frac{\partial}{\partial y}\\ \frac{\partial}{\partial z} & 0 & j\beta\\ -\frac{\partial}{\partial y} & -j\beta & 0\end{bmatrix}\begin{bmatrix}\{N\}^T\cos\left(\frac{\pi z}{a}\right) & \{0\} & \{0\}\\ \{0\} & \{V\}^T\cos\left(\frac{\pi z}{a}\right) & \{0\}\\ \{0\} & \{0\} & \{N\}^T\sin\left(\frac{\pi z}{a}\right)\end{bmatrix}\begin{bmatrix}\{\psi_x\}_{\mathrm{in}}\\ \{\psi_y\}_{\mathrm{in}}\\ \{\psi_z\}_{\mathrm{in}}\end{bmatrix}\\
&=\frac{1}{\varepsilon_r}\begin{bmatrix}\{0\} & \{0\} & \{0\}\\ \{0\} & \{0\} & -\{V\}\cos\left(\frac{\pi z}{a}\right)\\ \{0\} & \{N\}\sin\left(\frac{\pi z}{a}\right) & \{0\}\end{bmatrix}\\
&\qquad\begin{bmatrix}\{0\}^T & \frac{\pi}{a}\sin\left(\frac{\pi z}{a}\right)\{V\}^T & \sin\left(\frac{\pi z}{a}\right)\frac{\partial\{N\}^T}{\partial y}\\ -\frac{\pi}{a}\sin\left(\frac{\pi z}{a}\right)\{N\}^T & \{0\}^T & j\beta\sin\left(\frac{\pi z}{a}\right)\{N\}^T\\ -\cos\left(\frac{\pi z}{a}\right)\frac{\partial\{N\}^T}{\partial y} & -j\beta\cos\left(\frac{\pi z}{a}\right)\{V\}^T & \{0\}^T\end{bmatrix}\begin{bmatrix}\{\psi_x\}_{\mathrm{in}}\\ \{\psi_y\}_{\mathrm{in}}\\ \{\psi_z\}_{\mathrm{in}}\end{bmatrix}\\
&=\frac{1}{\varepsilon_r}\begin{bmatrix}[0] & [0] & [0]\\ \{V\}\frac{\partial\{N\}^T}{\partial y}\cos^2\left(\frac{\pi z}{a}\right) & j\beta\{V\}\{V\}^T\cos^2\left(\frac{\pi z}{a}\right) & [0]\\ -\frac{\pi}{a}\{N\}\{N\}^T\sin^2\left(\frac{\pi z}{a}\right) & [0] & j\beta\sin^2\left(\frac{\pi z}{a}\right)\{N\}\{N\}^T\end{bmatrix}\\
&\qquad\begin{bmatrix}\{\psi_x\}_{\mathrm{in}}\\ \{\psi_y\}_{\mathrm{in}}\\ \{\psi_z\}_{\mathrm{in}}\end{bmatrix}
\end{aligned}
\tag{3.45}
$$

The vector {u} associated with the boundary condition on the plane of incidence can be seen from the above as

$$\begin{aligned}\{u\} &= \int\!\!\int_{\Gamma} \left\{ \{\boldsymbol{N}\}^* \cdot \left(\boldsymbol{i}_n \times \frac{1}{\varepsilon_r} \nabla \times \boldsymbol{\Psi} \right) \right\} dS \\ &= \sum_{\Gamma} \begin{bmatrix} [B_{tx}] & [B_{ty}] & [0] \\ [B_{zx}] & [0] & [B_{zz}] \end{bmatrix} \begin{bmatrix} \{\psi_x\}_\Gamma \\ \{\psi_y\}_\Gamma \\ \{\psi_z\}_\Gamma \end{bmatrix} \end{aligned} \tag{3.46}$$

Here,

$$\boldsymbol{\psi}_\Gamma = \boldsymbol{i}_x \{N\}\{\psi_x\}_\Gamma + \boldsymbol{i}_y \{V\}\{\psi_y\}_\Gamma + \boldsymbol{i}_z \{N\}\{\psi_z\}_\Gamma \tag{3.47}$$

$$[B_{tx}] = \sum_{\Gamma} \int_{\Gamma} \frac{1}{\varepsilon_r} \{V\} \frac{\partial \{N\}^T}{\partial y} dy \tag{3.48}$$

$$[B_{ty}] = \sum_{\Gamma} \int_{\Gamma} j\beta \frac{1}{\varepsilon_r} \{V\}\{V\}^T dy \tag{3.49}$$

$$[B_{zx}] = \sum_{\Gamma} \int_{\Gamma} -\frac{1}{\varepsilon_r} \left(\frac{\pi}{a} \right) \{N\}\{N\}^T dy \tag{3.50}$$

$$[B_{zz}] = \sum_{\Gamma} \int_{\Gamma} j\beta \frac{1}{\varepsilon_r} \{N\}\{N\}^T dy \tag{3.51}$$

3.4 Basic Equation of LSE Mode and Solution

The NRD guide has the LSE mode in addition to the LSM mode, and these two modes have the same symmetry in the z-direction. Coupling occurs as a result of bends and discontinuities. As a result, the LSE mode power at the input/output port must also be evaluated. It is required for the LSE mode. It is easier to use E_z, and its basic formula and boundary conditions are written as follows:

$$\frac{\partial^2 \phi_z}{\partial y^2} + \left\{ \varepsilon_r k_0^2 - \left(\beta^2 + \frac{\pi}{a} \right)^2 \right\} \phi_z = 0 \tag{3.52}$$

$$\begin{aligned} \kappa b - 2\tan^{-1}\left(\frac{\alpha}{\kappa}\right) - m\pi = 0 \\ \left(\kappa = \sqrt{\varepsilon_{r,1} k_0^2 - \beta^2}, \;\; \alpha = \sqrt{\beta^2 - \varepsilon_{r,2} k_0^2} \right) \end{aligned} \tag{3.53}$$

The eigenmode amplitude ψ_z can be written as follows when the eigenvalue is obtained by solving (3.53) under boundary conditions:

$$\phi_z = \begin{cases} E_0 \cos(\kappa(y - y_0)) & (|y - y_0| \leq b/2) \\ E_0 \cos(\kappa b/2) \exp(-\alpha|y - y_0|) & (|y - y_0| > b/2) \end{cases} \tag{3.54}$$

Furthermore, once ψ_z is known, the other electromagnetic field components can be written as follows:

$$\phi_x = -\frac{1}{j\beta}\left(\frac{\pi}{a}\right)\phi_z \tag{3.55}$$

$$\phi_y = 0 \tag{3.56}$$

$$\psi_x = -\frac{1}{j\omega\mu_0}\frac{\partial\phi_z}{\partial y} \tag{3.57}$$

$$\psi_y = -\frac{1}{\omega\mu_0\beta}\left\{\left(\frac{\pi}{a}\right)^2 + \beta^2\right\}\phi_z \tag{3.58}$$

$$\psi_z = \frac{1}{j\omega\mu_0}\frac{\partial\phi_x}{\partial y} = \frac{1}{\omega\mu_0\beta}\left(\frac{\pi}{a}\right)\frac{\partial\phi_z}{\partial y} \tag{3.59}$$

The power carried by the LSE and LSM modes along the waveguide is as follows:

$$\begin{aligned} P_{\mathrm{LSE}} &= \mathrm{Re}\left\{\int \frac{a}{4}\boldsymbol{E}\times\boldsymbol{H}^*\cdot\boldsymbol{i}_x dy\right\} = \mathrm{Re}\left\{\frac{a}{4}\int -\phi_z\psi_y^* dy\right\} \\ &= \frac{a}{4}\cdot\frac{1}{\omega\mu_0\beta}\left\{\left(\frac{\pi}{a}\right)^2 + \beta^2\right\}\int |\phi_z|^2 dy \\ &= \frac{a}{4}\cdot\left[\frac{1}{\omega\mu_0\beta}\left\{\left(\frac{\pi}{a}\right)^2 + \beta^2\right\}\right]^{-1}\int |\psi_y|^2 dy \end{aligned} \tag{3.60}$$

$$\begin{aligned} P_{\mathrm{LSM}} &= \mathrm{Re}\left\{\int \frac{a}{4}\boldsymbol{E}\times\boldsymbol{H}^*\cdot\boldsymbol{i}_x dy\right\} = \mathrm{Re}\left\{\frac{a}{4}\int \phi_y\psi_z^* dy\right\} \\ &= \frac{a}{4}\cdot\frac{1}{\omega\varepsilon_0\beta}\left\{\left(\frac{\pi}{a}\right)^2 + \beta^2\right\}\int \frac{1}{\varepsilon_r}|\psi_z|^2 dy \end{aligned} \tag{3.61}$$

The normalization condition is satisfied by the eigenmode amplitude.

$$\int |\phi_z|^2 dy = 1 \ \text{ for LSE mode} \tag{3.62}$$

$$\int \frac{1}{\varepsilon_r}|\psi_z|^2 dy = 1 \ \text{ for LSM mode} \tag{3.63}$$

After obtaining model amplitudes for LSM and LSE modes, the normalized modal power for LSM_{n1} and LSE_{n1} respectively are calculated as follows:

$$P_{\mathrm{LSM_{n1}}} = \frac{\beta_{\mathrm{LSM_{01}}}\left\{(\pi/a)^2 + \beta^2_{\mathrm{LSM_{n1}}}\right\}}{\beta_{\mathrm{LSM_{n1}}}\left\{(\pi/a)^2 + \beta^2_{\mathrm{LSM_{01}}}\right\}}|a_{\mathrm{LSM_{n1}}}|^2 \tag{3.64}$$

$$P_{\mathrm{LSE_{n1}}} = \frac{\varepsilon_0 \beta_{\mathrm{LSM_{01}}} \left\{(\pi/a)^2 + \beta^2_{\mathrm{LSE_{n1}}}\right\}}{\mu_0 \beta_{\mathrm{LSE_{n1}}} \left\{(\pi/a)^2 + \beta^2_{\mathrm{LSM_{01}}}\right\}}$$
$$= \frac{\beta_{\mathrm{LSM_{01}}} \left\{(\pi/a)^2 + \beta^2_{\mathrm{LSE_{n1}}}\right\}}{\beta_{\mathrm{LSE_{n1}}} \left\{(\pi/a)^2 + \beta^2_{\mathrm{LSM_{01}}}\right\}} \left|\frac{a_{\mathrm{LSE_{n1}}}}{\eta_0}\right|^2$$
$$\left(\eta_0 = \sqrt{\frac{\mu_0}{\varepsilon_0}}\right) \tag{3.65}$$

In the full-vector analysis using the magnetic field, ψ_z is obtained as

$$\phi_z = -j\frac{1}{\omega\varepsilon_0\varepsilon_r}\left(\frac{\partial\{V\}^T}{\partial x} - \frac{\partial\{U\}^T}{\partial y}\right)\{\psi_t\} \tag{3.66}$$

3.5 Analysis of 2D-FV-FEM

To validate the developed two-dimensional full vectorial finite element method, we first calculate the guided modes in the NRD guide with dielectric strip height $a = 2.25\,\mathrm{mm}$ and width $b = 2.25\,\mathrm{mm}$. The relative permittivity of dielectric material and air is $\varepsilon_r = 2.2$ and $\varepsilon_{\mathrm{air}} = 1.0$ respectively. The $\mathrm{LSM_{01}}$ mode is considered incident at 60 GHz. Figure 3.2 shows the guided modes in the NRD guide calculated by 2D-FV-FEM analytically. For more confirmation, we compared 2D analysis with 3D analysis, and we can see that both are in good agreement. The field distribution of the $\mathrm{LSM_{01}}$ mode is shown in Fig. 3.3. After the guided mode analysis, we considered bending waveguide for the propagation analysis whose structure is shown in Fig. 3.4. The height and width of dielectric strip is $a = b = 2.25\,\mathrm{mm}$. The bending waveguide inner and outer radii are $R_1 = 3.875\,\mathrm{mm}$ and $R_1 = 6.125\,\mathrm{mm}$, respectively. The $\mathrm{LSM_{01}}$ mode is used to excite input port 1 at a frequency of 60 GHz. Figure 6.5 depicts the propagating fields of bending waveguides using 2D-FV-FEM and 3D-FV-FEM and both demonstrate excellent agreement. The 2D-FV-FEM analysis requires only 0.4 GB of memory and 4.5 s of computational time on a PC with an Intel(R) Xeon(R) CPU E5-2660 v4 at 2.00 GHz, whereas the 3D-FV-FEM analysis requires about 20 GB of memory and 109 s of computational time.

We can see how efficient our originally developed 2D simulation method is based on the computed computational resources above. Our 2D-FV-FEM is extremely useful for optimal design approaches that require analyzing waveguide devices multiple times with minimal computational time. In the following chapter, we

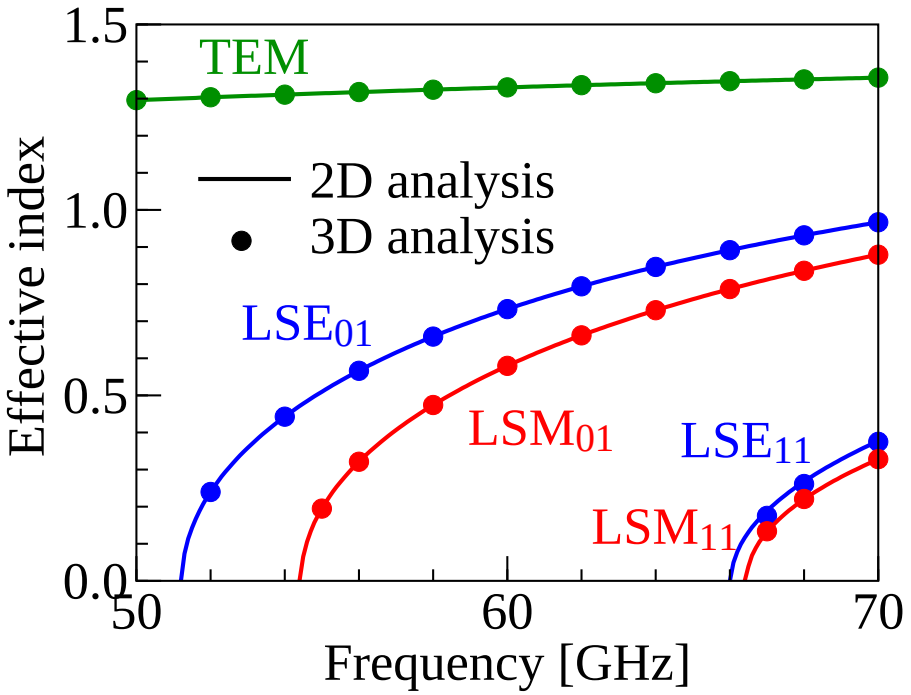

Figure 3.2: Dispersion relation of guided modes in an NRD guide at $a = 2.25$ mm, $b = 2.25$ mm, and $\varepsilon_r = 2.2$.

Figure 3.3: Field distribution of LSM_{01} mode at 60 GHz.

combine our 2D-FV-FEM with a variety of optimal design approaches.

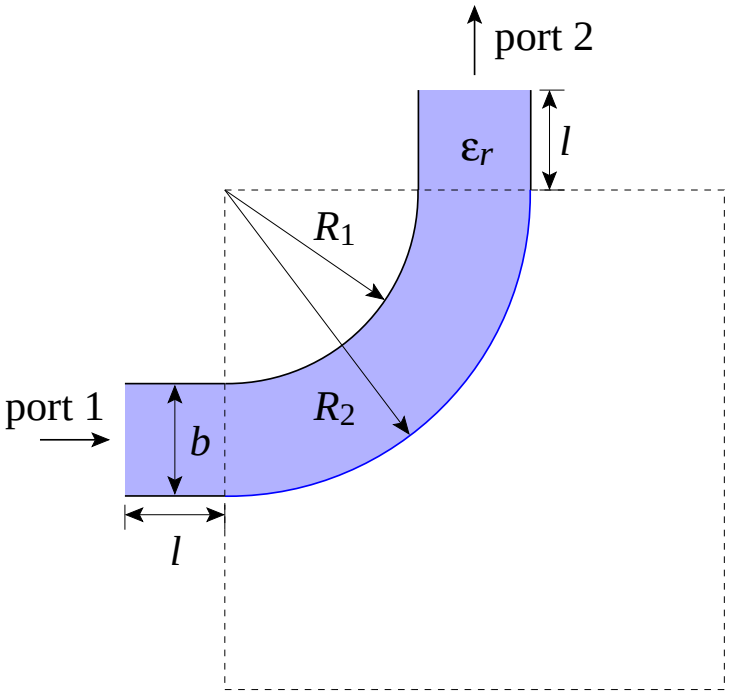

Figure 3.4: Design setup of NRD bending waveguide.

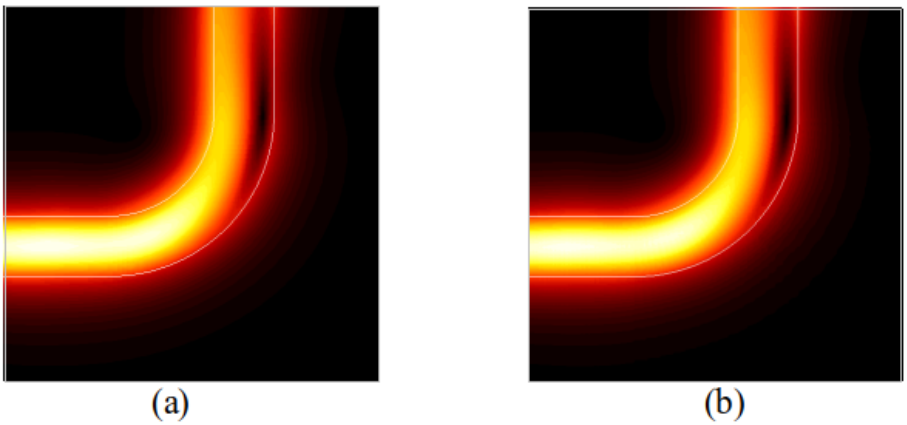

Figure 3.5: Propagation fields obtained by using (a) 2D-FV-FEM (b) 3D-FV-FEM.

Chapter 4

Optimal Design Approaches for NRD Guide Devices

In the preceding chapter, we developed a two-dimensional full vectorial finite method (2D-FV-FEM) to efficiently simulate the NRD guide devices. In this chapter, we present optimal design approaches based on the mosaic optimization concept for the designing of NRD guide devices with the goal of realizing high-performance, small-footprint millimeter-wave integrated circuits as shown in Fig. 4.1. Various optimization methods have been proposed and their effectiveness has been shown. There are inherent difficulties in designing NRD guides, and it is especially important to study wideband operation. Several optimal design approaches have been proposed for optical guide devices such as geometric optimization, topology optimization, genetic algorithm, particle swarm optimization, direct binary search algorithm, inverse design algorithm, and differential evolution algorithm [49]-[75]. But research for the development of these optimal design approaches with different optimization strategies for NRD guide devices have not been conducted. All these above optimization approaches have good enough search ability to design NRD guides with unique structure ideas.

In this chapter, as an optimization method, we employ either direct binary search (DBS) algorithm or genetic algorithm (GA) depending on design problems. In order to improve design efficiency, we employ the originally developed two-dimensional full vectorial finite element method (2D-FVFEM) which can accurately model 3D structure of NRD as a numerical simulation method. To show the usefulness of developed optimization method we considered several NRD guide devices which includes crossing waveguide, 90°-bend waveguide, T-branch, and Z-bend waveg-

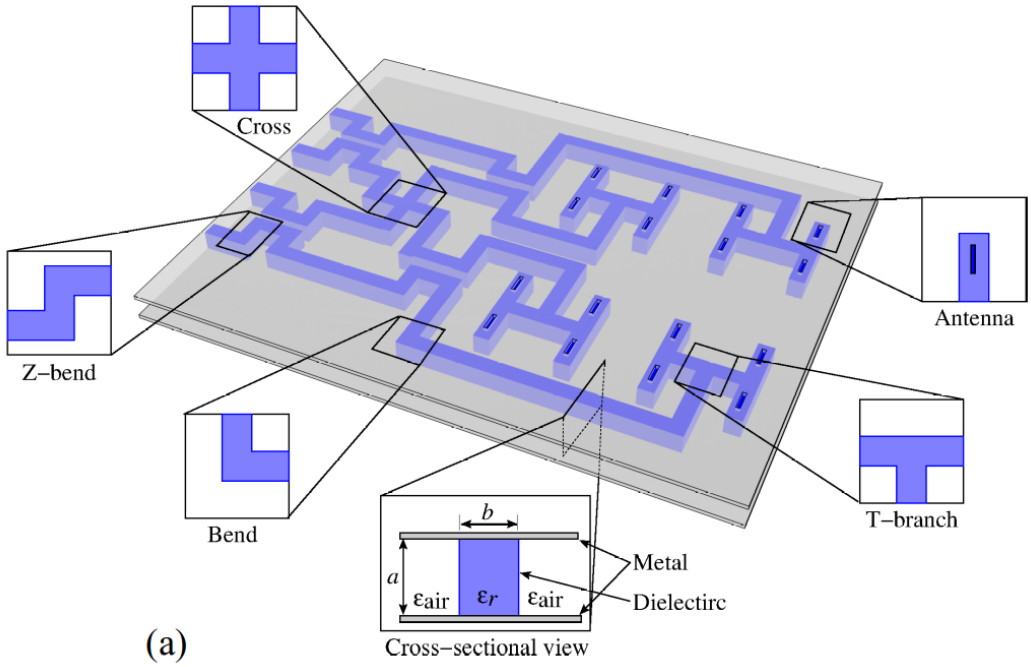

Figure 4.1: Image of NRD based millimeter-wave circuit.

uide. This chapter demonstrates the structure representation of NRD guide based on mosaic optimization concepts, detailed implementation procedure of developed optimization approaches and the numerical simulation results of considered NRD guide devices at 60 GHz.

4.1 Structure Representation of NRD Guide Using Mosaic Optimization

Achieving the desired properties typically requires many design variables to optimize material distribution in the target area of the guide device. Several optimization approaches have been proposed to optimize these variables, using various optimization concepts such as shape, size, and topology optimization. In which, size optimization deals with dimensional parameters such as the length and width of the structure, whereas shape optimization optimizes the outer shape of the structure, and the topology optimization optimizes the material distribution within area of interest. On other hand, mosaic-based optimization is another way to efficiently optimize the guide devices. Mosaic structures show the presence of dielectric materials in the form of pixels at particular positions within the area of interest.

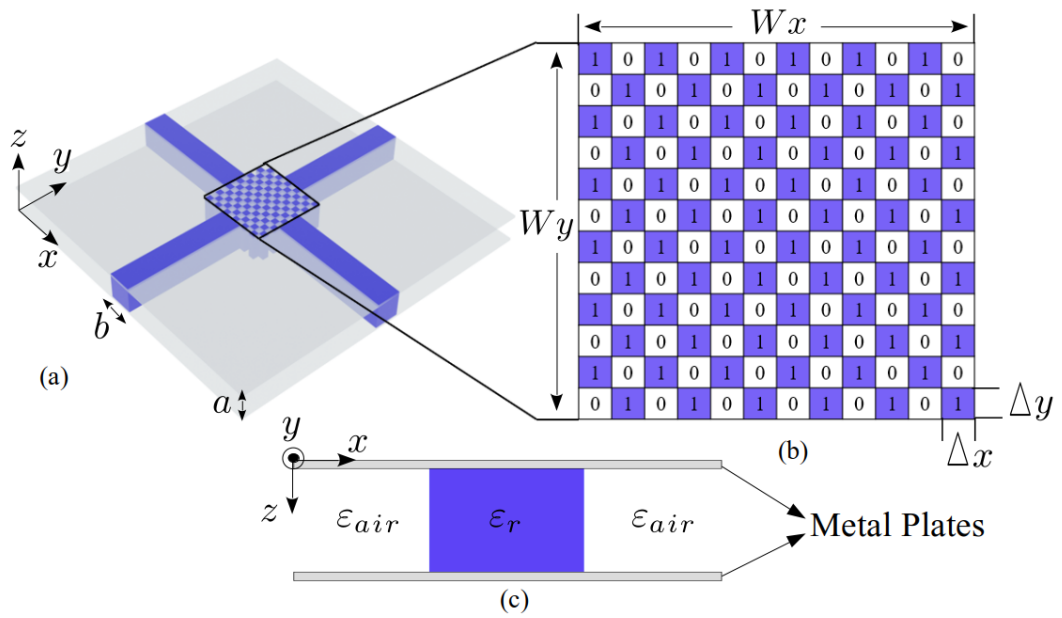

Figure 4.2: Non radiative dielectric (NRD) waveguide (a) design setup (b) representation of design region using mosaic-based optimization concept (c) front view of NRD guide.

In this work, mosaic-based optimization using direct binary search algorithm and evolutionary approaches are considered to optimize the material distribution in the design region of NRD guide. Several design variables are employed to express material distribution in the design region. In order to create a mosaic-like structure, first discretize the design region into a grid pattern and then allocate a dielectric or air to each pixel (also known as a mosaic) in the form of 1 or 0, respectively as shown in Fig. 4.2. This is called the concept of digital materials. The degree of design freedom of our optimization approaches is determined by the number of pixels. A large number of mosaics may require large number of iterations or population size in evolutionary that may degrade the design efficiency of optimization method.

For the realization of highly attributed circuit components, we used suitable mosaic size that is completely compatible with the design efficiency of optimization method. A large number of pixels may make it difficult to fabricate a designed device too. The pixel size is determined not by the convenience of the optimization method, but by the possibility of fabrication. A brief description of implementing the optimization approach is given below in the next section.

4.2 Implementation of Optimization Algorithm

The aim of our optimal design is to obtain optimal structure with desired outputs when fundamental LSM_{01} is launched into port 1. For this purpose, a structure in design region is expressed by numerical design variables and those values are optimized by DBS and genetic algorithm. The DBS algorithm is a simple approach, easily to be implemented, and sometimes efficiently provide an optimal structure. However, DBS is not guaranteed to give a globally optimal solution. In order to offer more versatile design, we also employ GA.

4.2.1 Direct Binary Search Algorithm

Initially we developed a direct binary search algorithm for the distribution of dielectric pixels in the design region of NRD guide devices. The purpose of this approach is to achieve maximum transmission efficiency by the optimization of the design region when LSM_{01} mode is applied at input port 1. To achieve the desired output, the developed approach optimizes the different design variables that represents the material distribution of the considered model. The designed approach discretizes the design region into a grid pattern and assign the air or dielectric material to each pixel. In DBS algorithm, a random selection of pixel is evaluated first so as to invert its state, then performance of device (transmission efficiency) is calculated. The pixel state is retained if the device performance is improved than initially generated structure otherwise pixel state is restored. The proposed approach iterates this operation on all pixels randomly until the desired result is achieved or the result is not improved more. The detailed working procedure of DBS algorithm is shown in Fig. 4.3.

4.2.2 Genetic Algorithm

GA is more versatile design approach than DBS and is applied to various optimization problems. Although various version of GA is developed, we employ a standard GA algorithm. First, some individuals with random grid pattern are generated and these individuals evolve based on genetic operation, such as selection, crossover, and mutation. In this study, we employ both elite selection and ranking selection as a selection scheme. In each generation, only one best individual is saved by elite

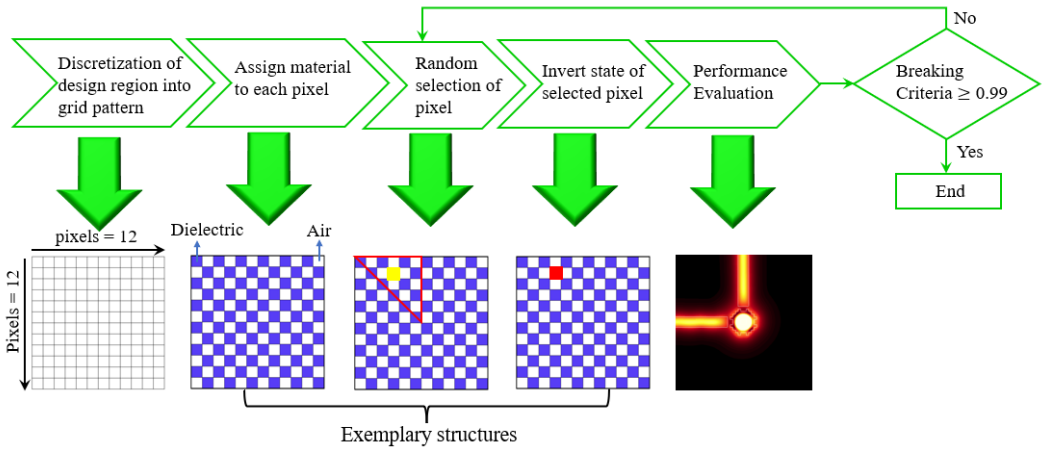

Figure 4.3: Detailed working procedure of DBS algorithm

selection and the other individuals are generated by uniform crossover of two parent individuals selected by ranking selection. After that, all the individuals except for elite individual may mutate with a predetermined probability. This change of generations is repeated until the desired property is obtained or the property is no longer improved. In evolutionary methods such as GA, the search space becomes wider as the design variables increase. A larger number of individuals and number of iterations will be required, but in the design using this digital material, due to the non-radioactivity of the NRD guide, it is possible to design a very compact element. It is possible to efficiently optimize by GA with relatively few design variables. The detailed working procedure of genetic algorithm is shown in Fig. 4.4.

4.3 Numerical Examples

In order to show the usefulness of our approach, design examples of crossing and T-branch waveguides are considered. To show the design efficiency more clearly, we compare the simulation results of non-optimal NRD guide structures with optimal ones obtained by using DBS approach. In the following design examples, we assume the metal plate separation is $a = 2.25\,\mathrm{mm}$, the dielectric strip width is $b = 2.2\,\mathrm{mm}$, and the relative permittivities of the dielectric and air are $\varepsilon_r = 2.2$ and $\varepsilon_{\mathrm{air}} = 1.0$ respectively. The dispersion relation of NRD guide using above parameters is shown in Fig. 4.5. Furthermore, LSM_{01} mode operation around 60

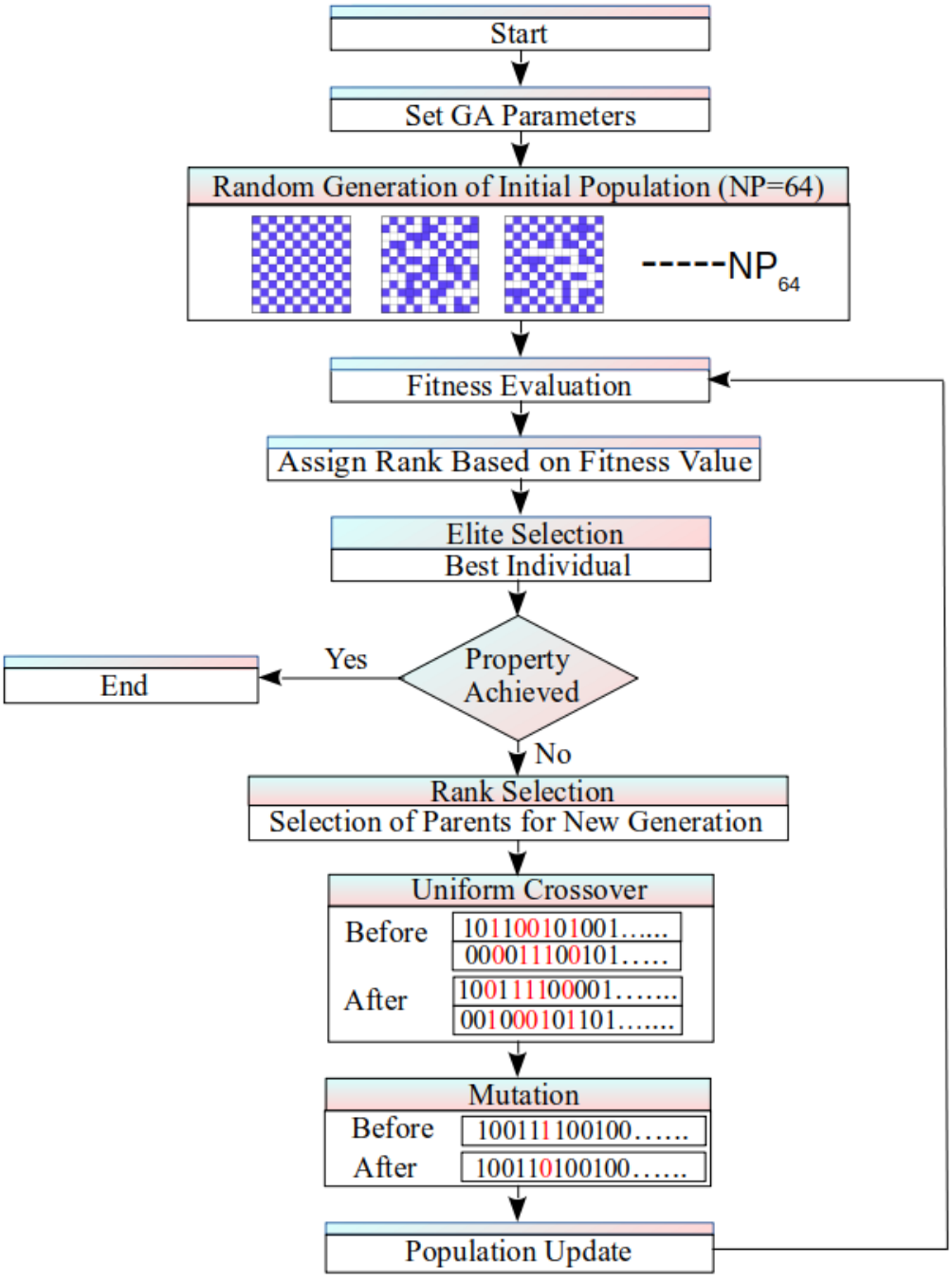

Figure 4.4: Detailed working procedure of GA algorithm

GHz is considered and incident port is set to be port 1.

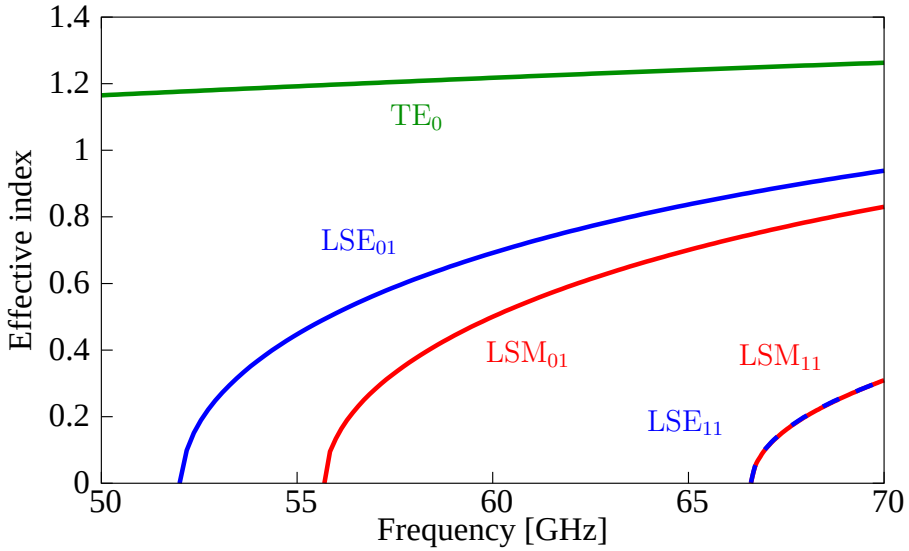

Figure 4.5: Dispersion relation of NRD guide using $a = 2.25$ mm, $b = 2$ mm, and $\varepsilon_r = 2.2$.

4.3.1 Crossing Waveguide

In order to show the potential of our optimization approach, first, a low crosstalk crossing waveguide is designed by using DBS algorithm. The design setup and optimized structure of NRD crossing waveguide is shown in Fig. 4.6. The structural parameters are set to be $d_{\mathrm{PML}} = 5$ mm, $l = 10$ mm and $W_x = W_y = 6$ mm. The design region is discretized into 12×12 pixels with size of $0.5\ \mathrm{mm} \times 0.5\ \mathrm{mm}$. In order to make the fabrication feasible, the pixel size is determined by considering the operating wavelength, guide width, and fabrication sensitivity. Utilizing structural symmetry, only the pixels in one-eighth region surrounded red line (21 pixels) are designed. The material in each pixel has been optimized by DBS approach in just 10 iterations.

In this numerical example, we targeted the maximum power transmission from input port to output port, when LSM_{01} mode at frequency of 60 GHz is launched into input port 1. The steady state propagation field in the non-optimized structure and the optimized structure are shown in Fig. 4.7. The transmission efficiency is 99.9 % in the optimized crossing waveguide compared with that of 61.0 % in the non-optimized one. We can see that clearly in Fig. 4.7 the optimized structure greatly suppresses the reflection and crosstalk effect than the non-optimized one. Furthermore, the frequency characteristics of the non-optimized and optimized

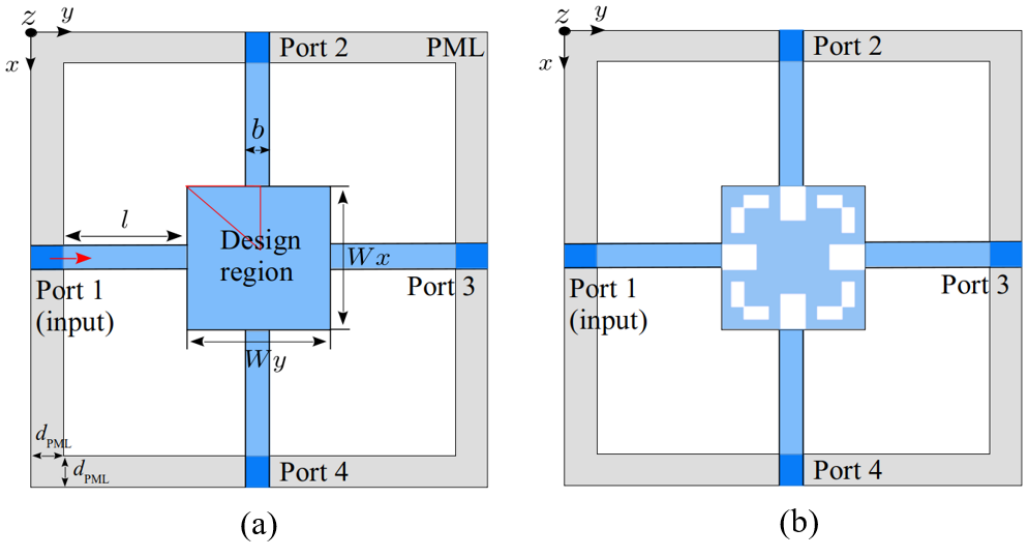

Figure 4.6: (a) Design model of crossing waveguide and (b) its optimized structure.

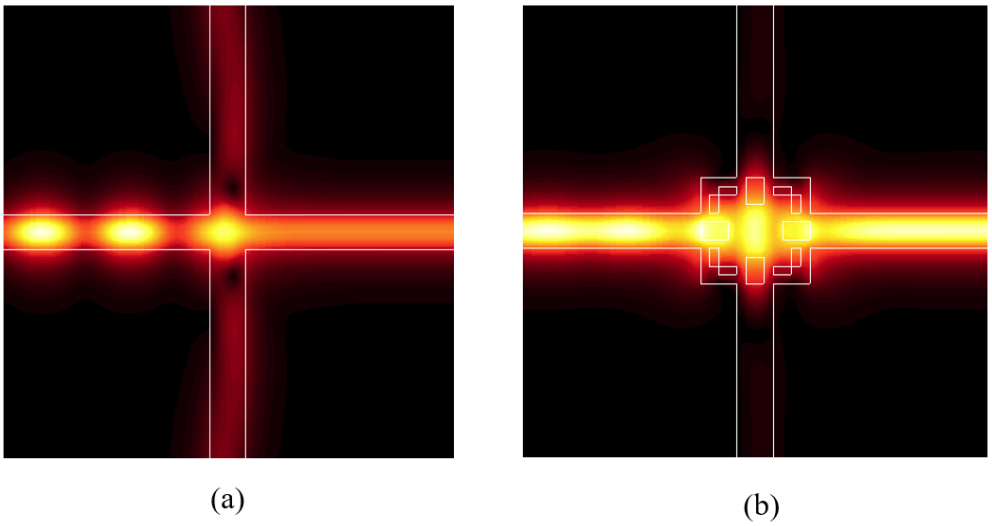

Figure 4.7: Propagation field in NRD crossing waveguide (a) non-optimized structure (b) optimized structure.

crossing waveguides are shown in Fig. 4.8. Numerical results of those devices calculated by 3D-FV-FEM are also shown. The designed approach realized the device structure with the remarkable transmission characteristics and practical design specifications. Figure 4.6 shows that the NRD guide can be intersected on a planar circuit. It has the potential to further miniaturize the NRD guide circuit.

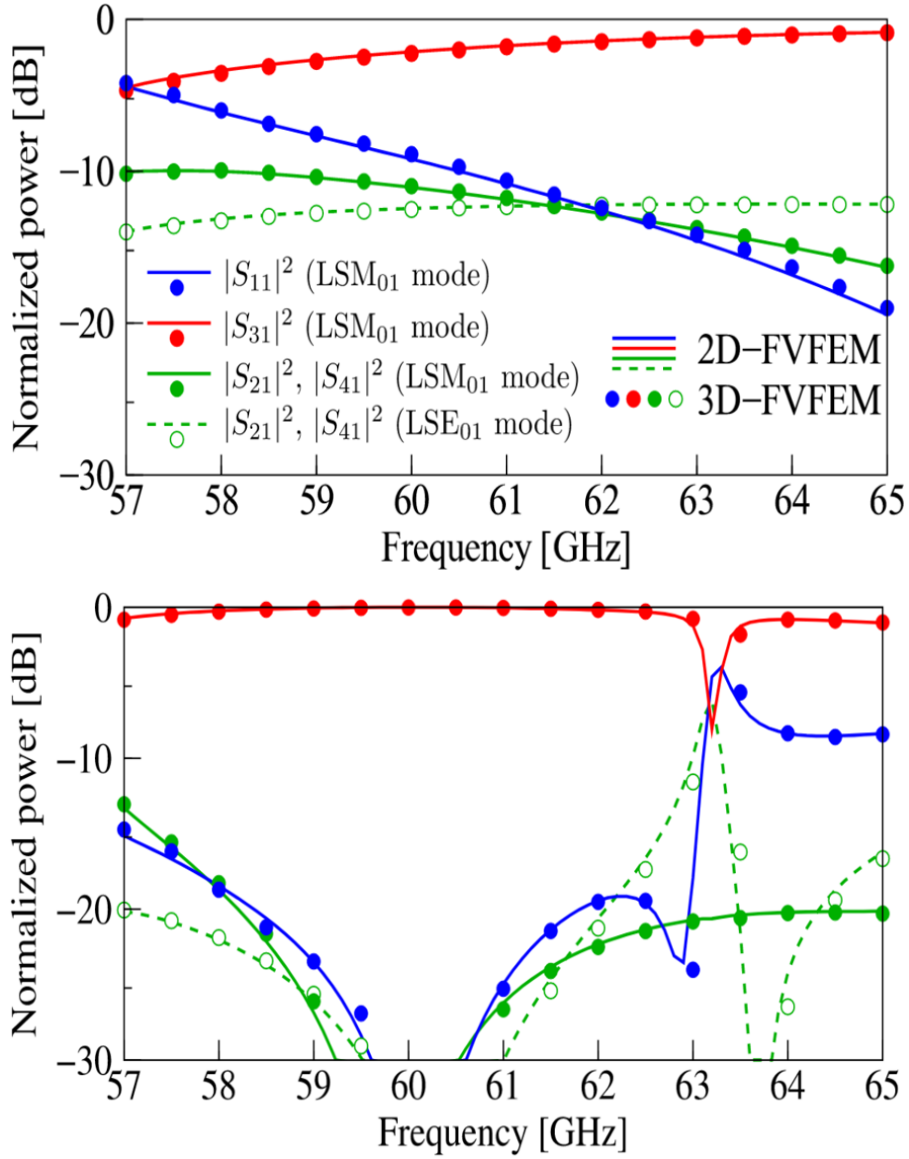

Figure 4.8: The normalized powers of NRD crossing waveguide (upper) non-optimized and (lower) optimized.

4.3.2 90°-bend Waveguide

Next, we designed a 90°-bend waveguide. The structural parameters and incidence condition are the same as considered in the previous example. Fig. 4.9 shows the design setup of the 90°-bend waveguide and the optimized structure. The pixel pattern is optimized by DBS algorithm and we achieved desired output in just 17 iterations. The steady-state propagation field in the non-optimized and

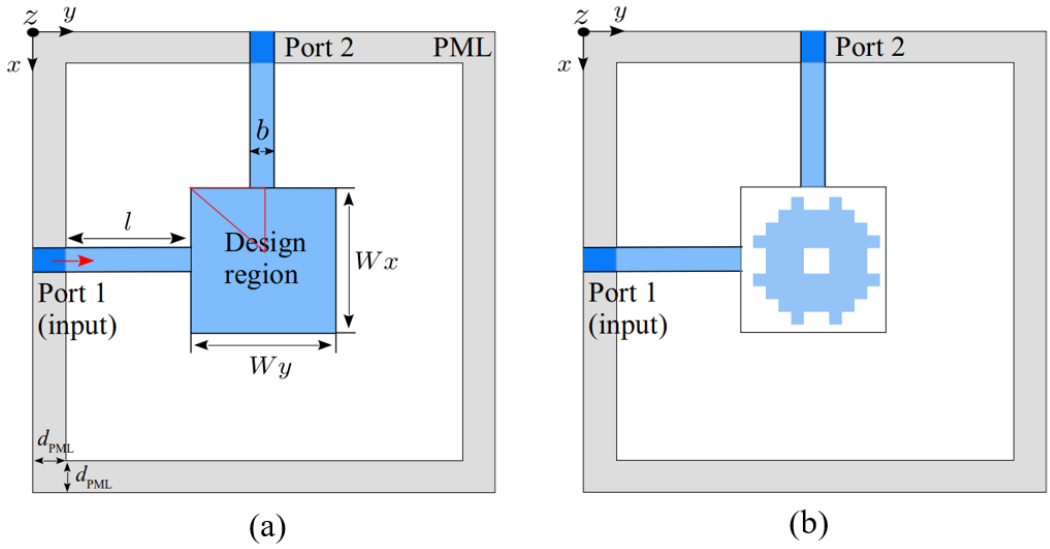

Figure 4.9: (a) Design model of NRD 90^0-bend waveguide and (b) its optimized structure.

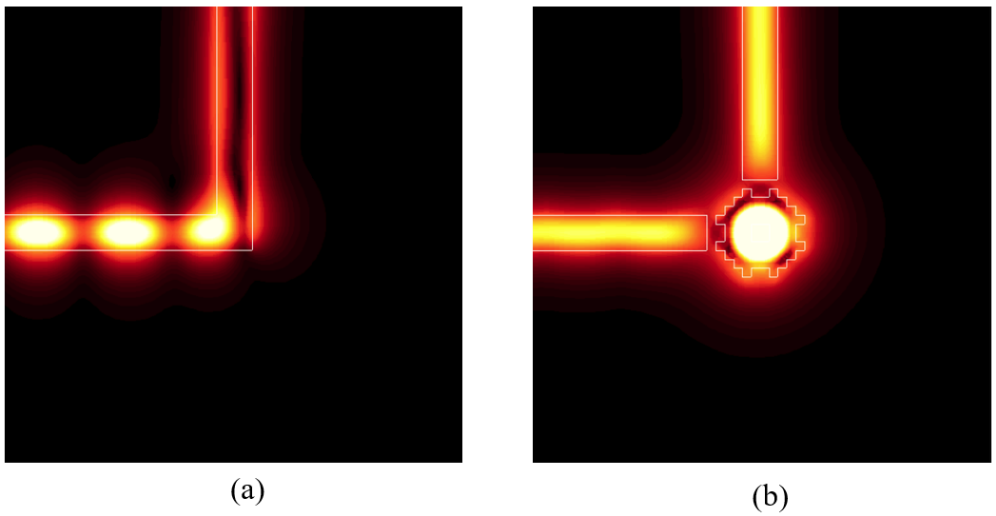

Figure 4.10: Propagation field in NRD 90^0-bend waveguide (a) non-optimized structure (b) optimized structure.

optimized structure are shown in Fig. 4.10. We achieved 99.0% transmission efficiency in the optimized structure as compared to 2.2% in the non-optimized one. Furthermore, the frequency characteristics of the non-optimized and optimized structure calculated by 2D-FVFEM and 3D-FVFEM are also shown in Fig. 4.11. The designed devices are simulated by originally developed 2D simulation method and we can see that design efficiency is greatly improved by using 2D-FV-FEM. The

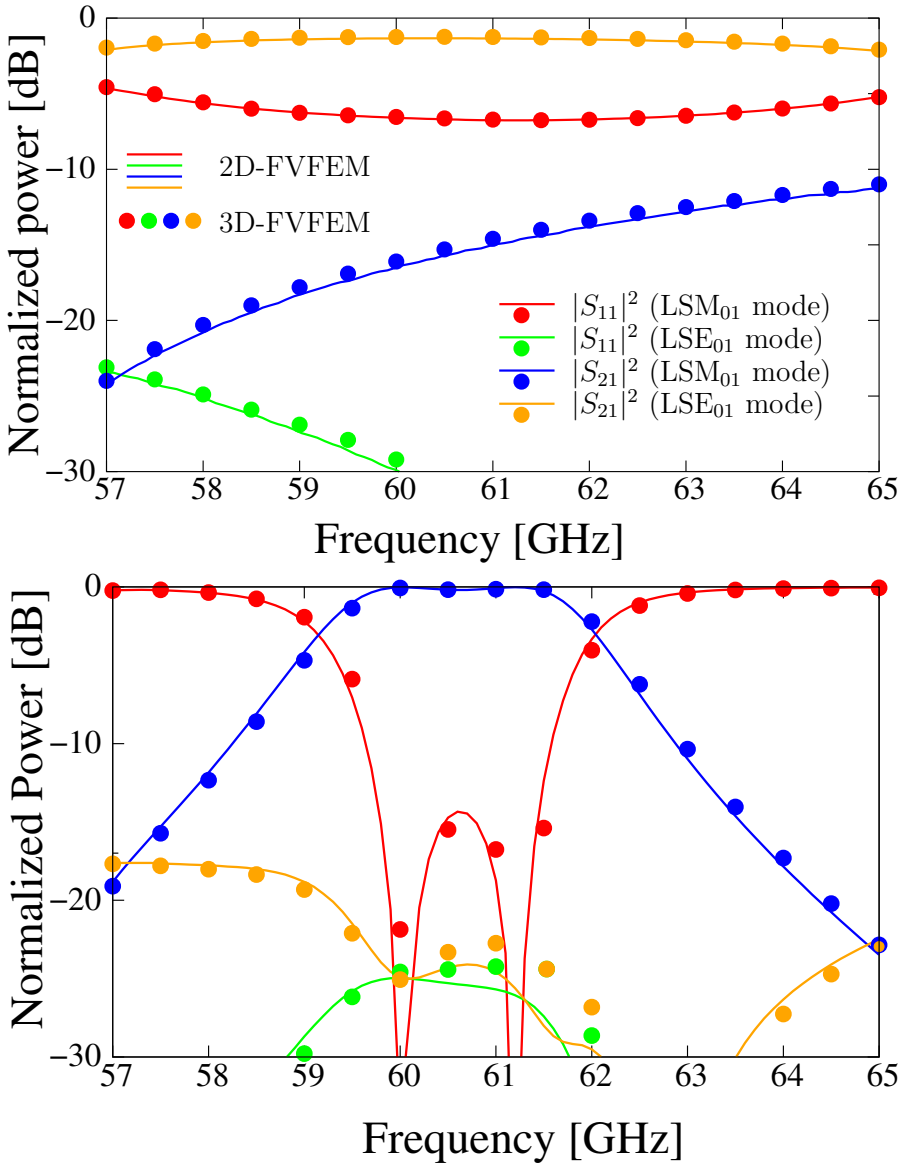

Figure 4.11: The normalized powers of 90°-bend waveguide (upper) non-optimized and (lower) optimized.

2D-FV-FEM analysis used only 2.7 s with 0.26 GB of memory for computation at PC Intel(R) Core(TM) i9-9900k CPU at 3.60 GHz, whereas 3D-FV-FEM required 798 s with 0.92 GB of memory using a PC Intel(R) Xeon (R) Gold 6242 CPU at 2.80 GHz. The proposed optimization approach proves its significance in aspect of remarkable performance and practical design specifications. The advantage of DBS is it is ease to implement and can optimize the structure in few iterations as proved above in considered devices. In case of NRD guide using mosaic optimization

concept DBS algorithm have some limitation too it is not so efficient for complex device structure such as T-branch and Z-bend waveguide or for broadband operation. For this purpose, we employ GA for these devices to achieve desired properties. Furthermore, in the above study, we considered single operating frequency in the optimal design. The obtained devices may have narrow bandwidth or may show abrupt performance deterioration at specific frequency due to resonance behavior. In order to widen the bandwidth, it may be possible to widen the bandwidth by discretizing the operating band at equal intervals and considering it in the objective function. Due to the resonant behavior, large deterioration of characteristics was sometimes seen at frequencies not considered. In order to avoid this, we have devised the setting of the objective function. We developed a method to randomly change the frequency to be considered in each generation of genetic algorithm (GA). The usefulness of this method has been confirmed through some design examples. The optimal results of T-branch and Z-bend waveguide at 60 GHz and at broadband operation are discussed below.

4.3.3 T-branch Waveguide

Now, we design a NRD T-branch guide, which split the input power equally into output ports. The initial design setup of T-branch guide is shown in Fig. 4.12. The configurational parameters are same as considered in crossing guide except symmetric conditions. In this example, we considered one-two symmetric condition in rectangle form for equal and smooth distribution of power towards output ports as shown in Fig. 4.12(a). Due to considered symmetry, 72 pixels (N_x = 12 N_y = 6) in the upper half of the design region are optimized using GA. To achieve the maximum transmission at 60 GHz, we considered the following objective function.

$$\text{Minimize } C = 1 - |S_{21}|^2 - |S_{41}|^2 \qquad (\text{at } 60 \text{ GHz}) \tag{4.1}$$

whereas, $|S_{21}|^2$ and $|S_{41}|^2$ are output powers at port 2 and port 4 respectively. In addition, we used a following objective function for broadband operation of NRD T-branch waveguide.

$$\text{Minimize } C = \sum_{i=1}^{5} (1 - |S_{21}(f_i)|^2 - |S_{41}(f_i)|^2) \tag{4.2}$$

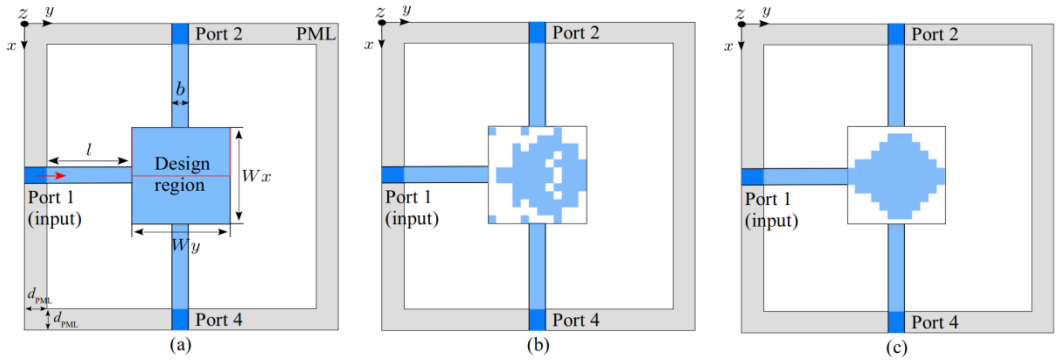

Figure 4.12: NRD T-branch waveguide (a) Initial design model, (b) optimized structure at 60 GHz, and (c) optimized structure for broadband operation.

$$(f_{1,2,3,4,5} = 58, 59, 60, 61, 62 \text{ GHz})$$

The optimized structures of T-branch guides are shown in Fig. 4.12(b,c). To optimize the structure, which split the maximum power equally with smooth propagation behavior, is a bit difficult in case of NRD T-branch guide, but in our study, we can see that how incident power smoothly split into two output ports in both cases as shown in Fig. 4.13. The normalized splitting power ratio of NRD T-branch guide at 60 GHz is $|S_{21}|^2 = 0.495$ $|S_{41}|^2 = 0.495$ as shown in Fig. 4.14. Figure 4.14(b) shows that the proposed T-branch guide achieved broad bandwidth in the frequency range of 58-62 GHz. However, it shows a negligible reflection $|S_{11}|^2$ at 58 or 62 GHz because of structural limitations. The value of objective function versus number of generations are shown in Fig. 4.15. It clearly shows that the solution of T-branch guide at frequency 60 GHz is quickly converged within 50 generations but broadband operation is quite different due to multiple frequencies involve during simulations. We achieved good enough convergence with desired broadband property in 300 generations. However, more than this takes a long computational time and the solution will not more converge as shown in Fig. 4.15.

4.3.4 Z-Bend Waveguide

Finally, NRD Z-bend guide is designed whose initial model is shown in Fig. 4.16. The structural parameters of this model are exactly same as in previous example except size of the design region as follows: $W_x = 10$ mm and $W_y = 16$ mm. We

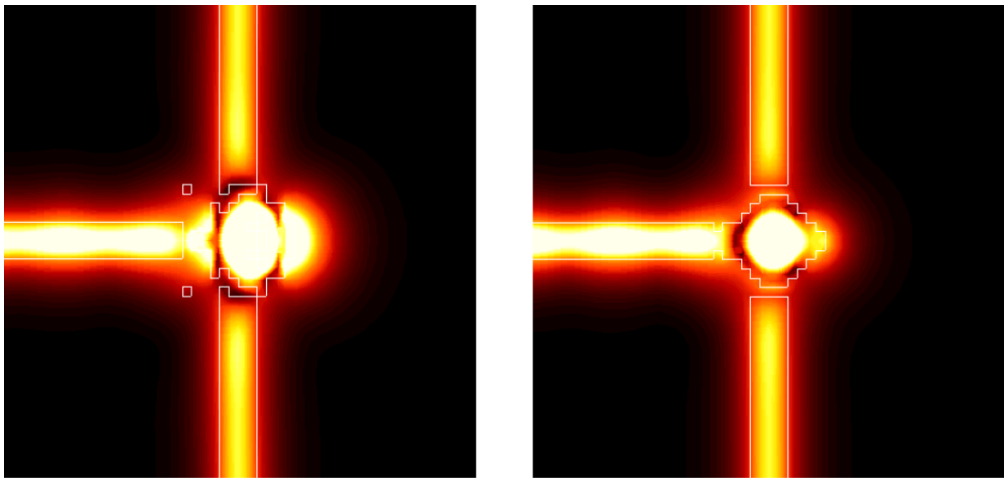

(a) (b)

Figure 4.13: Propagation fields of NRD T-branch waveguides. (a) At operating frequency 60 GHz and (b) broadband T-branch guide at 60 GHz.

assume half of the design region for the optimization of pixels as shown in Fig. 4.16(a). To maximize the power of LSM_{01} mode at frequency 60 GHz, we used the following objective function.

$$\text{Minimize } C = 1 - |S_{21}|^2 \qquad (\text{at } 60 \text{ GHz}) \tag{4.3}$$

In order to achieve the broadband property more stably we proposed an interesting objective function as given below. The proposed objective function is more general one and not limited to the design of Z-bend guide. To compute the random frequency, we used a random function to select a number between 0 and 1 and $\mathrm{RND}_{\mathrm{MAX}}$ function is also used for the normalization.

$$\text{Minimize } C = 1 - |S_{21}(f)|^2 \tag{4.4}$$

$$f = f_{\min} + (f_{\max} - f_{\min}) \times \mathrm{random}()/\mathrm{RND}_{\mathrm{MAX}}$$

$$(f_{\min} = 59 \text{ GHz},\ f_{\max} = 62 \text{ GHz})$$

The optimized structures and propagation fields of both Z-bend devices are shown in Fig. 4.16(b,c) and Fig. 4.17 respectively. The proposed objective function randomly selects the frequency in the range of 59–62 GHz for each generation of GA to avoid degradation of device performance at unconsidered frequency. Using this function, we achieved almost ideal broadband property from 59 to 63 GHz as shown

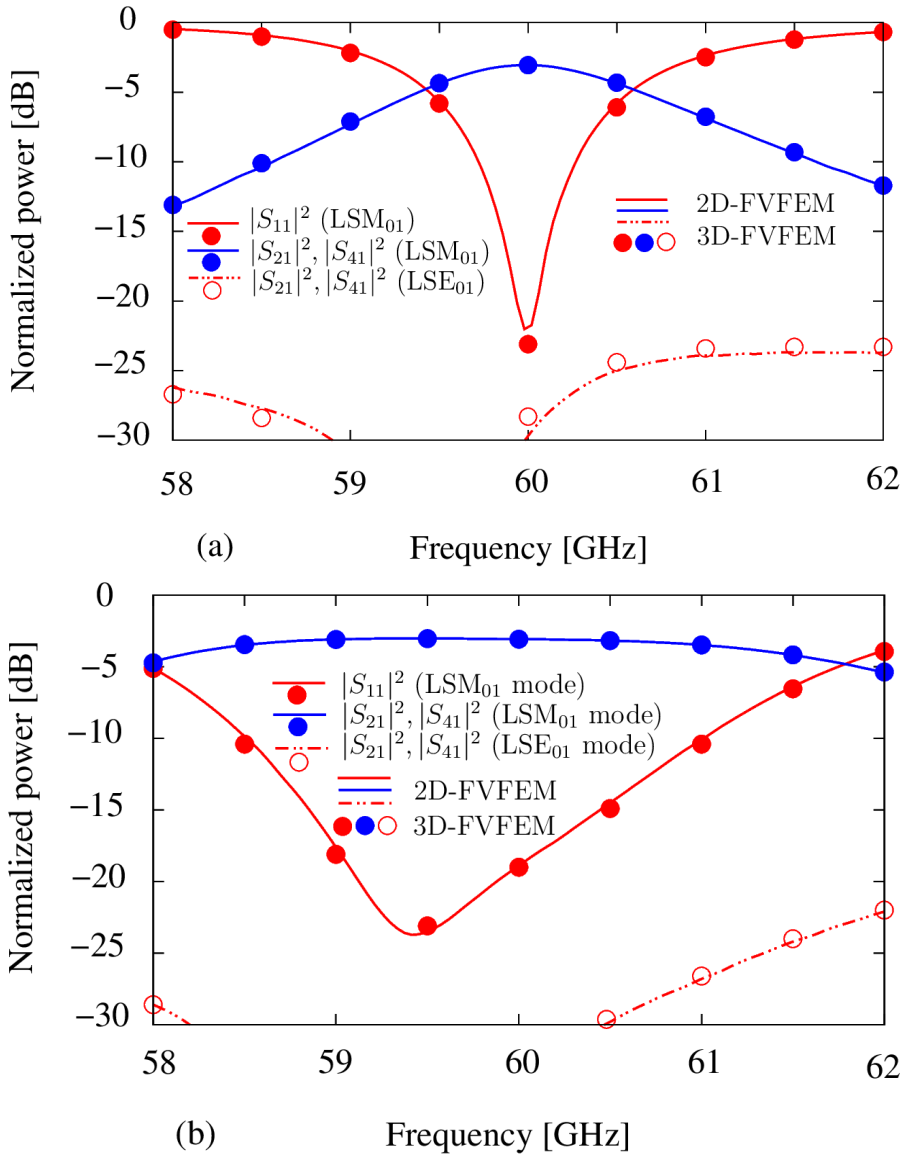

Figure 4.14: Frequency characteristics of NRD T-branch waveguide (a) At operating frequency 60 GHz and (b) broadband operation.

in Fig. 4.18(b). The considered objective function does not guarantee to achieve broad bandwidth for other NRD guides but in case of Z-bend its functioning well. The normalized power is $|S_{21}|^2 = 0.999$ at operating frequency 60 GHz as shown in Fig. 4.18(a). Figure 4.19 shows the calculated results of considered objective functions in term of minimum objective function value at different frequencies. Due to simple in structure Z-bend guide at 60 GHz converge very smoothly even from starting to the completion of generations. However, in case of broadband

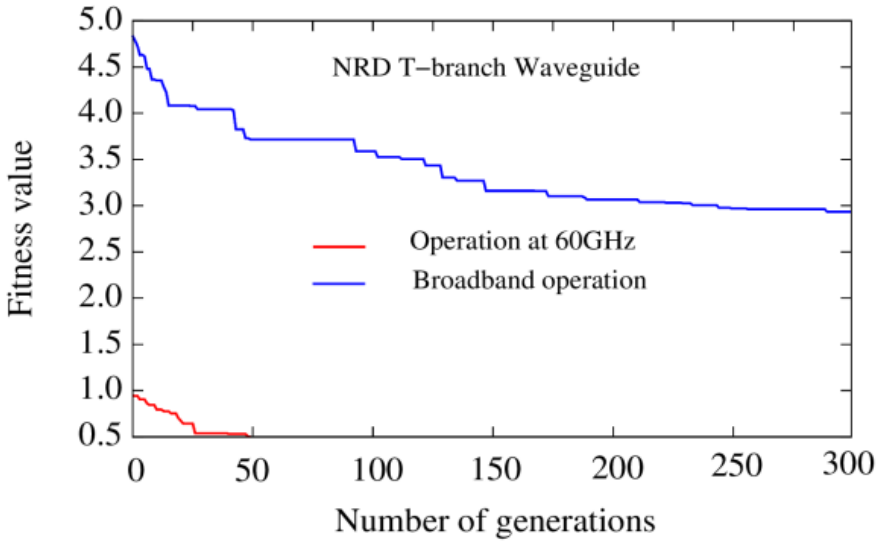

Figure 4.15: Convergence behavior of NRD T-branch waveguide.

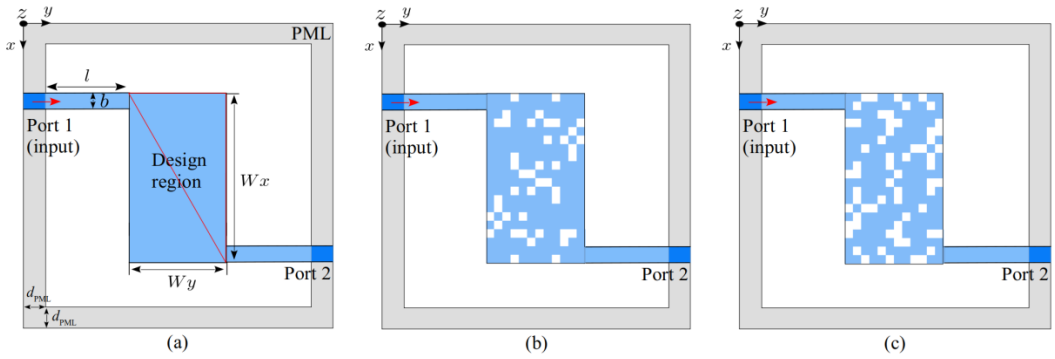

Figure 4.16: NRD Z-bend waveguide. (a) Initial design model, (b) optimized structure at 60 GHz, and (c) optimized structure for broadband operation.

operation, it shows the abrupt changes in fitness values along number of generation due to random selection of frequencies in the range of 59–62 GHz. We can see that in Fig. 4.19 the convergence is almost same from 40 number of generations to till 85 although frequencies are different. Therefore, to increase the generations will be not effective except consumption of time because it will show the same convergence behavior except some particular frequency points. The developed genetic algorithm is more efficient and appropriate choice for single frequency or broadband operation as compared to the DBS algorithm. In spite of several advantages the developed GA is not so stable. Sometime GA does not converge the solution quickly and satisfy

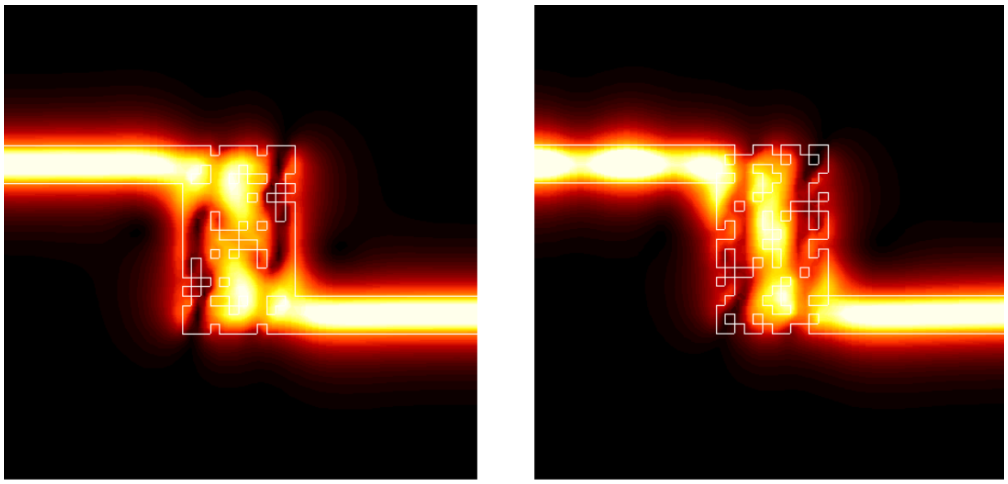

Figure 4.17: Propagation fields of NRD Z-bend waveguides (a) At operating frequency 60 GHz and (b) broadband Z-bend guide at 60 GHz.

the desired properties. Hence, highly efficient, sensitive and more stable optimal design approaches are required for more complex device functionalities. In the next chapter, we will discuss a class of binary evolutionary approaches including GA with the improvement of parallelization computation.

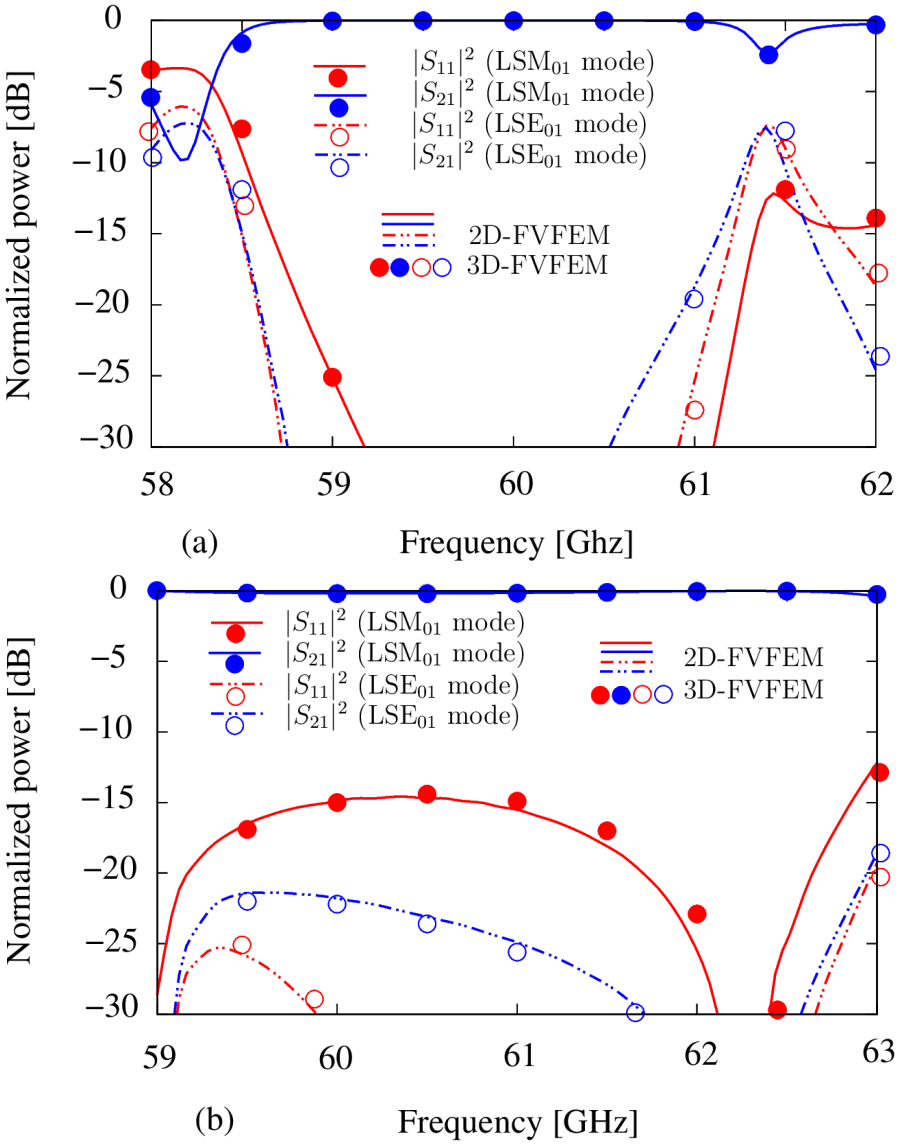

Figure 4.18: Frequency characteristics of NRD Z-bend waveguide. (a) At operating frequency 60 GHz and (b) broadband operation.

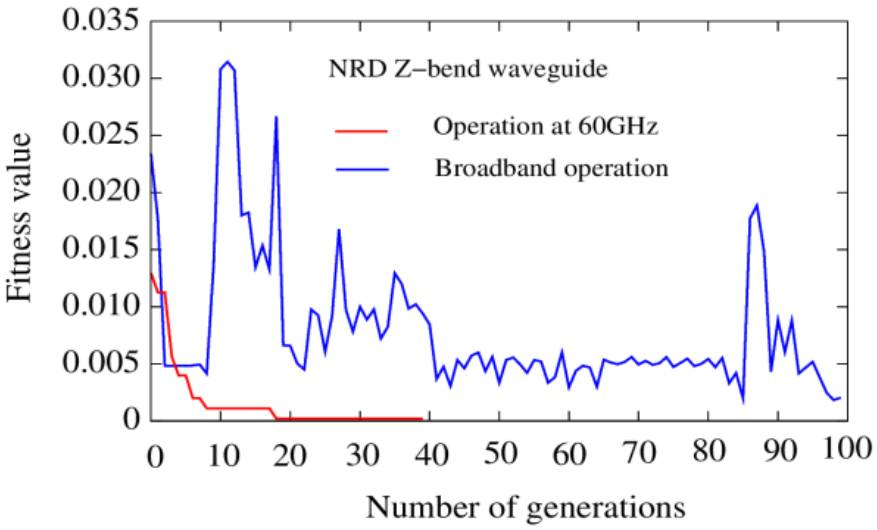

Figure 4.19: Convergence behavior of NRD Z-bend waveguide.

Chapter 5

Binary Evolutionary Approaches for NRD Guide Devices

In the preceding chapter, we developed a direct binary search algorithm which is not too efficient for complex NRD guiding structure or device functionalities. In this chapter, we present more sensitive and sophisticated optimal design approaches based on mosaic optimization concept for NRD circuit to realize the high-performance compact millimeter-wave integrated circuit as shown in the Fig. 4.1 of previous chapter. Several optimization approaches and variants based on size, shape, topology, and mosaic optimization concepts, such as genetic algorithm, particle swarm optimization, inverse design algorithm, and direct binary search algorithm, have been proposed for the efficient design of optical, dielectric, and photonic crystal guide devices [76]-[83]. However, a study about the development of optimal design approaches using the above-mentioned optimization concepts for NRD guides is insufficient.

To the best of our knowledge the development of binary evolutionary approaches based on mosaic optimization concepts, detailed implementation procedure, comparative study, and high performance NRD circuit components at single frequency operation and broadband operation, has not been presented previously. Therefore, we have developed several optimization approaches for the efficient design of NRD guide components with various functions. For this purpose, digital material concept (mosaic-optimization) using binary evolutionary approaches is very useful. Using mosaic-based optimization a small number of variables are used to express the design region of NRD guide and those variables are optimized by five optimization approaches. Binary representation-based genetic algorithm, dif-

ferential evolution algorithm, harmony search algorithm, firefly algorithm, and particle swarm optimization are developed to efficiently optimize the pixel pattern in the design region of NRD guide devices. To demonstrate the usefulness of these population-based optimizations, four NRD circuit components are designed which include low crosstalk waveguide crossing, T-branch power splitter, bending waveguide, and frequency demultiplexer. In addition, the same NRD guide components except frequency demultiplexer are also designed at wideband operation. In order to improve the design efficiency, 2D-FV-FEM is employed for the numerical simulations. This chapter demonstrates the detailed implementation procedure of developed evolutionary, comparative study of optimization approaches, and proposed highly attributed NRD circuit components for the realization of NRD based high-performance compact millimeter wave circuit.

5.1 Evolutionary Approaches for Binary Optimization

In evolutionary approaches, three processes are involved in the evolution of the population. The first step is initialization, which involves randomly generating an initial population of individuals based on a predetermined quantity. Determining an appropriate population size and individual representation technique that are more likely to offer feasible solutions are important. Another important parameter is the number of iterations. Both the population size and the number of iterations may have a significant impact on solution quality and time. After a few trials, an appropriate selection of these parameters can be determined based on the design problem resulting in a feasible solution. Individuals can be represented using a variety of ways, including binary representation, real value representation, and integer value representation.

The second step is to calculate the value of each individual using a problem-dependent objective function after the population has been randomly generated. The calculated value can be used to rank each individual for selection purposes. Whether the breaking criteria has been satisfied is judged after the evaluation of objective function. Different breaking criteria, such as static, dynamic, and hybrid, are used to stop the optimization process. When dynamic criteria are used, the optimization is executed until the desired characteristics is achieved, whereas the optimization is terminated at a fixed number of iterations in the case of static

criteria. A combination of these two criteria is called a hybrid and is used in some cases. If no individual satisfies the desired property, the third stage of the evolutionary technique generates a new population by perturbation of solutions in the existing population. In evolutionary approaches, three processes are involved in the evolution of the population. The generic optimization procedure of our binary evolutionary approaches that we considered in this paper is shown in Fig. 5.1.

In these optimizations, the size of population (Np = 64) is same for all evolutionary approaches. The starting search point is varies from one another due to the random generation of populations, resulting in differing optimal structures. The number of iterations required may be determined by the device function, whether it is designed for single frequency operation or wideband operation. For single and broadband operation, we evaluated a maximum of 100 and 300 iterations for all devices, respectively. Binary representation is considered to represent an individuals structure because the digital material concept is employed to generate a mosaic-like structure. The optimization process is terminated by using static breaking criteria.

5.1.1 Binary Genetic Algorithm (BGA)

John Holland proposed GA, a metaheuristic global search optimization method, in 1975 [84]. Conventional GA and its variants are used to solve a wide range of complex optimization problems. The basic goal of GA is to simulate natural selection and survival of the fittest individuals. The random generation of the initial population is the first step in GA optimization. It should be emphasized that a large population slows down the optimization process, whereas a small population may not be suitable for a mating pool. As a result, multiple trials are required to determine the appropriate size. To optimize the design region of the NRD guide, a random population is formed that has a set of individuals, also known as chromosomes, encoded by digital technique. Each individual is a mosaic-like structure made up of a set of pixels (called a gene) arranged in the form of 1 and 0.

After the population is randomly generated, the objective function calculates each individual quality and then assigns a rank to each individual based on the calculated value. GA is a method for generating new populations that mimics natural selection of individuals, and it employs three biologically inspired operators: selection, crossover, and mutation. Selection is a procedure to update the generation

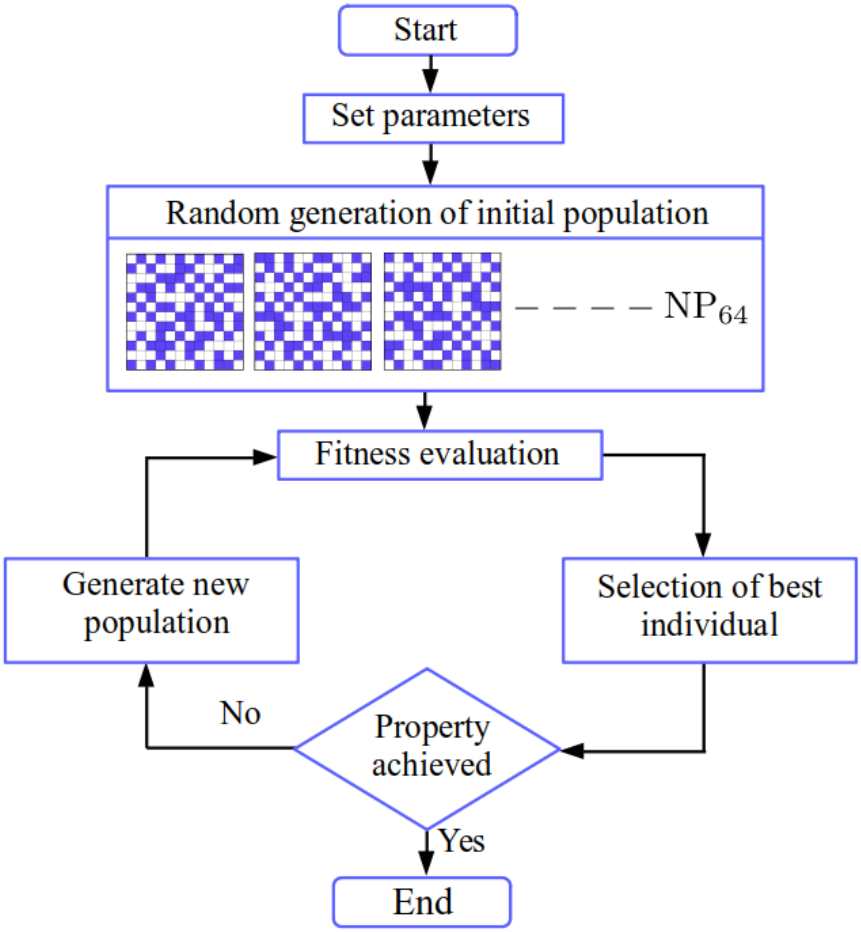

Figure 5.1: Generic work procedure of binary evolutionary methods.

by replacing the highly fit individuals with previous ones those are poor in fitness value. Individuals are selected for later mating through crossover and mutation in the first stage of evolution. The developed optimization method considers two different selection techniques. To save the best individual from the entire population, first elite selection is used. On the other hand, rank selection, is used to select the best individuals for a new generation. Once the parent individuals $\boldsymbol{x}_{p1}^{(n)}$ and $\boldsymbol{x}_{p2}^{(n)}$ are selected, the crossover operator perturbs the selected individuals to produce new offspring as follows:

$$x_{c,k}^{(n+1)} = \begin{cases} x_{p1,k}^{(n)} \; U(0,1) \leq 0.5 \\ x_{p2,k}^{(n)} \; \text{otherwise} \end{cases} \tag{5.1}$$

where $U(0,1)$ is a random number between 0 and 1 and $x_{i,k}^{(n)}$ denotes k-th component of the design variable vector $\boldsymbol{x}_i^{(n)}$. Crossover is a significant part of GA, in which

two individuals mate and exchange some bits to create a new individual with some attributes that are identical to the parents. Our optimal design approach used uniform crossover technique in which each pixel is randomly chosen from one of the corresponding pixels of the parent individuals. After crossover, the newly generated offspring have a tendency to become highly similar to previously selected individuals. Mutation is a third operator in evolutionary process of GA that is used to maintain the genetic diversity from one population to the next and to avoid local minima by preventing population of individuals from becoming too similar. There are several types of mutation operators, but we employed bit flip mutation to inject diversity into the population to avoid stagnation. A bit flip mutant is the inverting of bits according to a preset probability to create a unique individual. With this optimization approach, the mutation rate is 1%. The evolution of a randomly generated population is now complete. This search process is repeated until the number of iterations is reached. Finally, the best individual at the final iteration will be the optimal mosaic-like structure of the NRD guide.

5.1.2 Binary Differential Evolution Algorithm (BDEA)

DEA is a metaheuristic optimization approach, and first proposed by Storn and Price in 1995 for global optimization [85]. Usually, DEA performs better than GA because it explores the given search space more efficiently, when multi objectives are need to be optimized. The key reasons for differential evolution application in electromagnetic optimization are its reliability in dealing with multi-minima functional and its improved rate of convergence as compared to GA when applied to small scale real valued problem. It is critical to improve the candidate solution with each iteration, and it doesn't require explicit cost function gradients in the candidate solution search space. As a result, DEA can be applied to problems that are not even continuous or non-differentiable. The most important feature of DEA is its unique mutation operation. The scaling parameter S and the population size N_P are two critical control parameters in DEA. The key steps in the implementation of DEA are mutation, crossover, and selection. First, in binary strategy, a mutant individual is generated as follows:

$$x_{m,k}^{(n)} = \begin{cases} x_{p1,k}^{(n)} + (x_{p2,k}^{(n)} - x_{p3,k}^{(n)})\, U(0,1) < S \\ x_{p1,k}^{(n)} \quad \text{otherwise} \end{cases} \tag{5.2}$$

where $x_{m,k}^{(n)}$ is a mutant individual and may possible to take the value of other than binary number -1 or 2 if the values of randomly selected individuals are ($x_{p1,k}^{(n)}$, $x_{p2,k}^{(n)}$, and $x_{p3,k}^{(n)}$) = (0, 0, 1) or (1, 1, 0) respectively. In order to binarize the mutant individual the value of $x_{m,k}^{(n)}$ is set to be (0, 1) as follow.

$$x_{m,k}^{(n)} = \begin{cases} 0 \ (x_{m,k}^{(n)} < 0.5) \\ 1 \text{ else} \end{cases} \tag{5.3}$$

The scaling parameter S is used to control the differential variations and it is set to be 0.75. The operation described above is called the mutation of DEA. The second step of DEA is crossover. In DEA, $\boldsymbol{x}_t'$ is the candidate of next generation by crossover between mutant individual $\boldsymbol{x}_m^{(n)}$ and target individual $\boldsymbol{x}_t^{(n)}$.

$$x_{t,k}' = \begin{cases} x_{t,k}^{(n)} \ \ (U(0,1) < 0.5) \\ x_{m,k}^{(n)} \text{ otherwise} \end{cases} \tag{5.4}$$

Then $\boldsymbol{x}_t'$ is used as $\boldsymbol{x}_t^{(n+1)}$ if $\boldsymbol{x}_t'$ is better than $\boldsymbol{x}_t^{(n)}$, otherwise $\boldsymbol{x}_t^{(n)}$ is restored. The third step of DEA is to select the best individual between target individual and candidate individual for next round until the completion of iteration.

5.1.3 Binary Harmony Search Algorithm (BHSA)

HSA is a population-based metaheuristic optimization approach proposed by Geem et al. in 2001 [86]. HSA is inspired by the improvisation process of experienced musicians. The key benefits of HSA are its clarity of execution, record of success, and ability to solve a variety of complex problems. Pitch adjustment rate, bandwidth, and harmony memory considering rate are the three main parameters that control exploitation and exploration in HSA. Through the selecting and tuning process, a new harmony is created in HSA. Each design variable is chosen from the harmony memory, which contains previous good harmonies. A random number, with a specified probability, tunes or replaces the selected harmony. The new harmony $\boldsymbol{x}_h^{\text{new}}$ is generated as follows:

$$x_{m,k} = x_{p1,k} + x_{p2,k} + x_{p3,k}$$

$$x_{h,k}^{\text{new}} = \begin{cases} (U(0,1) < 0.5)?\ 0:1\ (C_h < (1 - R_{\text{hmcr}}) \\ (x_{m,k} = 0 \text{ or } 2)?\ 0:1\ (\text{C}_\text{h} < (1 - \text{R}_\text{hmcr}) \\ \qquad\qquad\qquad\qquad (1 + R_{\text{par}}) \\ (x_{m,k} \leq 1)?\ 0:1\ \text{ otherwise} \end{cases} \tag{5.5}$$

where $C_h = U(0,1)$ and $x_{m,k}$ is k-th sound generated in considering harmony memory. R_{hmcr} is the harmony memory considering rate (HMCR), and it is utilized to make the harmony memory more effective. If the HMCR value is very low, close to 0, only a few harmonies are used, and therefore the convergence rate is slow, whereas large rates exploit the harmonies, and the solution space is not fully explored, thus leading to an insufficient solution. The value of HMCR should be in the range of 0.7-0.95. In this optimization approach the R_{hmcr} = 0.85 has been set. The pitch adjustment rate R_{par}, is used to control the degree of adjustment. Because of the limitation in exploring only a small subspace of the entire subspace, a small R_{par} with narrow bandwidth can slow down HSA convergence, whereas a large R_{par} with a wide bandwidth can lead to optimization deviation in some optimal solutions. In this optimization approach, the pitch adjustment rate is set to be R_{par} = 0.2.

5.1.4 Binary Particle Swarm Optimization (BPSO)

PSO is an iterative optimization approach that takes its inspiration from the animal kingdom, specifically a group of animals moving in search space for common objective. Dr. Eberhart and Dr. Kennedy were the first to suggest PSO [87]. In PSO, a swarm of particles is the first to be randomly initialized. Each particle has its own unique position and velocity. Each particle changes its position continuously inside a specified search space with velocity to find the optimal location. The particles movement is determined by its memory path and iteration with other particles. The best position of each particle and the best position of the swarm are updated once all particles have reached the new place. PSO finds the best solution by collaborating and sharing information among swarm particles. The following are the steps in the PSO procedure:

1. Generate an initial swarm with initial position and velocity.
2. Evaluate objective function of each particle.
3. Update both the individual and global best positions.

4. Update each particle velocity and position.

The optimization process is repeated until the termination criterion is met. The following equations are used in PSO to update the position and velocity of the particles.

$$\boldsymbol{y}_i^{(n+1)} = \boldsymbol{y}_i^{(n)} + \boldsymbol{v}_i^{(n+1)} \tag{5.6}$$

$$\boldsymbol{v}_i^{(n+1)} = W\boldsymbol{v}_i^{(n)} + C_1 r_1(\boldsymbol{y}_p^{(n)} - \boldsymbol{y}_i^{(n)}) + C_2 r_2(\boldsymbol{y}_g^{(n)} - \boldsymbol{y}_i^{(n)}) \tag{5.7}$$

$$\boldsymbol{x}_i^{(n+1)} = \text{binarize}(\boldsymbol{y}_i^{(n+1)}) \tag{5.8}$$

where $\boldsymbol{y}_i^{(n)}$ and $\boldsymbol{v}_i^{(n)}$ are the position and velocity of i-th particle respectively, while $\boldsymbol{y}_p^{(n)}$ and $\boldsymbol{y}_g^{(n)}$ are the individual and global best positions of n-th iteration respectively. W is the inertial weight parameter with a value 0.8 that adjusts the ability to search locally and globally. The initial cognitive and social cognitive coefficients, C_1 and C_2 can adjust the balance between individual and global optimum positions. r_1 and r_2 are two random values between 0 and 1 which are used to simulate the random components of swarm behavior. To obtain $\boldsymbol{x}_i^{(n+1)}$, the following binarization scheme is employed:

$$x_{i,k}^{(n+1)} = \begin{cases} 1 & \left(\dfrac{1}{1+\exp(-y_{i,k}^{(n+1)})} + \Delta U(-1,1) > 0.5 \right) \\ 0 & \text{otherwise} \end{cases} \tag{5.9}$$

where Δ is a coefficient introduced to avoid being trapped in a local solution and is set to be $\Delta = 0.125$.

5.1.5 Binary Firefly Algorithm (BFA)

FA is a swarm-based metaheuristic optimization algorithm first proposed by Xin She Yang in 2008 [88]. FA is inspired by the movement of fireflies as they interact based on their flashing light. Regardless of their gender, particles are attracted to others because of their attractiveness. Attractiveness is determined by brightness and distance between them. The optimization process of FA consists of three steps. First, a particles called fireflies are randomly generated. Each firefly has a brightness level. The brightness is used to calculate the value of each firefly by using objective function. For minimization problem, the fireflies with small value are more brighter than higher ones. Once brightness of fireflies is evaluated, then

fireflies follow those ones who are rich in brightness. The brightest firefly conducts a local search by moving randomly in its surroundings. The position of firefly $\boldsymbol{y}_i^{(n)}$is updated by equation as follow:

$$\boldsymbol{y}_i^{(n+1)} = \boldsymbol{y}_i^{(n)} + \sum_j u\left(\beta_{0,j} - \beta_{0,j}\right)\beta_{0,j}e^{-}\gamma r_{ij}^2\left(\boldsymbol{y}_j^n - \boldsymbol{y}_i^n\right) + \alpha\delta^n\varepsilon \tag{5.10}$$

$$\boldsymbol{x}_i^{(n+1)} = \text{binarize}(\boldsymbol{y}_i^{(n+1)}) \tag{5.11}$$

The attraction to the brighter neighbor is calculated using the second term of the above equation where, $\beta_{(0,j)}$ is attractive force of the j-th particle and r_{ij} is a distance between i-th and j-th particles. $u(\xi)$ is the unit step function. $\boldsymbol{y}_i^{(n)}$ and $\boldsymbol{y}_j^{(n)}$ are the positions of fireflies at n-time. The light absorption coefficient of medium is $\gamma = 1/\sqrt{L}$ and L is used to adjust the search range of particles. The third term in the above equation is for randomization, where α is the scaling factor used to adjust the random step length, δ is the damping factor and $\boldsymbol{\varepsilon}$ is a random vector. The values of δ and α are 0.99 and 0.25, respectively. Using the above equation, the firefly's position is updated before the end of iterations.

5.2 Design Examples of NRD Guide

To demonstrate the usefulness of these optimization approaches, we considered four numerical examples of NRD guide devices. Except symmetrical conditions in design region, size of design region, position and number of output ports, the other basic geometrical parameters are the same in all devices. In our design examples, we assume the spacing between metal plates is $a = 2.2\,\text{mm}$, length and width of the dielectric strip are $l = 10\,\text{mm}$ and $b = 2\,\text{mm}$, respectively. The relative permittivity of dielectric and air is $\varepsilon_r = 2.2$ and $\varepsilon_{\text{air}} = 1.0$ respectively. The size of design region in waveguide crossing, T-branch power splitter and bending waveguide is $W_x = W_y = 6\,\text{mm}$ and it is discretized into 144 pixels. In case of frequency demultiplexer $W_x = 6\,\text{mm}$ and $W_y = 16\,\text{mm}$ with total 384 pixels in the design region. The size of each pixel is $0.5\,\text{mm} \times 0.5\,\text{mm}$ that is quarter of the dielectric strip. In order to make the fabrication feasible, pixel size is determined by considering the operating wavelength, guide width and fabrication sensitivity. The computational domain is surrounded by a perfectly matched layer (PML) with

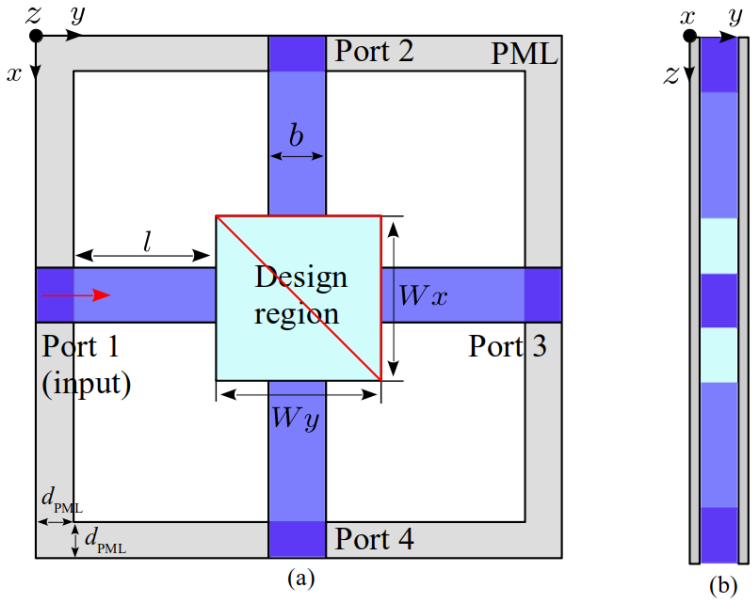

Figure 5.2: Initial structure of NRD waveguide crossing (a) top view (b) front view.

a thickness of $d_{\mathrm{PML}} = 5$ mm. LSM_{01} mode at 60 GHz is incident at input port 1 in first three examples. In case of frequency demultiplexer wave at two frequencies 59 GHz and 61 GHz are incident, and it is selectively output to port 2 and 3 respectively. In order to achieve the desired properties, the design region of size $W_x \times W_y$ is optimized.

5.2.1 Low Crosstalk Waveguide Crossing

First, we consider low crosstalk NRD waveguide crossing as shown in Fig. 5.2. The geometrical parameters and incident conditions are explained above. In order to make the optimization process easy and faster, a unique one-two structural symmetric conditions are applied in the design region indicated by red line, to optimize the half design region except whole as shown in Fig. 5.2. The following objective function is used at 60 GHz to achieve the maximum transmission efficiency at output port 3 when LSM_{01} mode is incident at input port 1.

$$\text{Minimize } F = 1 - |S_{31}(f)|^2 \quad (\text{at } 60 \text{ GHz}) \tag{5.12}$$

The pixel pattern is optimized by using five different optimization that are described in above section. The convergence behavior of these optimization approaches at 60 GHz is shown in Fig. 5.3. We can see that all optimization approaches show

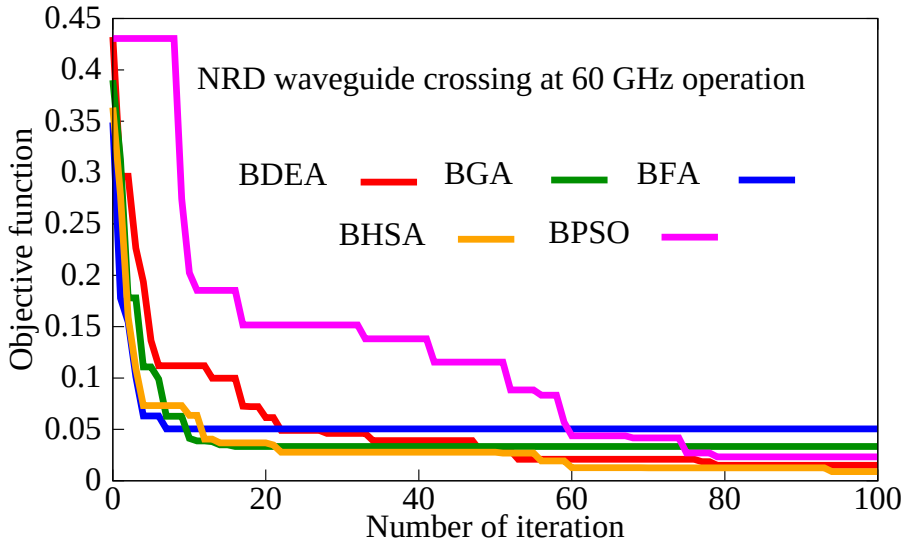

Figure 5.3: Convergence behavior of NRD waveguide crossing at 60 GHz.

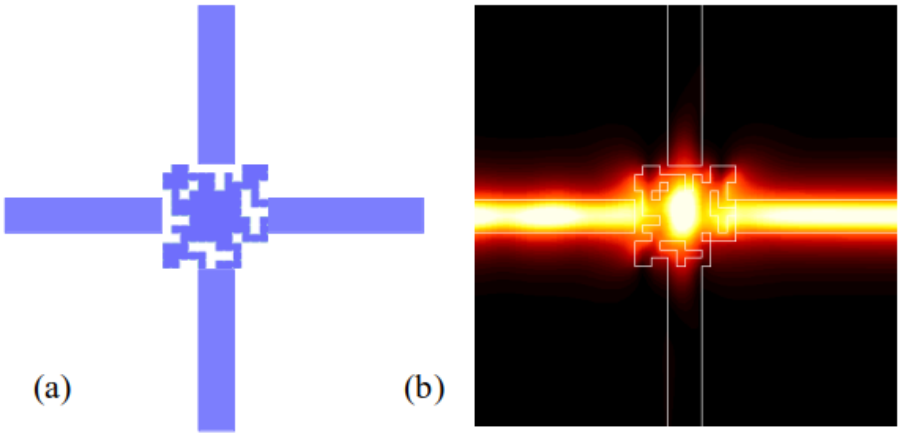

Figure 5.4: Optimal results of waveguide crossing at 60 GHz using BHSA (a) optimized structure and (b) propagation field.

good convergence in the range of 60 to 80 number of iterations. The performance of BHSA and BDEA is slightly better, but other optimizations also achieved sufficient device performances. Figure 5.4 and 5.5 shows the optimized structure, propagation field, and frequency characteristics of BHSA which is the best one in case of waveguide crossing at 60 GHz operation. The frequency characteristics of waveguide crossing using other optimizations are shown in Fig. 5.6. Due to random generation of initial population in each optimization the optimal structures are different to each other. Although, optimized structures are different but overall

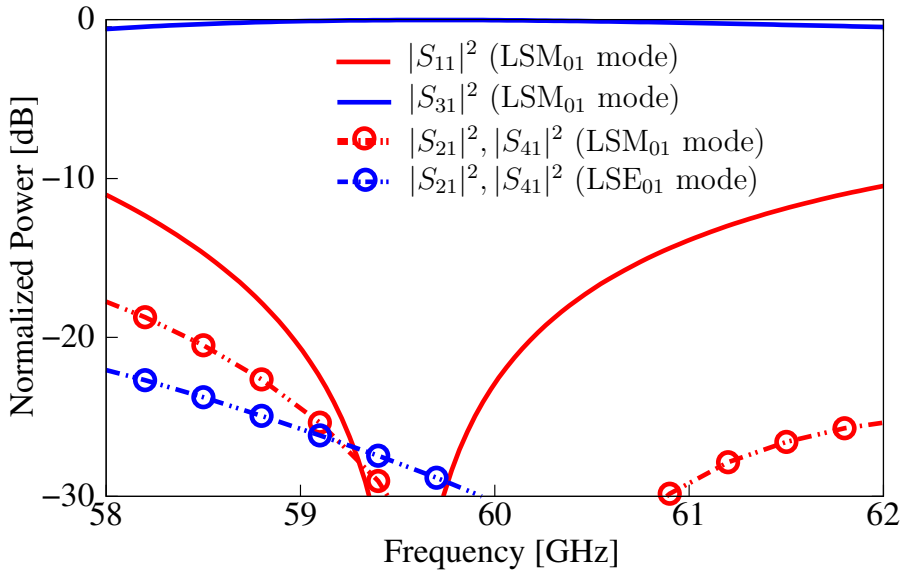

Figure 5.5: The frequency characteristics analysis of NRD crossing waveguide using BHSA.

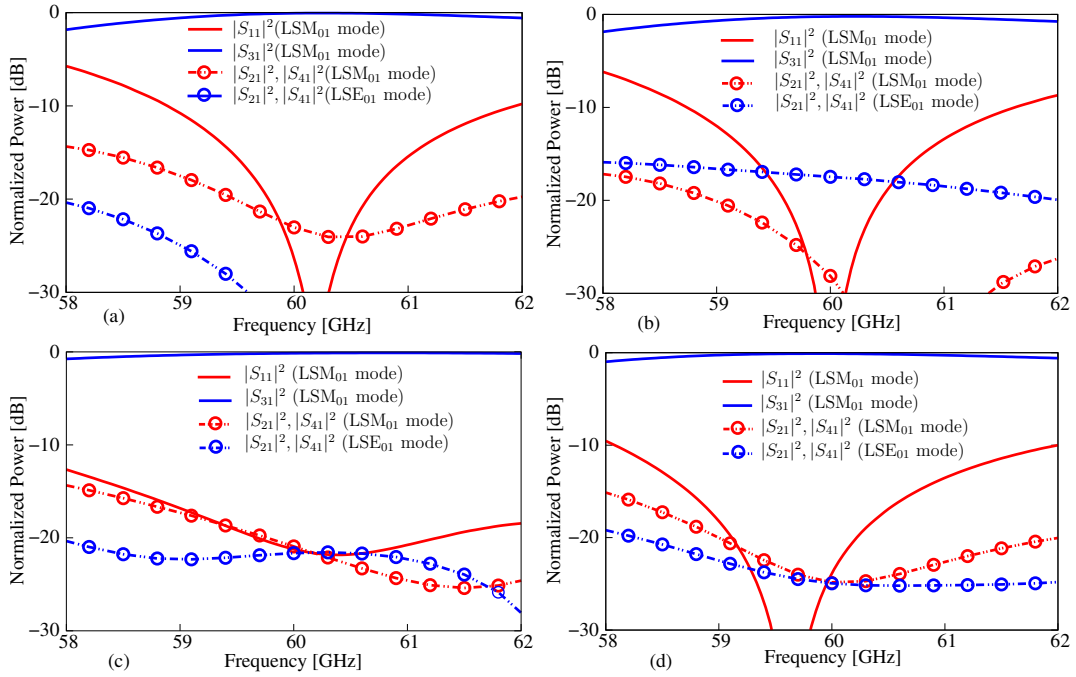

Figure 5.6: Frequency characteristics analysis of waveguide crossing at 60 GHz operation (a) BDEA (b) BFA (c) BGA (d) BPSO

device performance is almost same for each design as shown in Fig. 8. All optimized waveguide crossings achieve high transmission power more than 0.95. In Fig. 5.5, frequency analysis by BHSA relatively show broad bandwidth character-

istics. By considering this clue, we modified our objective function to realize the broadband operation possible. In order to achieve the broader bandwidth, we used the following modified objective function.

$$\text{Minimize } F = \frac{1}{3}\sum_{i=1}^{3}\left(1 - |S_{31}(f_i)|^2\right) \tag{5.13}$$

$$(f_{1,2,3} = 58,\ 60,\ 62 \text{ GHz})$$

The updated objective function analyzes the waveguide structure using three different frequencies at a time for each generation of optimization approaches. Usually, a large number of iterations are required to optimize the structure for broadband operation because multiple frequencies involve in the objective function. In Fig. 5.7 we can see that how efficient our developed optimization approaches that converge the solution at broadband operation with almost same number of iterations used for single frequency operation. The optimized structure at broadband operation, propagation fields at considered frequencies in the objective function and frequency characteristic by BDEA are shown in Fig. 5.8 and Fig. 5.9. Furthermore, the performance detail of proposed NRD waveguide crossing is summarized in Table 5.1. By using modified objective function, all optimization approaches achieve high broadband property around 5 GHz in the frequency range of 58 GHz-63 GHz.

5.2.2 T-branch Power Splitter

Next, we considered second numerical example NRD T-branch power splitter as shown in Fig. 5.10. The geometric parameters are the same as in the previous example, except for the number of output ports and the condition for structural symmetry. In order to split the transmission power equally at output ports, one-two symmetric condition in rectangle form is applied indicated by red line as shown in Fig. 5.10. Due to considered symmetry, pixels in the upper half of the design region are optimized. The following objective function is used to achieve the maximum transmission power at 60 GHz.

$$\text{Minimize } F = 1 - |S_{21}(f)|^2 - |S_{41}(f)|^2 \quad (\text{at } 60 \text{ GHz}) \tag{5.14}$$

where $|S_{21}|^2$ and $|S_{41}|^2$ are transmission powers from port 1 to port 2 and port 1 to port 4 respectively. Figure 5.11 shows the convergence behavior of optimization

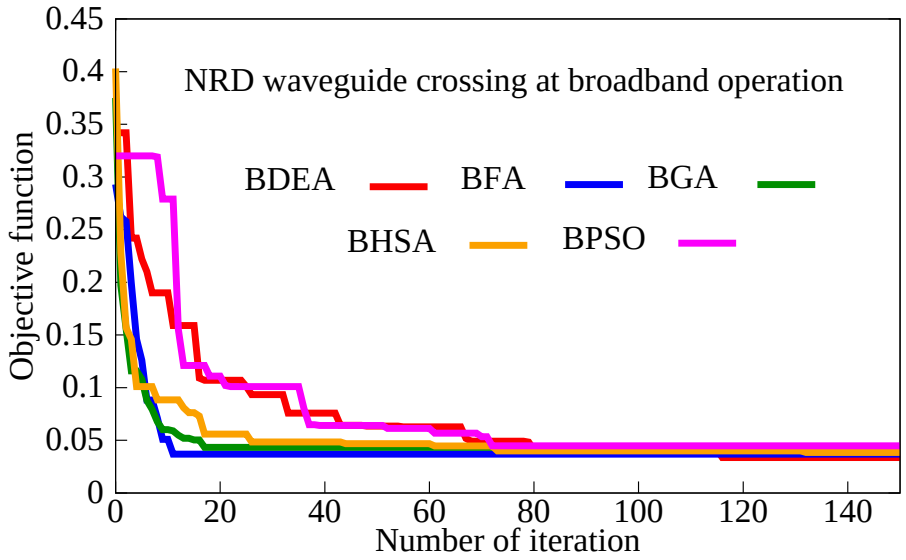

Figure 5.7: Convergence behavior of NRD waveguide crossing at broadband operation.

Table 5.1: Detail performance analysis of NRD waveguide crossing at 60 GHz and broadband operation

Crossing	**Transmission [dB]**		**Reflection [dB]**		**X-talk**
60 GHz	**LSM_{01}**	**LSE_{01}**	**LSM_{01}**	**LSE_{01}**	**[dB]**
BHSA	-0.03	-29.0	-22.8	-30.2	-50.4
BDEA	-0.06	-32.7	-26.3	-34.7	-33.8
BPSO	-0.10	-24.7	-23.8	-31.5	-32.6
BGA	-0.14	-34.6	-21.2	-24.0	-45.3
BFA	-0.22	-21.5	-53.5	-20.7	-28.1
Broadband	**Transmission [dB]**		**Reflection [dB]**	**X-talk**	**BW**
Crossing	**LSM_{01}**	**LSE_{01}**	**LSM_{01}**	**[dB]**	**[GHz]**
BDEA	-0.08	-31.2	-25.6	-29.5	5.0
BFA	-0.10	-37.9	-31.0	-44.9	5.0
BHSA	-0.12	-36.9	-25.5	-53.7	5.0
BGA	-0.12	-32.8	-25.5	-33.1	5.0
BPSO	-0.11	-42.2	-24.7	-53.6	5.0

approaches for T-branch guide at 60 GHz in which BDEA, BHSA, and BFA converge the solution very efficiently between 40 to 60 number of iterations. However, BGA requires more number of iterations for better convergence in comparison to BDEA, BHSA and BFA but it also achieves a desired device performance. The optimal structure, propagating field at 60 GHz and frequency characteristics of BHSA obtained by 2D-FVFEM are shown in Fig. 5.12 and Fig. 5.13, and it depicts that optimal structure can efficiently split the power equally into two output ports. The

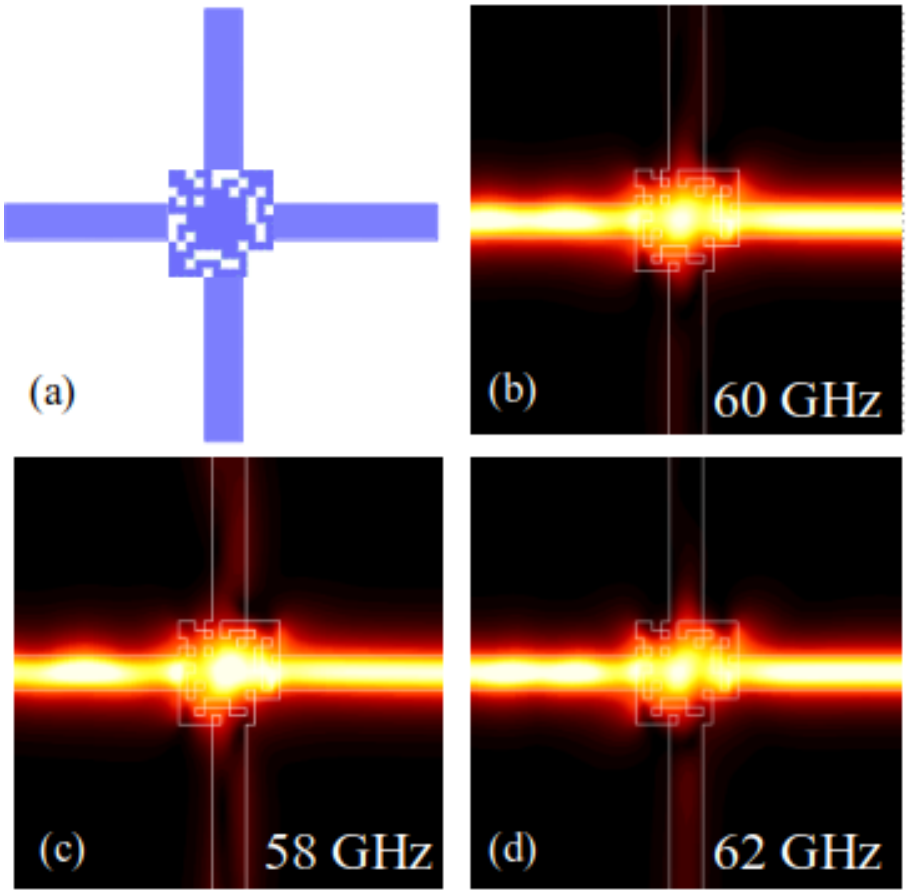

Figure 5.8: Optimal results of waveguide crossing at broadband operation using BDEA (a) optimized structure and (b-d) propagation field.

frequency characteristics of T-branch guide using other optimizations are shown in Fig. 5.14. The optimized structures by BDEA, BHSA, BGA, BPSO and BFA achieved high splitting power ratio at 60 GHz $|S_{21}|^2$= $|S_{41}|^2$ = 0.499, 0.496, 0.493, 0.491, and 0.488 respectively. Based on the convergence analysis at 60 GHz we considered all optimization approaches for broadband operation by using objective function as follow:

$$\text{Minimize } F = \frac{1}{5}\sum_{i=1}^{5} \left(1 - |S_{21}(f_i)|^2 - |S_{41}(f_i)|^2\right) \tag{5.15}$$

$$(f_{1,2,3,4,5} = 58,\ 59,\ 60,\ 61,\ 62 \text{ GHz})$$

In order to ensure the broad bandwidth, more close intervals within interested frequency band are considered in the objective function. Figure 5.15 show the

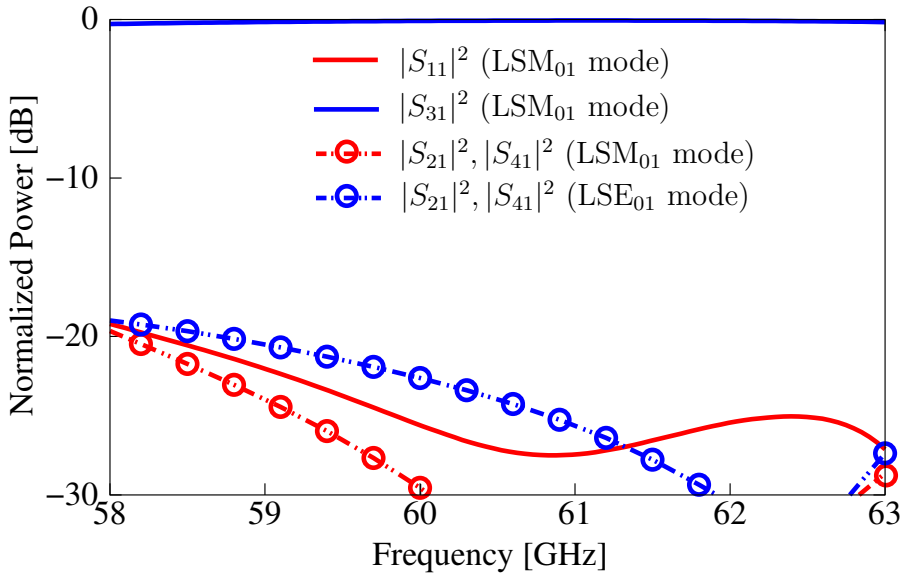

Figure 5.9: The frequency characteristics analysis of NRD crossing waveguide at broadband operation using BDEA.

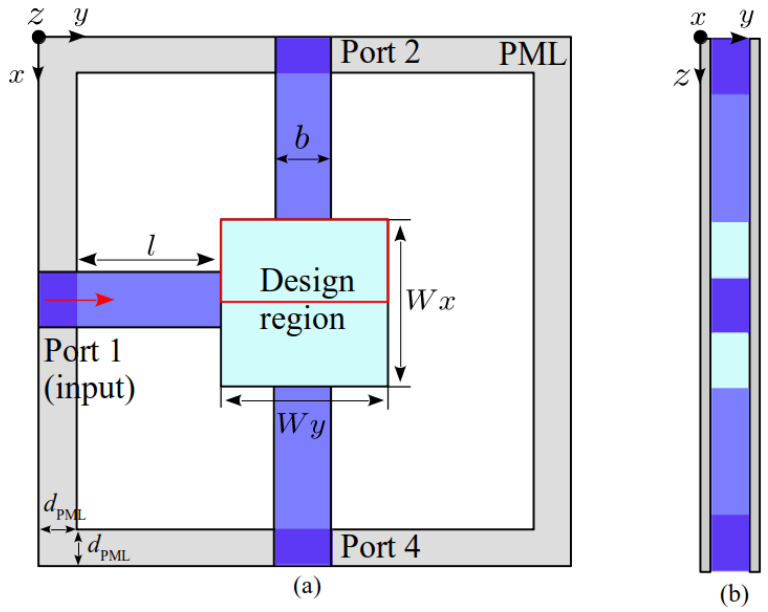

Figure 5.10: Initial structure of NRD T-branch power splitter (a) top view (b) front view.

convergence behavior at broadband operation and it shows almost same behavior and convergence order as in 60 GHz operation. In this design, BDEA, BHSA, and BGA achieved desired property around 25, 60 and 250 number of iterations. Due to structural limitations of T-branch guide, it is quite challenging for each

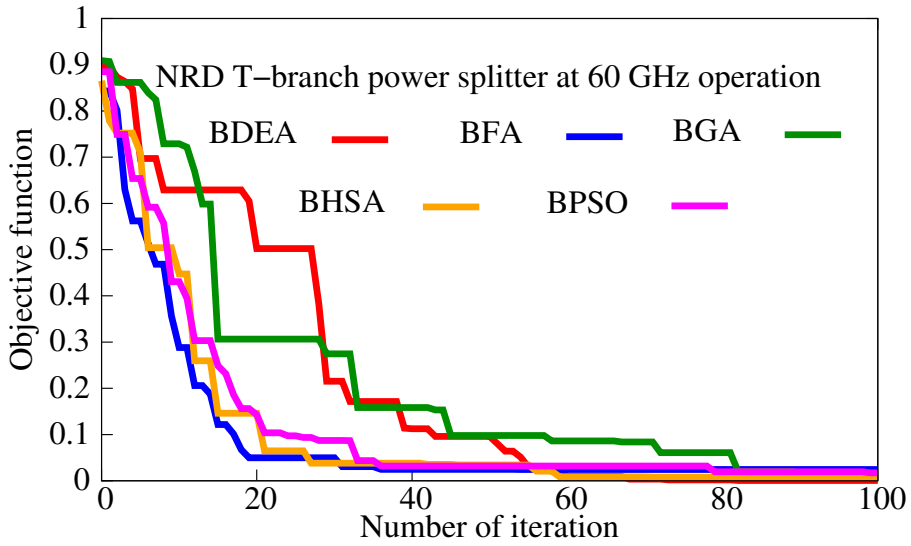

Figure 5.11: Convergence behavior of NRD T-branch power splitter at 60 GHz operation.

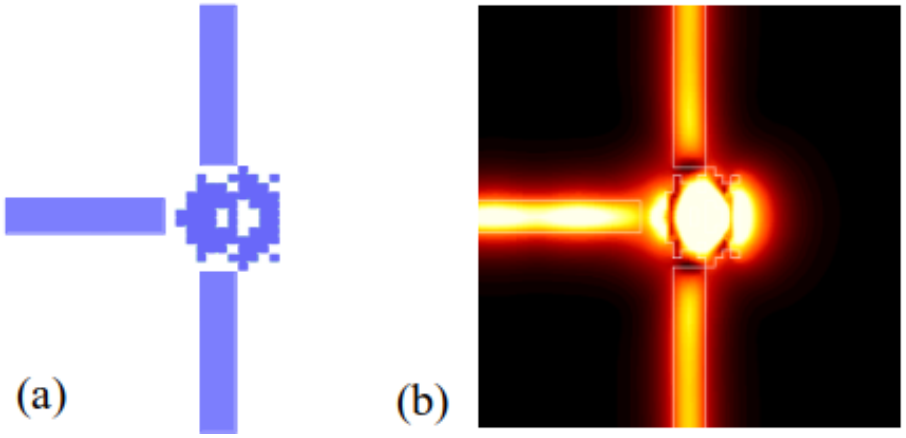

Figure 5.12: Optimal results of T-branch power splitter at 60 GHz using BHSA (a) optimized structure and (b) propagation field.

optimization approach to achieve a desired property. Therefore, the performance of BPSO and BFA is not satisfactory. Successful optimizations achieved same device performance with broad bandwidth around 4 GHz in the frequency range of 58 GHz-62 GHz, but BHSA and BDEA are more efficient than BGA. The best optimal results obtained by BDEA are shown in Fig. 5.16 and Fig. 5.17. Furthermore, the performance detail of proposed NRD T-branch power splitter is summarized in Table 5.2.

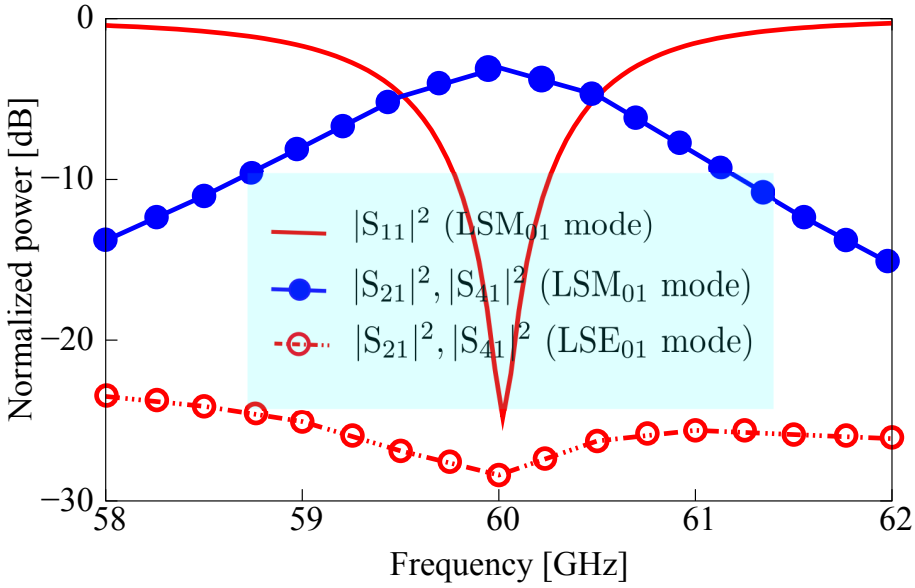

Figure 5.13: The frequency characteristics analysis of NRD T-branch power splitter using BHSA.

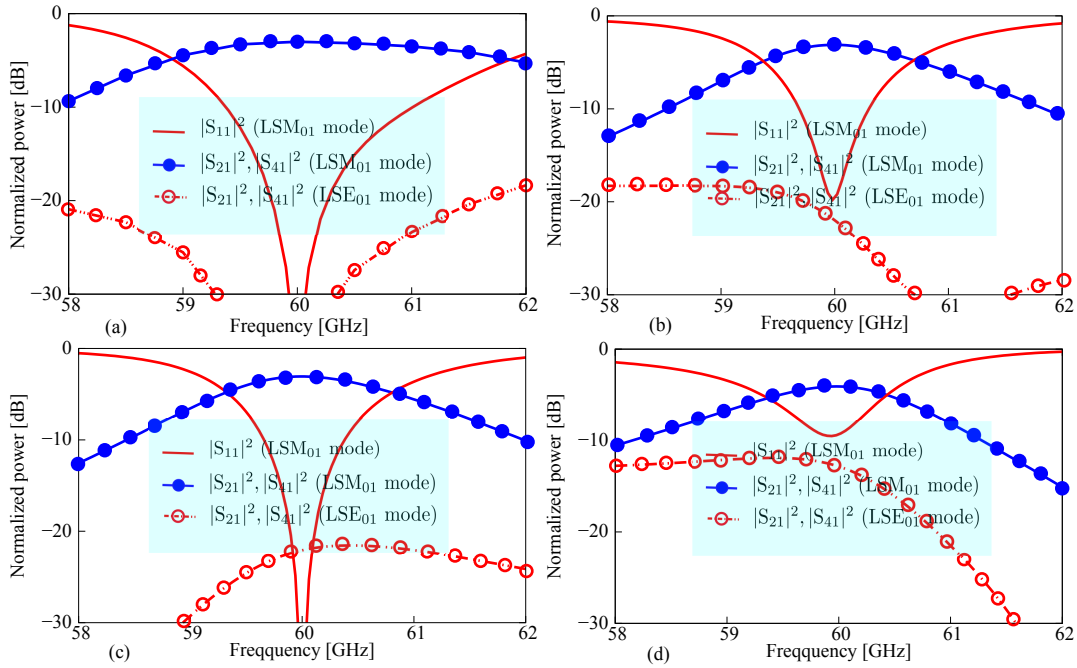

Figure 5.14: Frequency characteristics analysis of T-branch power splitter at 60 GHz operation (a) BDEA (b) BFA (c) BGA (d) BPSO.

5.2.3 Bending Waveguide

Next, we considered the third numerical example of an NRD bending waveguide as shown in Fig. 5.18. Except number of output ports, geometrical parameters

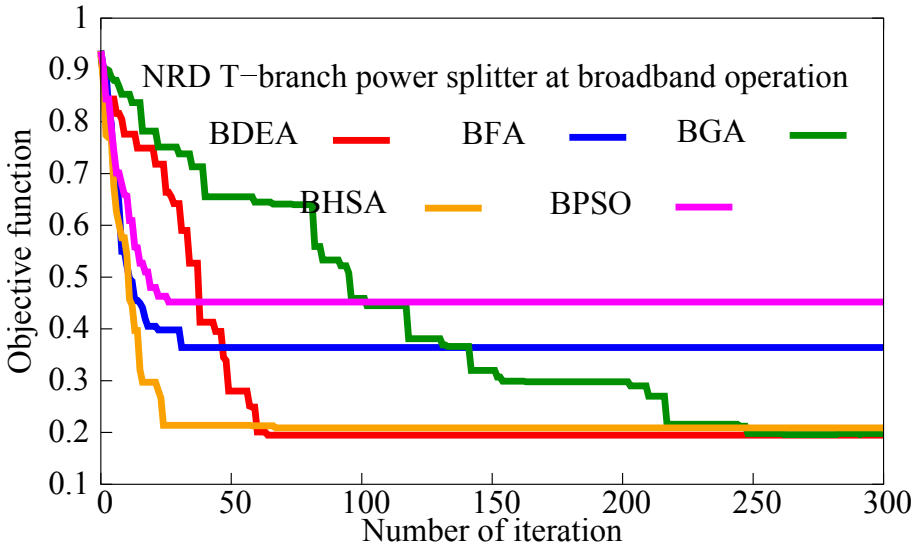

Figure 5.15: Convergence behavior of NRD T-branch power splitter at broadband operation.

Table 5.2: Detail performance analysis of NRD T-branch power splitter at 60 GHz and broadband operation

T-branch	**Transmission [dB]**		**Reflection [dB]**		**BW**
60 GHz	**LSM_{01}**	**LSE_{01}**	**LSM_{01}**	**LSE_{01}**	**[GHz]**
BDEA	−3.01	−36.0	−37.8	−53.4	−−
BHSA	−3.04	−28.3	−23.7	−51.1	−−
BGA	−3.06	−22.3	−62.0	−48.5	−−
BFA	−3.11	−21.9	−19.5	−52.7	−−
BPSO	−4.11	−12.7	−9.3	−43.9	−−
Broadband	**Transmission [dB]**		**Reflection [dB]**		**BW**
T-branch	**LSM_{01}**	**LSE_{01}**	**LSM_{01}**	**LSE_{01}**	**[GHz]**
BDEA	−3.12	−19.7	−22.2	−56.4	4.0
BGA	−3.04	−31.5	−21.3	−55.0	4.0
BHSA	−3.15	−19.2	−21.0	−56.0	4.0
BFA	−3.43	−17.7	−12.2	−53.6	−−
BPSO	−3.69	−19.5	−9.12	−48.7	−−

and structural symmetrical conditions are the same as in the example of waveguide crossing. For maximum transmission, the following objective function is used at a single operating frequency.

$$\text{Minimize } F = 1 - |S_{21}(f)|^2 \quad (\text{at 60 GHz}) \tag{5.16}$$

where $|S_{21}|^2$ is the transmission power at port 2. Figure 5.19 shows the convergence analysis of optimization approaches at 60 GHz in which BDEA, BHSA, BGA, and

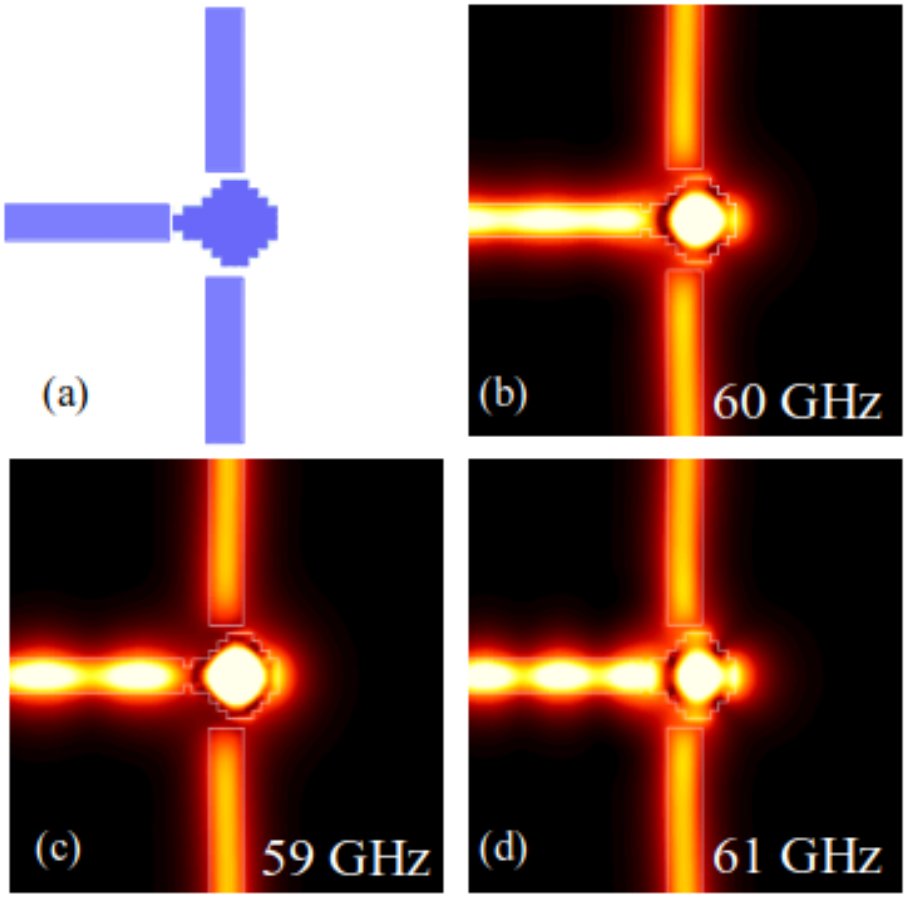

Figure 5.16: Optimal results of T-branch waveguide at broadband operation using BDEA (a) optimized structure and (b-d) propagation field.

BFA achieving the best convergence results not more than 60 iterations but as usual GA require more iterations confirmed in the previous example in both operation. Because of the sharp bending structure, it is challenging for each optimization approach to satisfy the desired properties. Figure 5.20 and Figure 5.21 shows the optimal results of a bending waveguide at 60 GHz using BHSA. The frequency characteristics of bending waveguide using other optimizations are also shown in Fig. 5.22. As shown in Fig. 5.21 and Fig. 5.22, the structures obtained by BDEA, BHSA, BGA, BFA, and BPSO achieved high transmission power $|S_{21}|^2$ = 0.998, 0.998, 0.999, 0.988, and 0.998 respectively. For broadband operation, we used the objective function as follow.

$$\text{Minimize } F = \frac{1}{3}\sum_{i=1}^{3}\left(1 - |S_{21}(f_i)|^2\right) \tag{5.17}$$

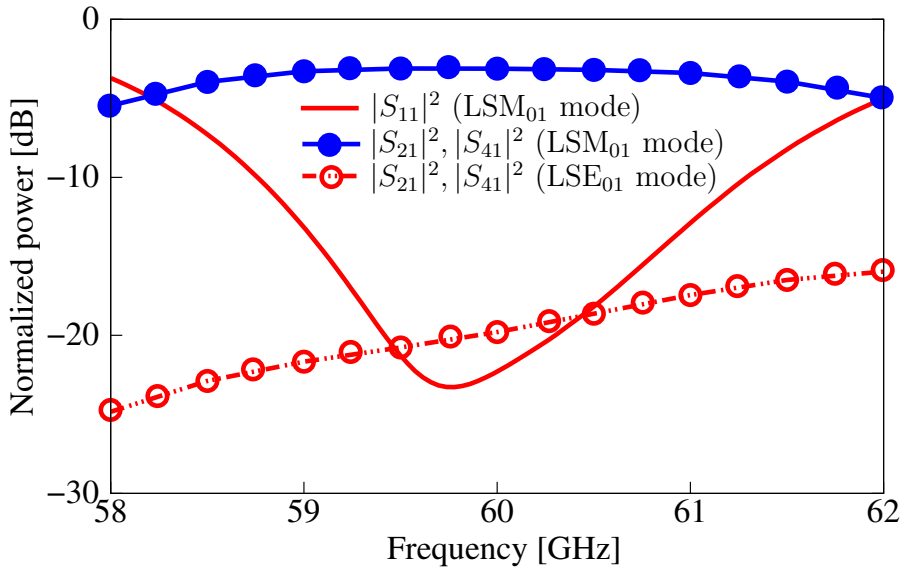

Figure 5.17: The frequency characteristics analysis of NRD T-branch waveguide at broadband operation using BDEA.

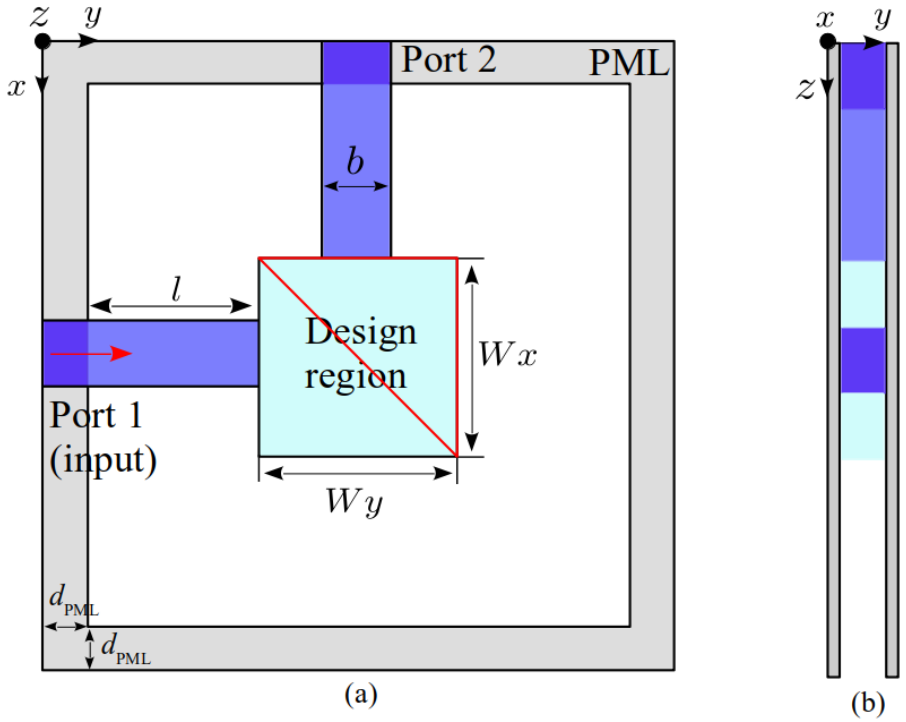

Figure 5.18: Initial structure of NRD bending waveguide (a) top view (b) front view.

$$(f_{1,2,3} = 59,\ 60,\ 61\ \text{GHz})$$

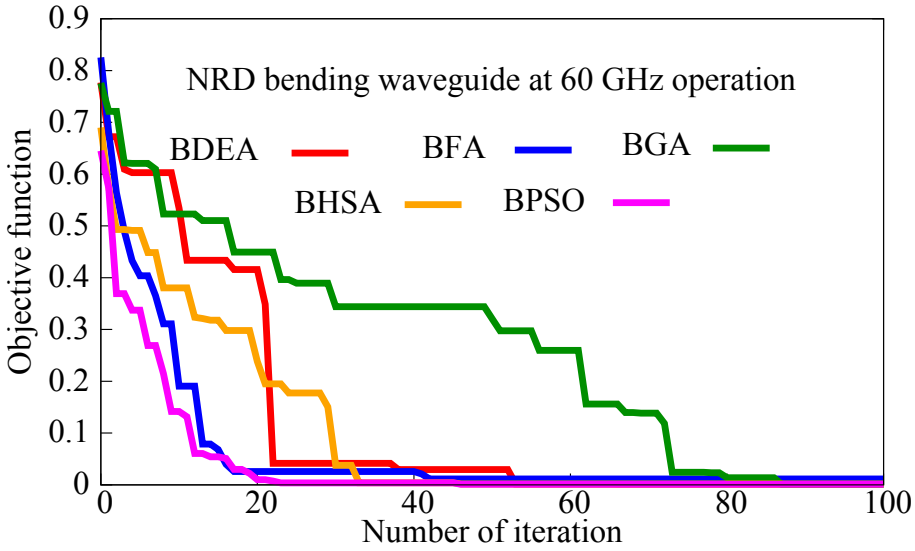

Figure 5.19: Convergence behavior of NRD bending waveguide at 60 GHz operation.

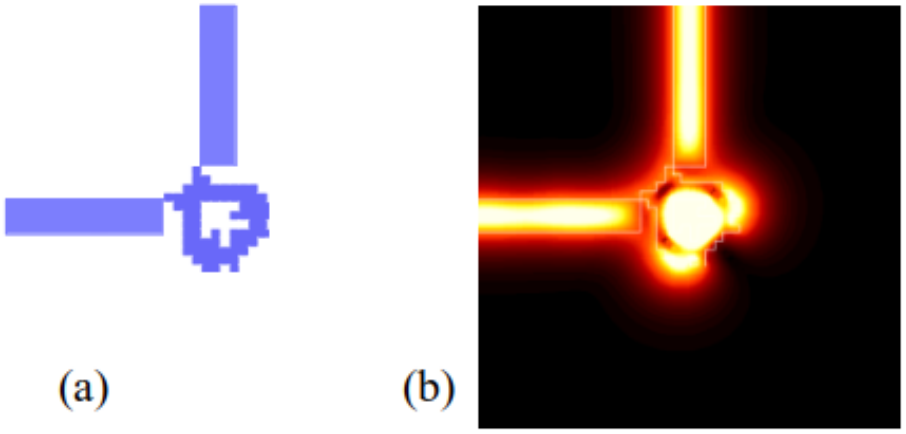

Figure 5.20: Optimal results of bending waveguide at 60 GHz using BHSA (a) optimized structure and (b) propagation field.

The above objective function analyzes the guide structure using three frequencies 59, 60, 61 GHz. Figure 5.23 depicts the convergence behavior of a bending waveguide at broadband operation, with almost same convergence order to that of the preceding example of a broadband T-branch, where BDEA and BHSA are more efficient than BGA. BDEA, BHSA, and BGA achieved broad bandwidth about 3 GHz in this design example, while BPSO and BFA achieved 2.3 GHz and 2 GHz respectively. The best optimal results at broadband operation using BDEA are shown in Fig. 5.24 and Fig. 5.25. Furthermore, the performance detail of proposed

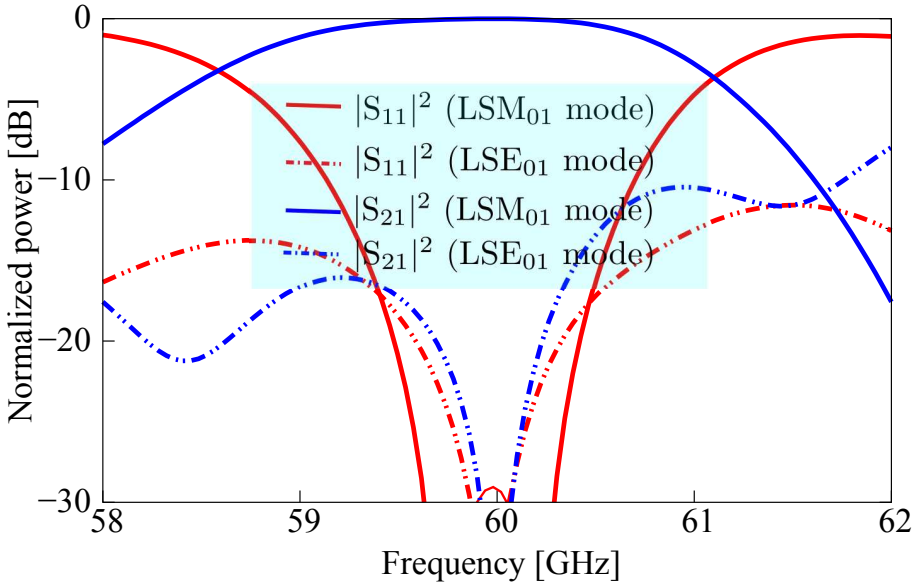

Figure 5.21: The frequency characteristics analysis of NRD bending using BHSA.

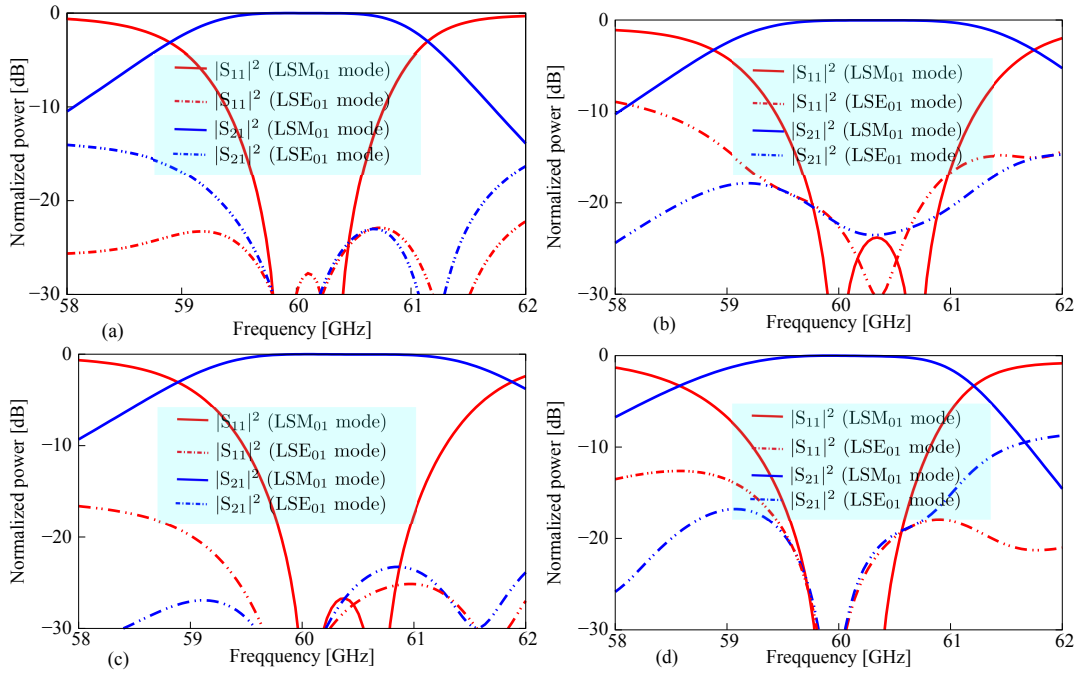

Figure 5.22: Frequency characteristics analysis of bending waveguide at 60 GHz operation (a) BDEA (b) BFA (c) BGA (d) BPSO.

NRD bending waveguide is summarized in Table 5.3.

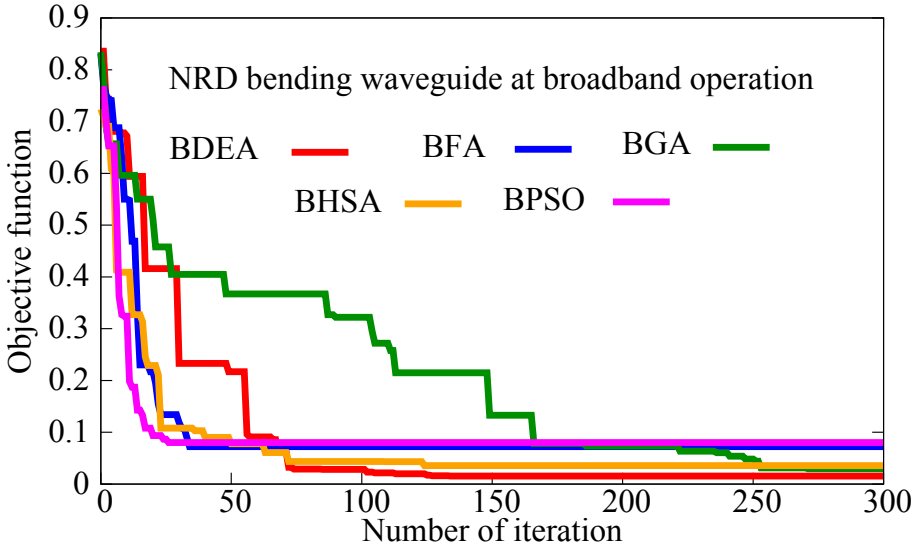

Figure 5.23: Convergence behavior of NRD Bending waveguide at broadband operation.

Table 5.3: Detail performance analysis of NRD bending waveguide at 60 GHz and broadband operation

Bending	**Transmission [dB]**		**Reflection [dB]**		**BW**
60 GHz	**LSM_{01}**	**LSE_{01}**	**LSM_{01}**	**LSE_{01}**	**[GHz]**
BGA	-0.003	-35.5	-34.7	-35.8	$--$
BPSO	-0.004	-34.9	-33.9	-35.0	$--$
BDEA	-0.006	-38.0	-29.8	-38.0	$--$
BHSA	-0.007	-39.4	-29.1	-34.6	$--$
BFA	-0.05	-22.6	-41.2	-22.3	$--$
Broadband	**Transmission [dB]**		**Reflection [dB]**		**BW**
Bending	**LSM_{01}**	**LSE_{01}**	**LSM_{01}**	**LSE_{01}**	**[GHz]**
BDEA	-0.006	-38.0	-29.8	-38.0	3.0
BGA	-0.17	-31.8	-14.0	-33.5	3.0
BHSA	-0.007	-39.4	-29.1	-34.6	3.0
BFA	-0.14	-31.2	-14.1	-31.3	2.3
BPSO	-0.08	-21.0	-22.5	-22.2	2.0

5.2.4 Frequency Demultiplexer

Finally, we consider another interesting example of NRD frequency demultiplexer whose initial structure, placement of output ports, and incident conditions are different from those in the prior examples as shown in Fig. 5.26. It has one input and two output ports, as well as a design region of size $6\ \text{mm} \times 16\ \text{mm}$ between them. The design region is divided into 12×32 pixels, with each of size is

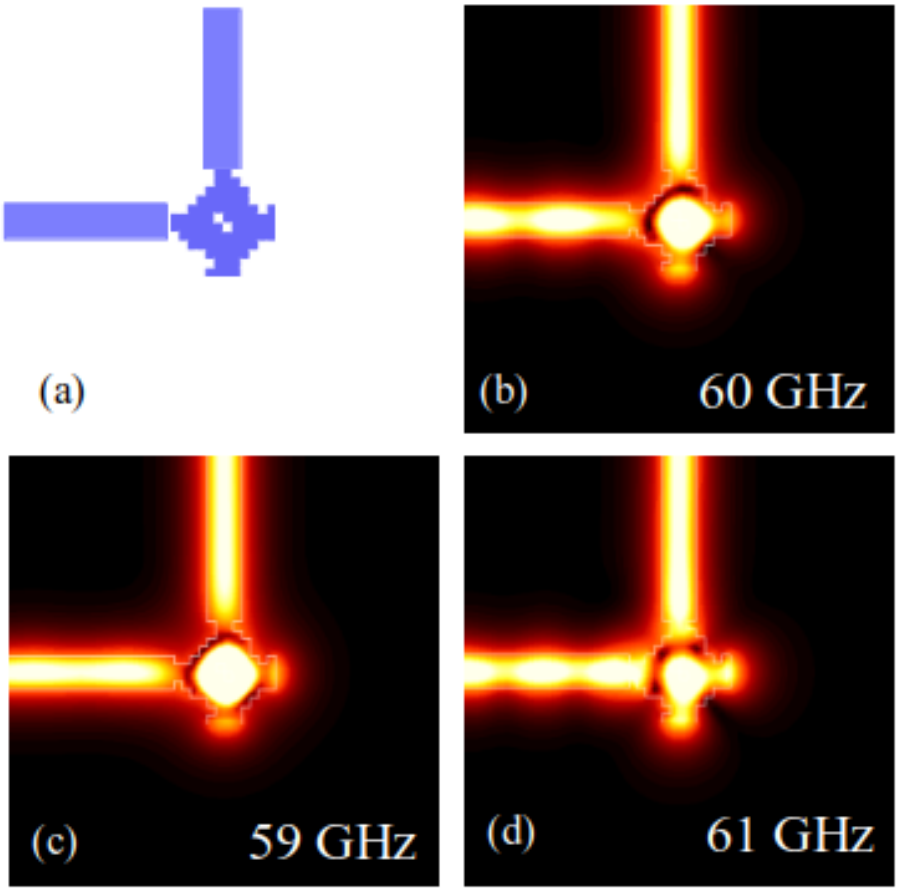

Figure 5.24: Optimal results of bending waveguide at broadband operation using BDEA (a) optimized structure and (b-d) propagation field.

$0.5\ \text{mm} \times 0.5\ \text{mm}$. The gap between two output waveguides is set to be d = 8 mm to avoid the coupling effect. To get the maximum power of a particular frequency at a desired output port, we ignore structural symmetry conditions in this case. Two frequencies $f_1 = 59$ GHz and $f_2 = 61$ GHz with LSM_{01} mode are incident at input port 1 and are separated into two different output ports. The following objective function is used to separate the input frequencies.

$$\text{Minimize } F = \frac{1}{2}[(1 - |S_{21}(f_1)|^2) + (1 - |S_{31}(f_2)|^2)] \tag{5.18}$$

$$(f_{1,2} = 59,\ 61\ \text{GHz})$$

where $|S_{21}|^2$ and $|S_{31}|^2$ are transmission powers at port 2 and port 3 for 59 GHz and 61 GHz respectively. After going through a design region optimized by using binary evolutionary approaches, two input frequencies are divided into two dif-

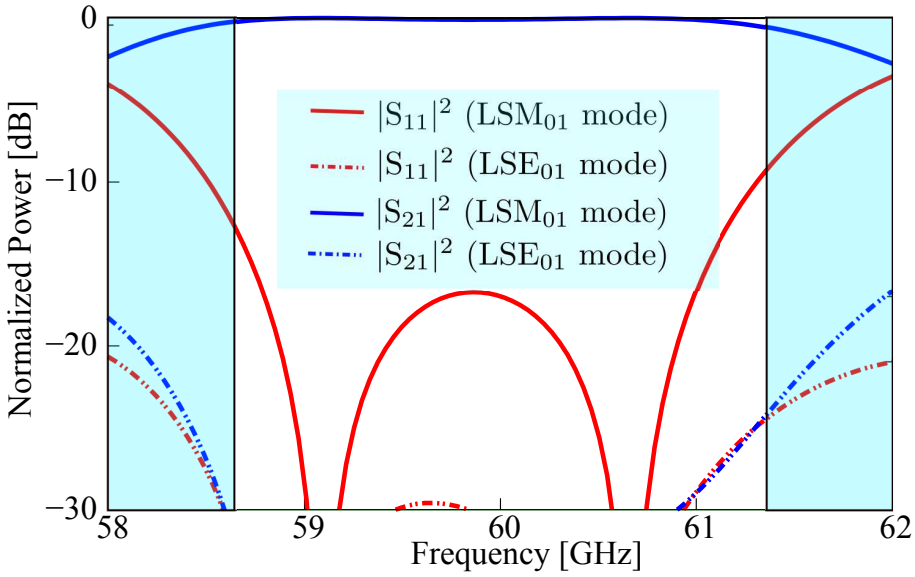

Figure 5.25: The frequency characteristics analysis of NRD bending waveguide at broadband operation using BDEA.

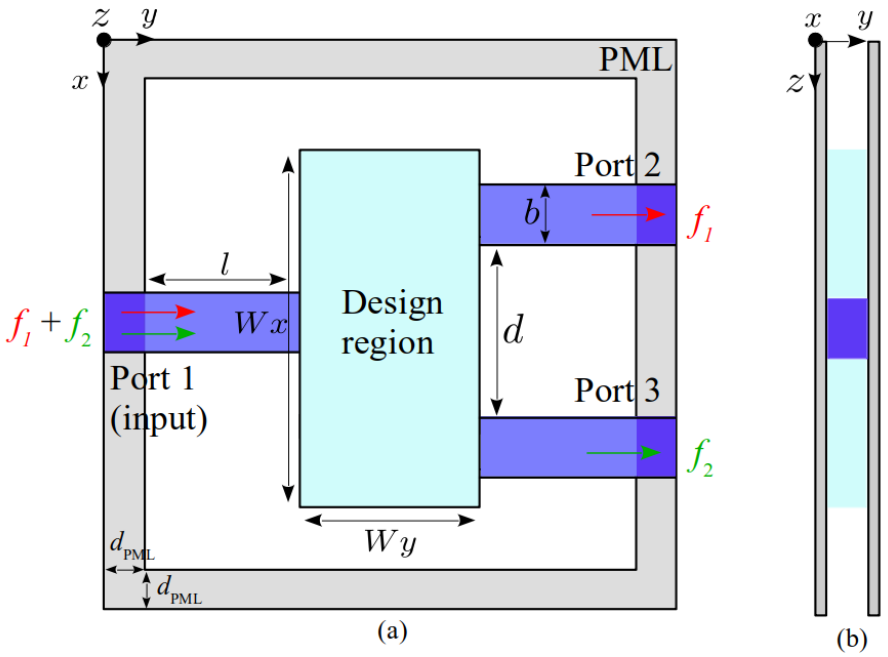

Figure 5.26: Initial structure of NRD frequency demultiplexer (a) top view (b) front view.

ferent output ports. The convergence trend of optimizations for designed device at 59 GHz and 61 GHz is shown in Fig. 5.27. In comparison to the preceding devices, more iterations are required for optimum convergence to obtain the desired

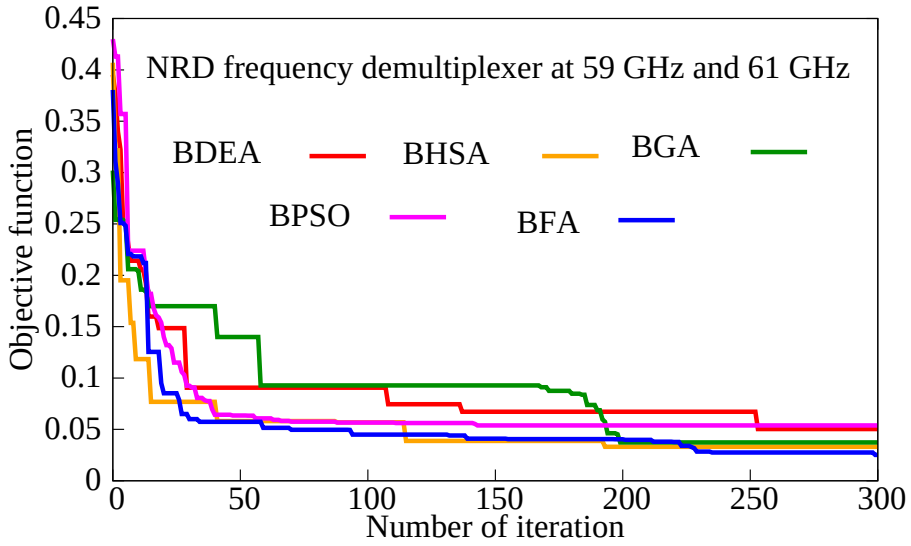

Figure 5.27: Convergence behavior of NRD frequency demultiplexer at broadband operation.

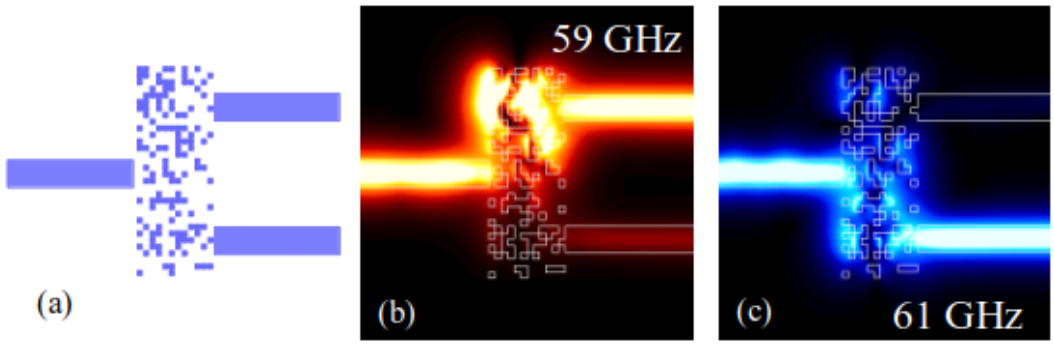

Figure 5.28: Optimal results of frequency demultiplexer using BFA (a) optimized structure and (b) propagation field at 59 GHz and 61 GHz respectively.

properties due to complicated device functionality, multiple frequencies, and large size of design region. As demonstrated in Fig. 5.27, all optimization algorithms have a good enough convergence rate of less than 300 iterations. Fig. 5.28 shows the best optimal results of the NRD frequency demultiplexer device using BFA. The frequency characteristics of the designed device is shown in Fig. 5.29, with maximum transmission power at 59 GHz and 61 GHz, as indicated by the straight magenta line. At 59 GHz and 61 GHz, the transmission power is 0.964 and 0.985 with minimal crosstalk level 0.03 and 0.006 respectively. Figure 5.28(b) and (c) indicate that the propagation fields of 59 GHz and 61 GHz are fully guided into output waveguides without any coupling effect. The main purpose of the demul-

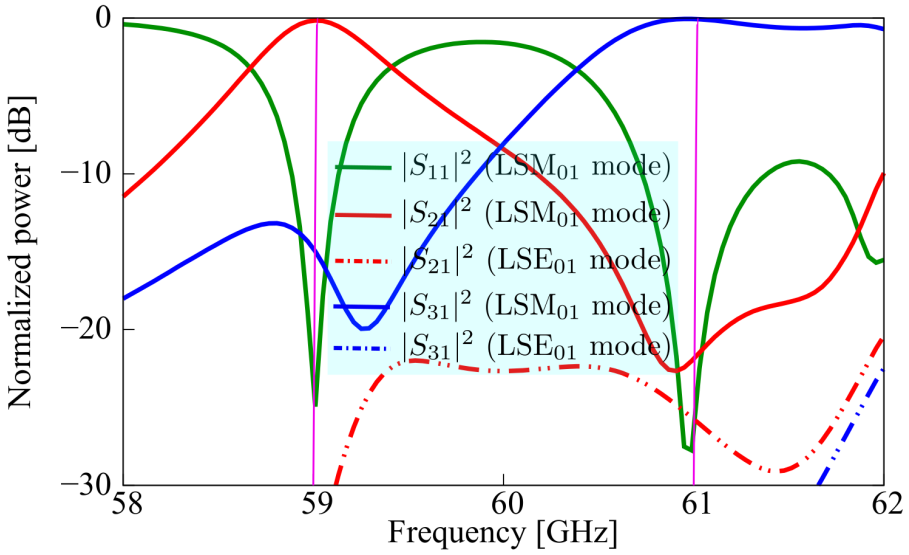

Figure 5.29: The frequency characteristics analysis of NRD frequency demultiplexer using BFA.

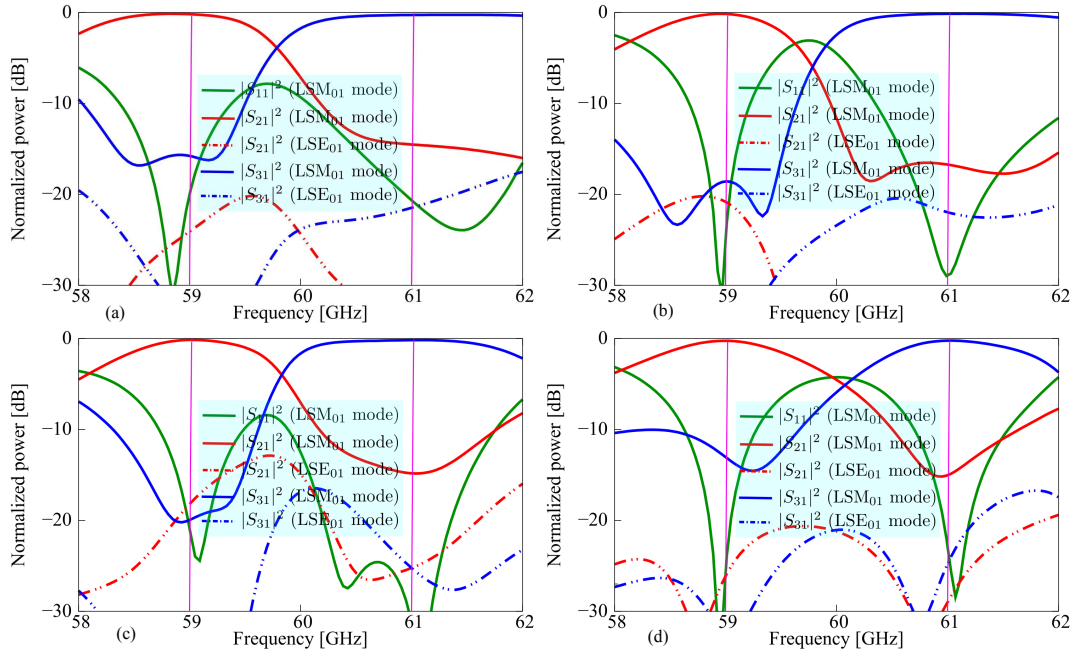

Figure 5.30: Frequency characteristics analysis of bending waveguide at 60 GHz operation (a) BDEA (b) BHSA (c) BGA (d) BPSO.

tiplexer is to achieve multi-path interference in the design region. For 59 GHz operation, constructive interference occurs at output port 2 and destructive interference occurs at output port 3, and vice versa for 61 GHz operation. Figure 5.30 shows the frequency characteristics analysis of designed device utilizing various

Table 5.4: Detail performance analysis of NRD frequency demultiplexer at 59 GHz and 61 GHz

Freq. Demux. 59 GHz	**Transmission [dB]**		**Reflection [dB]**		**X-talk [dB]**
	LSM_{01}	**LSE_{01}**	**LSM_{01}**	**LSE_{01}**	
BFA	-0.15	-37.3	-24.6	-31.9	-14.8
BHSA	-0.15	-20.8	-24.7	-19.6	-18.5
BGA	-0.15	-18.2	-20.8	-27.1	-19.9
BDEA	-0.32	-23.0	-15.1	-25.6	-14.4
BPSO	-0.24	-26.1	-25.4	-28.0	-13.0
Freq. Demux. 61 GHz	**Transmission [dB]**		**Reflection [dB]**		**X-talk [dB]**
	LSM_{01}	**LSE_{01}**	**LSM_{01}**	**LSE_{01}**	
BFA	-0.06	-42.2	-26.3	-24.7	-21.8
BHSA	-0.13	-21.9	-29.0	-26.2	-16.7
BGA	-0.17	-25.2	-31.2	-28.2	-14.8
BDEA	-0.38	-20.3	-16.4	-21.3	-13.3
BPSO	-0.23	-24.7	-22.8	-19.3	-15.0

optimization approaches, which similarly obtained the desired transmission property of more than 0.95. Furthermore, the performance detail of proposed NRD frequency demultiplexer is summarized in Table 5.4.

5.3 Pros and Cons of Evolutionary Approaches

The developed evolutionary approaches have a large degree of design freedom and require a small number of variables to efficiently optimize the pixel pattern in the design region. They result in high computation efficiency and converge the solution very quickly within a few iterations. This has been observed in proposed NRD guide devices. In addition, no matter how complex the device functionality and structure is or how large the design region is, developed evolutionary techniques are totally trustworthy for any type of NRD guide at single frequency operation. In spite of several practical advantages that are mentioned above, developed evolutionary approaches have some limitations too, the most important one being the careful selection of hyper parameters. Inappropriate parameter selection can result in population stagnation and premature convergence, rendering a solution unfeasible. Two of our five developed optimization approaches, BPSO and BFA, are not completely reliable in broadband operation, which is a only limitation. On the other hand, BDEA, BHSA, and BGA, are extremely efficient in both operations.

5.4 Stability Analysis of Developed Optimization Approaches

In order to investigate the stability performance of our developed evolutionary approaches, we considered the NRD T-branch power splitter which is the most challenging device for developed optimizations has been proven above. The device configuration, initialization and other hyper parameters of each optimization algorithm are same. The stability analysis is conducted by optimizing the considered device through ten attempts as shown in Fig. 5.31. We can see that BHSA and BDEA proves its high stability characteristics in each attempt but BHSA is more efficient than BDEA. The value of objective function in BGA is less than 0.2 with 100 iterations and may possible to achieve almost 0 with more iteration as obtained in BDEA and BHSA. The stability performance of BPSO and BFA is not impressive as achieved in rest of the optimizations. However, we can consider both of them for other simple NRD guide devices such as bending and crossing waveguide. Overall this analysis state that the BHSA is best one in term of stability, computational efficiency and reliability.

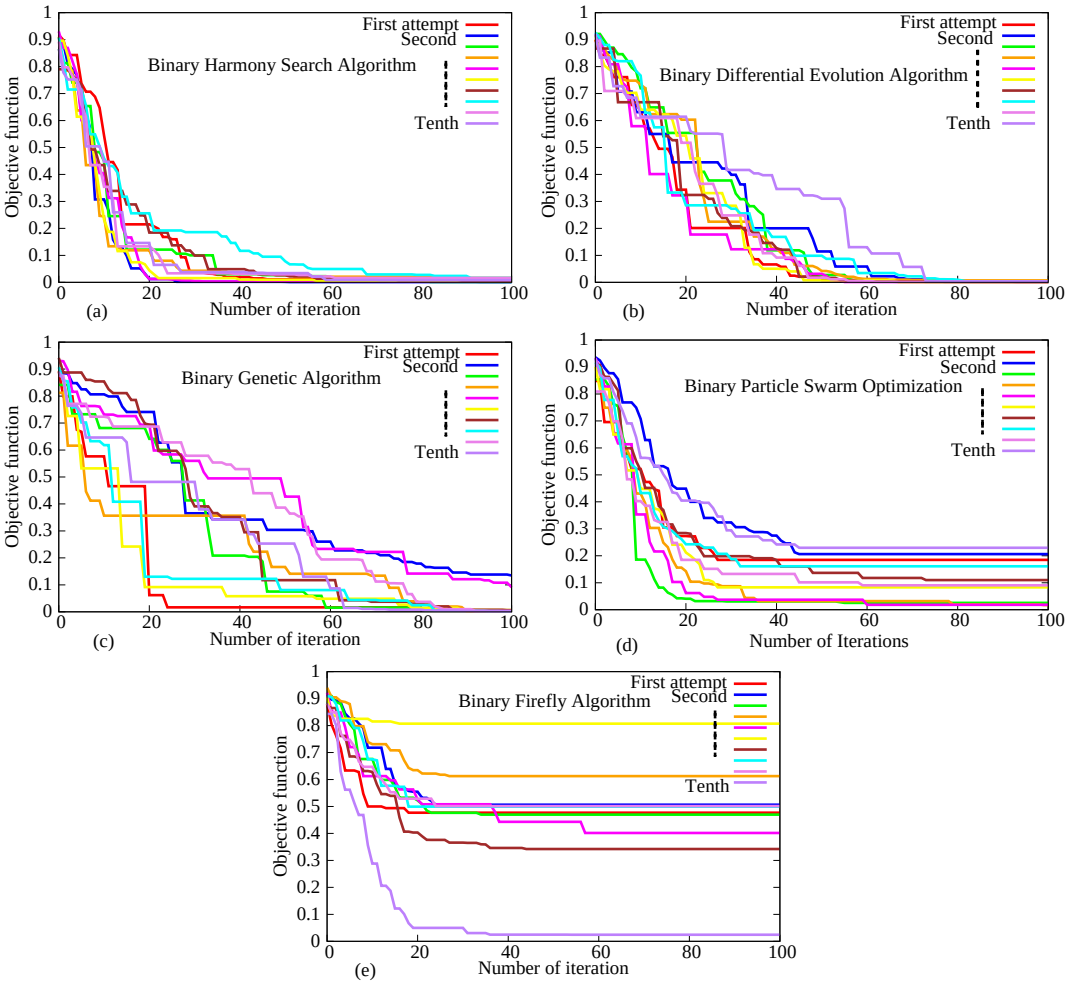

Figure 5.31: Stability analysis of developed evolutionary approaches (a) BHSA (b) BDEA (c) BGA (d) BPSO (e) BFA.

Chapter 6

Optimal Design of NRD Guide Using Magnetic Material

In the preceding chapters, we developed simulation and optimization methods for the analysis of NRD guides and several guide devices has been considered to show the usefulness of those methods. Now, in this chapter we extend our 2D-FV-FVEM using only dielectric material to dielectric and magnetic materials to realize the NRD non reciprocal guide devices. In order to verify the method, we considered NRD circulator and isolator at operating frequency of 26 GHz. The Ni-Zn ferrite material is used as a magnetic material in the center of the design region. In addition, the same devices are also designed at wideband operation to achieve the broadband property. To optimize the design region of considered devices binary harmony search and differential evolutionary algorithms are employ for single frequency or broadband operation respectively.

Although several types of non-reciprocal devices are proposed in the literature for various applications, with photonic crystal technology being the most well-known due to its great design flexibility and ability to control photonic motions [89]-[97]. But the optimal design of NRD-based non-reciprocal devices has yet to be thoroughly investigated. Non-reciprocal devices have received a lot of attention from researchers in recent years because they have a lot of interesting applications, such as directional controllers, power isolation between elements and modules, routing, data transmission, and as a duplexer in communication systems [98]-[104]. Generally most of circulators have three ports. As the number of ports increases, the usability of these devices improves. The protection of the source from destructive load reflections is one of the most significant functions of circulators. In

the microwave region, ferrite circulators give a high level of isolation and a broad frequency range. In circulators light entering from each input is directed toward the appropriate output after interacting with the magnetic material. The circulator allows waves to propagate in certain directions while preventing them from propagating in other undesirable directions, and it is a critical circuit component that realizes output at various ports when input is applied at the last output port.

On the other hands, millimeter-wave isolators are highly needed to isolate the power between elements and modules integrated in the circuit system applications. A circuit element known as an isolator permits forward propagation in one direction while preventing backward propagation and multi-path interference. Integration of isolators with other devices in the circuit is highly desired because they can improve the functionality and performance of communication systems and reduce the circuit size and cost too [105]. In last decades, research on optical and millimeter-wave isolators, leading to a wide variety of isolator designs, photonic crystal based isolators have been reported for miniaturization [106]-[109]. This chapter demonstrate the formulation of 2D-FV-FEM using magnetic materials, numerical design examples including NRD circulator and isolator and their simulation results.

6.1 2-D Full-Vectorial Finite Element Method for Magnetic Materials

The vector wave equation is used to describe the millimete-wave propagation in NRD guide using magnetic material and its functional relation are as follow:

$$\nabla \times \left([\varepsilon_r]^{-1} \nabla \times \boldsymbol{H} \right) - k_o^2 [\mu_r] \boldsymbol{H} = 0 \tag{6.1}$$

$$\begin{aligned} F = & \iiint \left[(\nabla \times \boldsymbol{H}^*) \cdot \left([\varepsilon_r]^{-1} \nabla \times \boldsymbol{H} \right) - k_0^2 \boldsymbol{H}^* \cdot [\mu_r] \boldsymbol{H} \right] dV \\ & - \iint \left\{ \boldsymbol{H}^* \cdot \left(\boldsymbol{i}_n \times [\varepsilon_r]^{-1} \nabla \times \boldsymbol{H} \right) \right\} dS. \end{aligned} \tag{6.2}$$

where $[\varepsilon_r]$ is the relative permittivity, $[\mu_r]$ is the relative permeability tensor, and k_0 is the free-space wavenumber. In the case that magnetic material is magnetized in z-direction normal to the metal parallel plates, the relative permittivity and

permeability tensors can be written as follow:

$$[\varepsilon_r] = \begin{bmatrix} \varepsilon_{xx} & 0 & 0 \\ 0 & \varepsilon_{yy} & 0 \\ 0 & 0 & \varepsilon_{zz} \end{bmatrix}, \; [\mu_r] = \begin{bmatrix} \mu_{xx} & \mu_{xy} & 0 \\ \mu_{yx} & \mu_{yy} & 0 \\ 0 & 0 & \mu_{zz} \end{bmatrix} \tag{6.3}$$

Due to uniform structure of the device in the z-direction the electric and magnetic fields, in LSM_{n1} and LSE_{n1} modes (n = 0, 1, . .) can be expressed as follows:

$$\begin{aligned} E_x &= \phi_x(x,y)\sin\left(\frac{\pi}{a}z\right), \quad H_x = \psi_x(x,y)\cos\left(\frac{\pi}{a}z\right), \\ E_y &= \phi_y(x,y)\sin\left(\frac{\pi}{a}z\right), \quad H_y = \psi_y(x,y)\cos\left(\frac{\pi}{a}z\right), \\ E_z &= \phi_z(x,y)\cos\left(\frac{\pi}{a}z\right), \quad H_z = \psi_z(x,y)\sin\left(\frac{\pi}{a}z\right). \end{aligned}$$

By descritizing the computational domain into curvilinear hybrid edge/nodal element, the following expression is derived for the analysis of NRD guide.

$$\begin{aligned} \boldsymbol{\psi}(x,y) &= \left(\boldsymbol{i}_x\{U\}^T + \boldsymbol{i}_y\{V\}^T\right)\{\psi_t\} + \boldsymbol{i}_z\{N\}^T\{\psi_z\} \\ &= \{\boldsymbol{N}\}^T\{\psi\} \end{aligned} \tag{6.4}$$

where $\{U\}$ and $\{V\}$ are the edge element shape function and $\{N\}$ is the nodal element shape function. The following linear equation is obtained by applying the variational principle.

$$\left([K] - k_0^2\,[M]\right)\{\psi\} = \{u\} \tag{6.5}$$

$$[K] = \begin{bmatrix} [K_{tt}] & [K_{tz}] \\ [K_{zt}] & [K_{zz}] \end{bmatrix}, \quad [M] = \begin{bmatrix} [M_{tt}] & [0] \\ [0] & [M_{zz}] \end{bmatrix},$$
$$\{\psi\} = \begin{bmatrix} \{\psi_t\} \\ \{\psi_z\} \end{bmatrix}, \quad \{u\} = \begin{bmatrix} \{u_t\} \\ \{u_z\} \end{bmatrix}$$

where $[K]$ and $[M]$ are finite element matrices and $\{u\}$ is the incident condition. The sub-matrices of $[K]$ and $[M]$ are as follow:

$$[K_{tt}] = \sum_e \iint_e \left[\left(\frac{1}{\varepsilon_{xx}} \{V\}\{V\}^T + \frac{1}{\varepsilon_{yy}} \{U\}\{U\}^T \right) \left(\frac{\pi}{a} \right)^2 \right. \tag{6.6}$$

$$\left. + \frac{1}{\varepsilon_{zz}} \left(\frac{\partial \{V\}}{\partial x} - \frac{\partial \{U\}}{\partial y} \right) \left(\frac{\partial \{V\}^T}{\partial x} - \frac{\partial \{U\}^T}{\partial y} \right) \right] dxdy \tag{6.7}$$

$$[K_{tz}] = \sum_e \iint_e \left[\left(\frac{1}{\varepsilon_{xx}} \{V\} \frac{\partial \{N\}^T}{\partial y} + \frac{1}{\varepsilon_{yy}} \{U\} \frac{\partial \{N\}^T}{\partial x} \right) \left(\frac{\pi}{a} \right) \right] \times dxdy \tag{6.8}$$

$$[K_{zt}] = \sum_e \iint_e \left[\left(\frac{1}{\varepsilon_{xx}} \frac{\partial \{N\}}{\partial y} \{V\}^T + \frac{1}{\varepsilon_{yy}} \frac{\partial \{N\}}{\partial y} \{U\}^T \right) \left(\frac{\pi}{a} \right) \right] \times dxdy \tag{6.9}$$

$$[K_{zz}] = \sum_e \iint_e \left[\left(\frac{1}{\varepsilon_{yy}} \frac{\partial \{N\}}{\partial x} \frac{\partial \{N\}^T}{\partial x} + \frac{1}{\varepsilon_{xx}} \frac{\partial \{N\}}{\partial y} \frac{\partial \{N\}^T}{\partial y} \right) \right] \times dxdy \tag{6.10}$$

$$[M_{tt}] = \sum_e \iint_e \Big[\mu_{xx} \{U\}\{U\}^T + \mu_{yy} \{V\}\{V\}^T + \mu_{xy} \{U\}\{V\}^T + \tag{6.11}$$

$$\mu_{yx} \{V\}\{U\}^T \Big] dxdy \tag{6.12}$$

$$[M_{zz}] = \sum_e \iint_e \mu_{zz} \{N\}\{N\}^T dxdy \tag{6.13}$$

$$\{u\} = \int \int_\Gamma \left[\{N\}^* . \left\{ i_n \times \left([\varepsilon_r]^{-1} \nabla \times \boldsymbol{H} \right) \right\} \right] ds \tag{6.14}$$

The expression of Perfectly Matched Layer (PML), modal amplitude, and propagation constant of propagating modes are derived in chapter 3.

6.2 Numerical Examples

In this chapter, we present two-dimensional full vectorial finite element method for non-reciprocal guide devices. To confirm the validity of developed method we considered two NRD guide devices which include NRD four port cross shaped circulator and three port isolator. The Ni-Zn ferrite material is used in the center of the design region whose properties are as follow:

$$\varepsilon_{rb} = 13.5 \tag{6.15}$$

$$[\mu_{rb}] = \begin{bmatrix} \mu & j\kappa & 0 \\ -j\kappa & \mu & 0 \\ 0 & 0 & 1 \end{bmatrix} \tag{6.16}$$

$$\mu = 1 + \frac{\omega_m(\omega_0 + j\alpha\omega)}{(\omega_0 + j\alpha\omega)^2 - \omega^2} \tag{6.17}$$

$$\kappa = \frac{\omega_m\omega}{(\omega_0 + j\alpha\omega)^2 - \omega^2} \tag{6.18}$$

where $\omega_0 = \mu_0\gamma H_0$, $\omega_m = \mu_0\gamma M_s$, $\gamma = 1.759 \times 10^{11}$ C/kg, $\alpha = 3 \times 10^{-5}$, $M_s = 2.39 \times 10^5$ A/m, $H_0 = 3.15 \times 10^5$ A/m then μ and κ are calculated as $\mu = 0.8315693 - j1.704673 \times 10^{-5}$, $\kappa = -0.3951738 - j1.234924 \times 10^{-5}$ at 26 GHz. For simplicity, the imaginary part of μ and κ is ignored in this design example.The LSM_{01} mode is incident at input port 1. The geometrical parameter, dispersion relation and simulation result are discussed below.

6.2.1 NRD Circulator

First, we present NRD four port cross shaped circulator whose initial structure shown in Fig. 6.1. The NRD circulator is made up of four waveguides that are connected to the design region, which is filled with ferrite material (green) centrally and magnetized by applying a magnetic field perpendicular to the metal parallel plates. The dielectric waveguides height, width, and length are indicated by a, b, and l respectively. The dispersion property of the NRD guide can be calculated using the relative permittivity of the dielectric waveguide ε_{ra} and the geometrical parameters a and b, as illustrated in Fig. 6.2. The 90 degree rotational structural symmetrical conditions are imposed in the design region indicated by the yellow lines as shown in Fig. 6.1 and one quarter of the design region is optimized. In

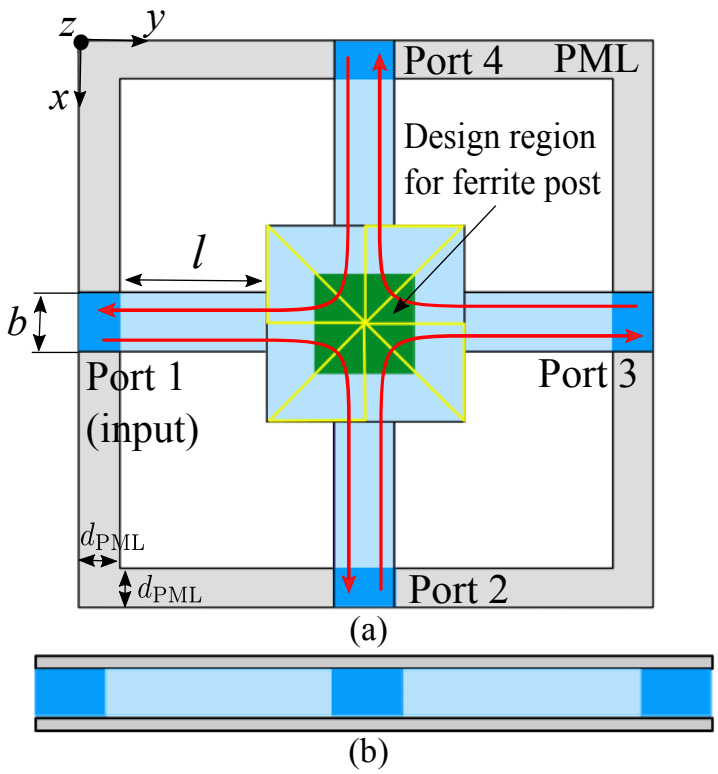

Figure 6.1: The design setup of the NRD based four port cross-shaped circulator at 26 GHz (a) top view (b) side view.

order to achieve the desired properties ferrite post geometry in $W_x \times W_y$ region is optimized then, dielectric distribution is optimized by using binary harmony search algorithm. The detailed geometrical parameters of the proposed device are shown in Table 6.1 and the design strategy is illustrated in Fig. 6.3. In this design example, using 90 degree rotational symmetry condition for four port devices, the following scattering matrix has to be as following form:

$$\begin{bmatrix} R & X_o & X_t & T \\ T & R & X_o & X_t \\ X_t & T & R & X_o \\ X_o & X_t & T & R \end{bmatrix} \tag{6.19}$$

Therfore if port 1 to port 2 transmission is achieved the circulator operation $(1 \rightarrow 2,\ 2 \rightarrow 3,\ 3 \rightarrow 4,\ 4 \rightarrow 1)$ are simultaneously achieved. In this case, it is sufficient to consider only the port 1 incidence case and the objective function to be minimized

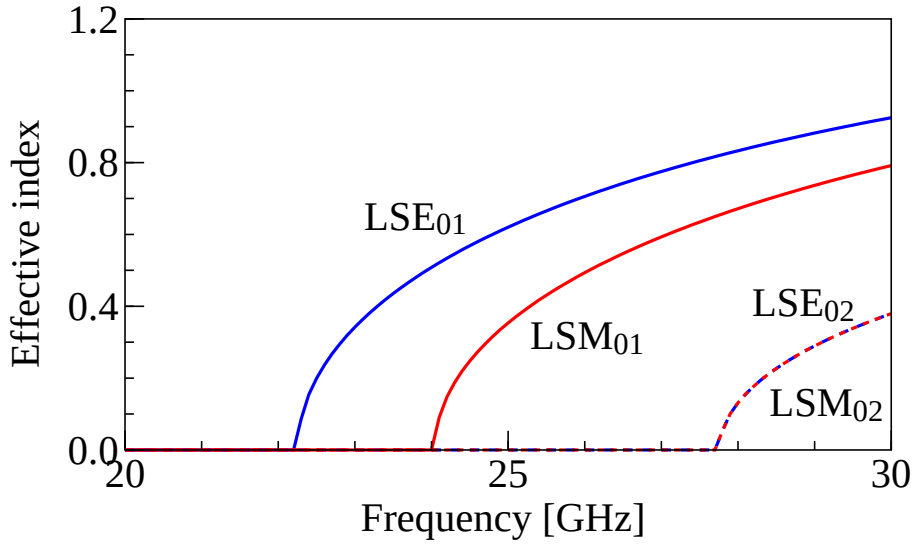

Figure 6.2: Dispersion relation at $a = 5.4$ mm, $b = 4$ mm, and $\varepsilon_r = 2.2$.

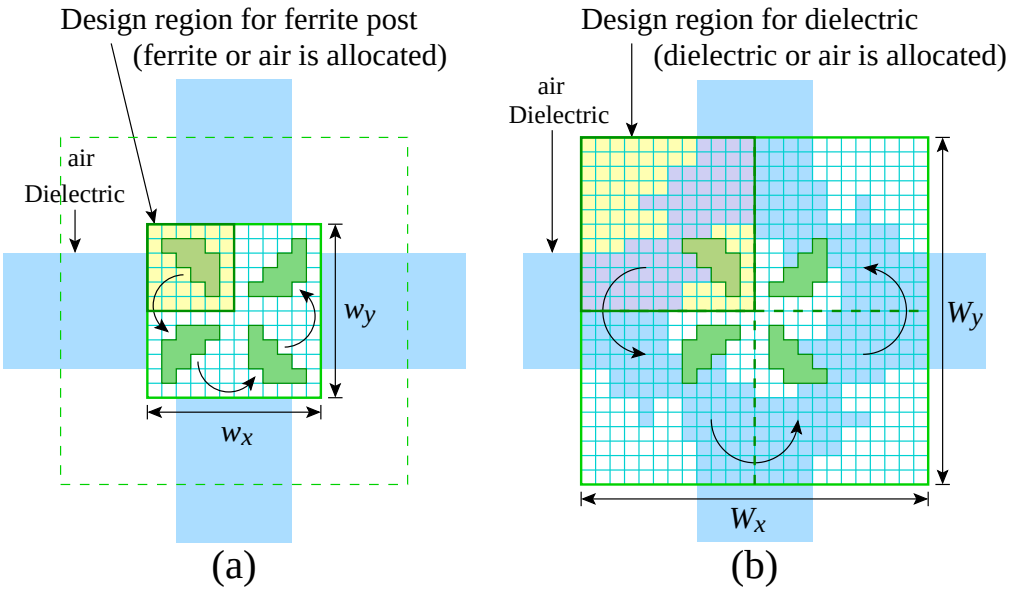

Figure 6.3: Two-step optimization of circulator (a) First step for optimization of ferrite post (b) Second step for optimization of dielectric, where ferrite post is fixed 90^0 rotational symmetry is imposed in both optimizations .

can be simply defined as follow:

$$\text{Minimize } C = 1 - |S_{21}|^2 \quad (\text{at } 26 \text{ GHz}) \tag{6.20}$$

Fig. 6.4 shows the optimal structure obtained by BHSA. Ferrite post are depicted in green, dielectric is in light blue, and air is in white. The structure in upper-left

Table 6.1: Geometrical parameters of NRD cross circulator.

Parameters	Description	Values
a	Height of dielectric strip	5.4 mm
b	Width of dielectric strip	4.0 mm
l	Length of dielectrip strip	20.0 mm
$W_x = W_y$	Size of total design region	12 mm
$w_x = w_y$	Size of ferrite post design region	6 mm
d_{PML}	Thickness of PML	10 mm
ε_{ra}	Permittivity of dielectric	2.2
ε_{rb}	Permittivity of ferrite	13.5
ε_{air}	Permittivity of air	1.0
$N_x = N_y$	Number of pixels	576
$\Delta_x = \Delta_y$	Size of pixel	0.5 mm
f	Operating frequency	26 GHz

quarter region is rotated and copied to the other region. According to the design region dimensions the total number of pixels are 576, with 144 ferrite and air in the center and the remaining dielectric and air around ferrite pixels. When port 1 is activated in LSM_{01} mode at 26 GHz, the propagation field is shown in Fig. 6.5. The wave propagates from port 1 to port 2, with 1 to 2, 2 to 3, 3 to 4, and 4 to 1 as the circulation direction are also shown in Fig. 6.5. By changing the direction of the applied external magnetic field, the propagation direction can be reversed. Figure 6.6 shows the normalized transmission power at various frequencies when port 1 is input and port 2 is output. The S-parameters of the design example are shown in Fig. 6.5 when any or all of the ports are input ports. Maximum transmission to target port is about -0.3 dB and maximum crosstalk in LSM_{01} mode is -17.7 dB (for opposite rotation) at 26 GHz. In order to achieve the broader bandwidth, we used the following modified objective function.

$$\text{Minimize } C = \frac{1}{4}\sum_{i=1}^{4} (1 - |S_{21}(f_i)|^2) \tag{6.21}$$

$$(f_{1,2,3,4} = 25.75,\ 26,\ 26.25,\ 26.5 \text{ GHz})$$

Due to complex device structure, functionality, several materials, and multiple frequencies in the objective function, it is quiet challenging for optimal design approach to optimize the pixels distribution efficiently with desired property. Therefore, the performance of NRD circulator at broadband operation is not impressive as we obtained in other devices in chapter 5. Fig. 6.7 shows the optimal structure of

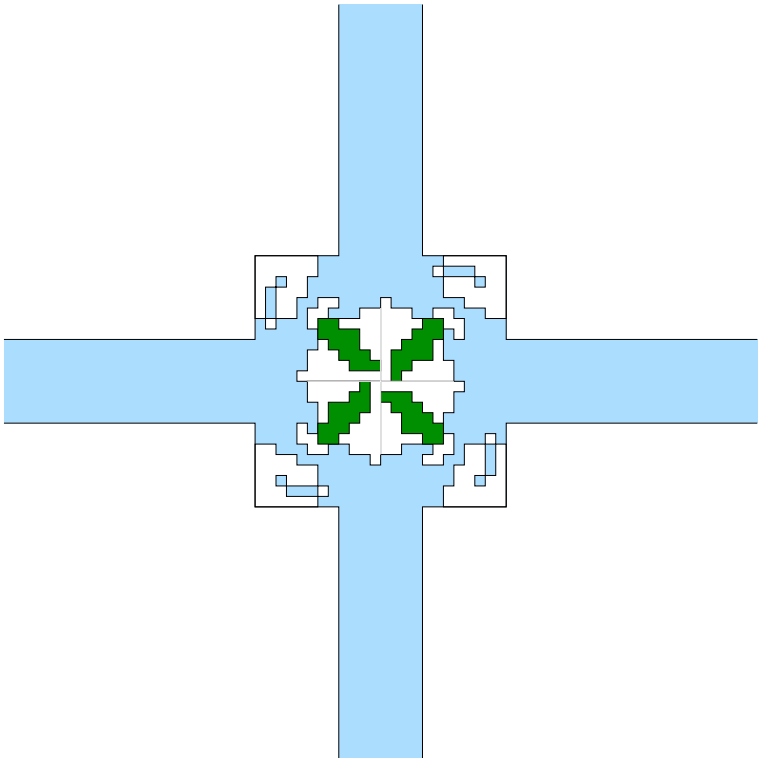

Figure 6.4: Optimal structure of NRD circulator.

NRD circulator using binary differential evolution algorithm at broadband operation. Figure 6.8 shows the propagation fields at different frequencies considered in the objective function. The designed device achieved bandwidth around 1.5 GHz in the range of 25.5 GHz to 27 GHz as shown in Fig. 6.9.

6.2.2 NRD Isolator

The design setup of proposed NRD isolator with three ports is shown in Fig. 6.10. In this design, we assume the separation between plates is $a = 4.5$ mm. The designed device is made up of three alumina (Al_2O_3) waveguide strips with a length and width of each is $l = 10$ mm and $b = 2$ mm, respectively. The gap between two waveguide strips is set to be $d = 4$ mm to avoid the coupling effect. The total size of design region is $W_x \times W_y = 10$ mm $\times$ 8 mm including ferrite post of thickness 1 mm which is inserted in the mid of design region (green). The total number of pixels in the design region are 288 excluding ferrite post region. The footprint of each pixel is 0.5 mm $\times$ 0.5 mm. The operating wavelength and guide width are taken into account while determining the pixel size to make the fabrication practical. Alumina

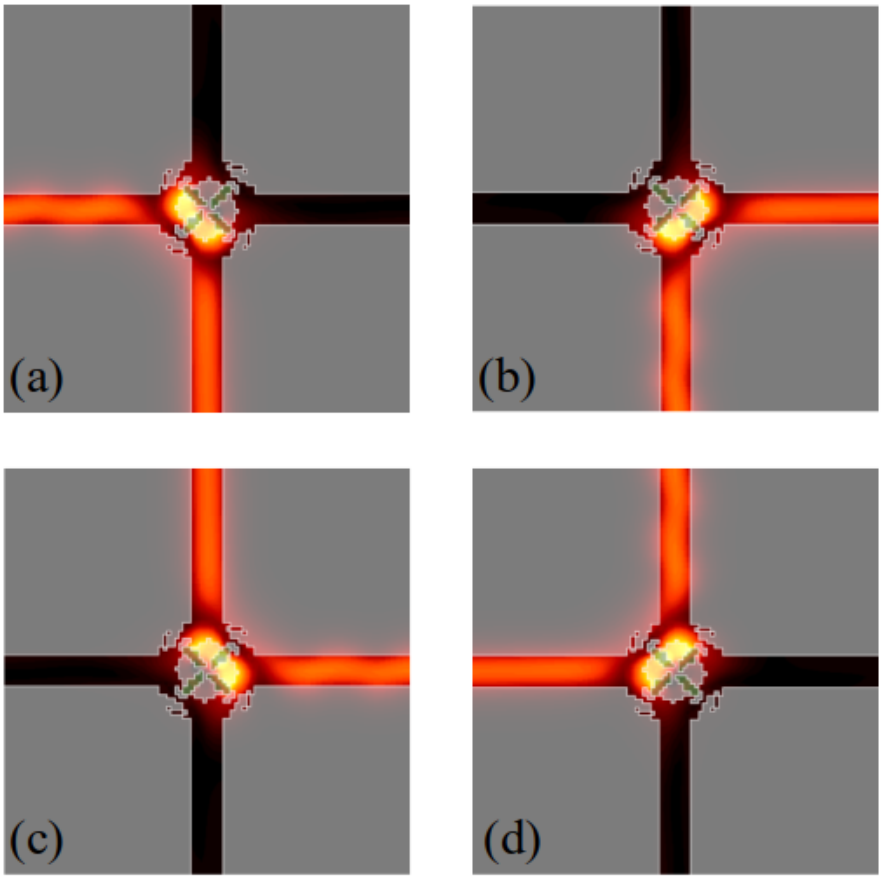

Figure 6.5: Propagating field of NRD circulator at 26 GHz when (a) port 1 is input (b) port 2 (c) port 3 (d) port 4.

(ε_{ra}), ferrite (ε_{rb}), and air (ε_{air}) all have relative permittivity values of 9.2, 13.5, and 1.0 respectively. The dispersion property of the input and output NRD guides can be calculated using the relative permittivity of the dielectric waveguide (ε_{ra}) and the geometrical parameters a, b as illustrated in Fig. 6.11. The computational domain is surrounded by a perfectly matched layer (PML) with a thickness of d_{PML} = 5 mm. Furthermore, LSM_{01} mode around 26 GHz is considered for excitation at input port. In order to maximize the power at port 2 and 3, the following objective function are used.

$$\text{Minimize } \boldsymbol{C} = (1 - |S_{21}|^2 + |S_{31}|^2 + |S_{11}|^2) \quad (\text{at 26 GHz}) \tag{6.22}$$

$$\text{Minimize } \boldsymbol{C} = (1 - |S_{32}|^2 + |S_{22}|^2 + |S_{12}|^2) \quad (\text{at 26 GHz}) \tag{6.23}$$

The optimal structure of the proposed device obtained by BHSA is shown in Fig.

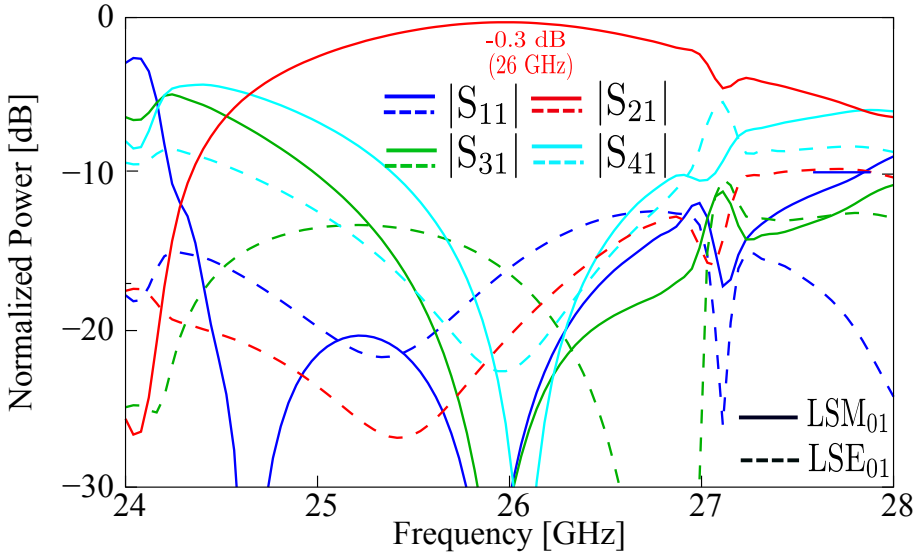

Figure 6.6: Frequency characteristics of NRD circulator.

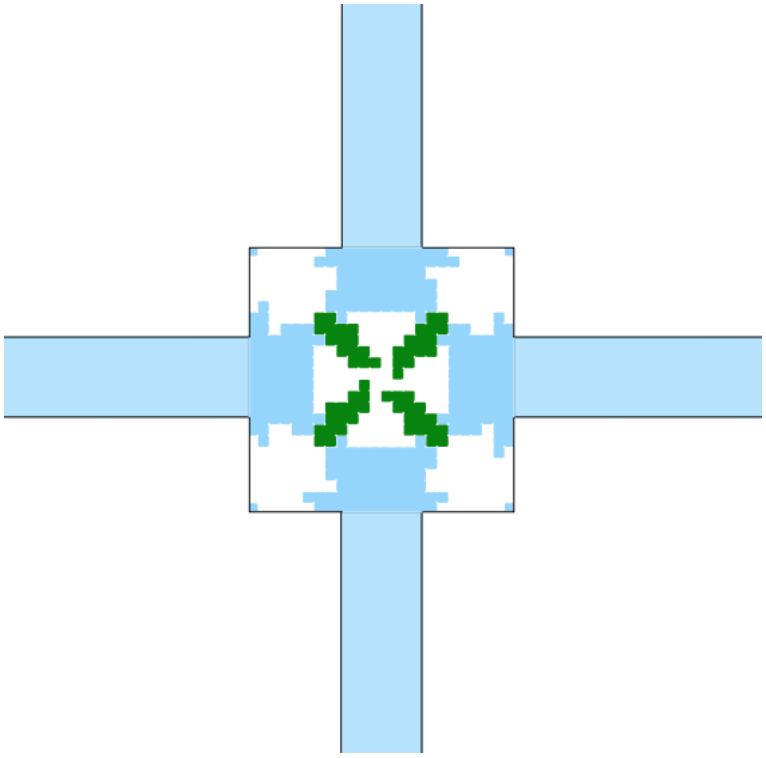

Figure 6.7: Optimal structure of NRD brodband circulator.

6.12. The propagation field is shown in Fig. 6.13. As shown in Fig. 6.13(a), the propagation field smoothly propagates from input port 1 toward output port 2. When the LSM_{01} wave at 26 GHz is launched at port 2, port 1 is completely

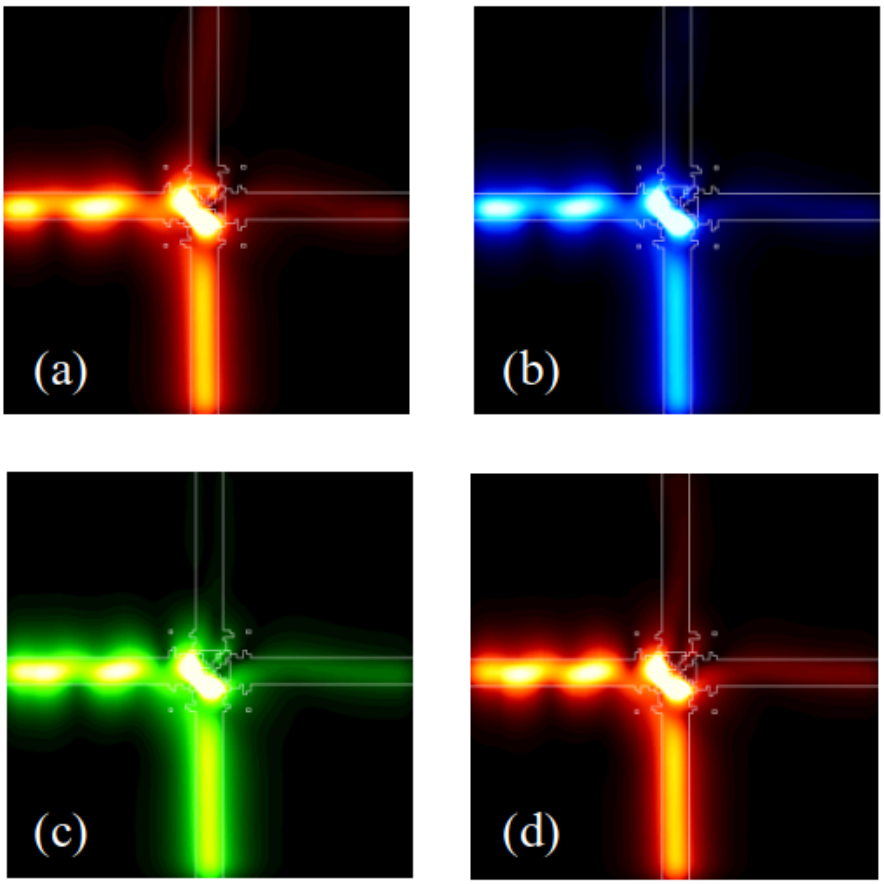

Figure 6.8: Propagating field of NRD broadband circulator at different frequencies (a) 25.75 GHz (b) 26 GHz (c) 26.25 GHz (d) 26.5 GHz.

isolated due to ferromagnetic resonance, as shown in Fig. 6.13(b). Our proposed device fully realizes the primary function of an isolator. Fig. 6.14 shows the frequency characteristics in the frequency range of 24 GHz-28 GHz. The proposed device achieved excellent forward transmission and backward rejection of -0.18 dB and -23 dB respectively. The S-parameters plays important role to understand the performance of device. In our design example S_{11} and S_{22} are forward and backward reflected powers while S_{21} and S_{12} represent the forward and backward transmission when port 1 and port 2 is input respectively. When ports 1 and 2 are input, the parameters S_{32} and S_{31} represent the transmission power at port 3. In order to achieve the broader bandwidth, we used the following modified objective function when port 1 and 2 is input respectively.

$$\text{Minimize } C = (1 - |S_{21}|^2 + |S_{31}|^2 + |S_{11}|^2) \tag{6.24}$$

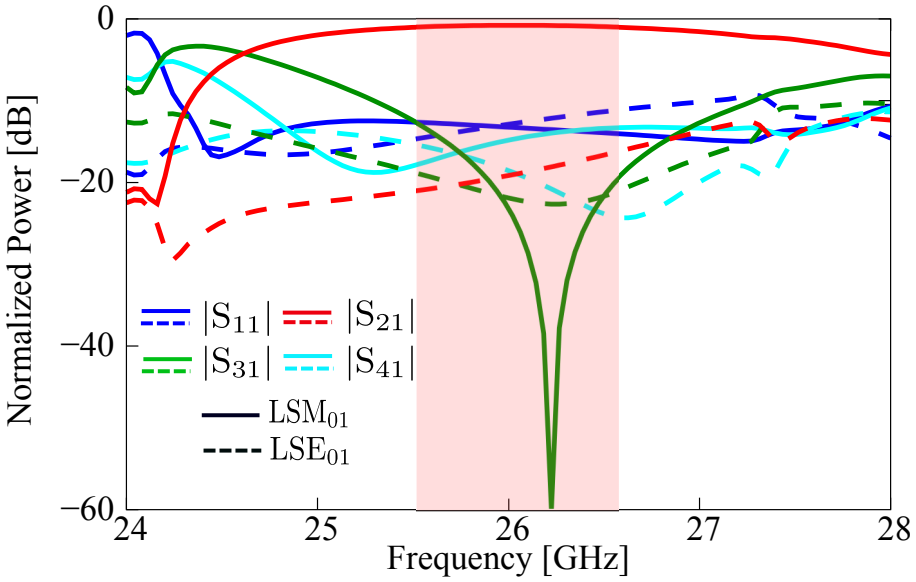

Figure 6.9: Frequency characteristics of NRD broadband circulator.

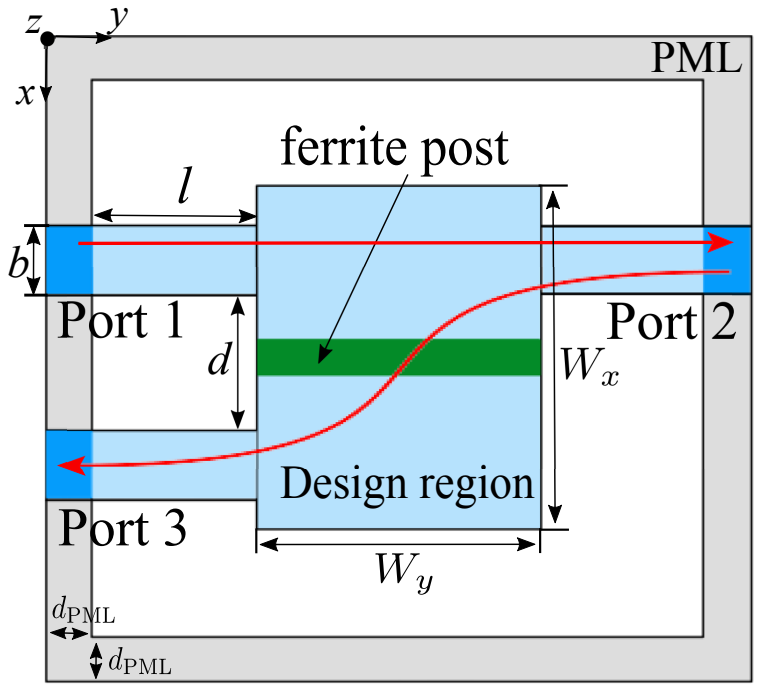

Figure 6.10: The design setup of the NRD three-port isolator at 26 GHz.

$$\text{Minimize } C = (1 - |S_{32}|^2 + |S_{22}|^2 + |S_{12}|^2) \tag{6.25}$$

$$(f_{1,2,3} = 25,\ 26,\ 27 \text{ GHz})$$

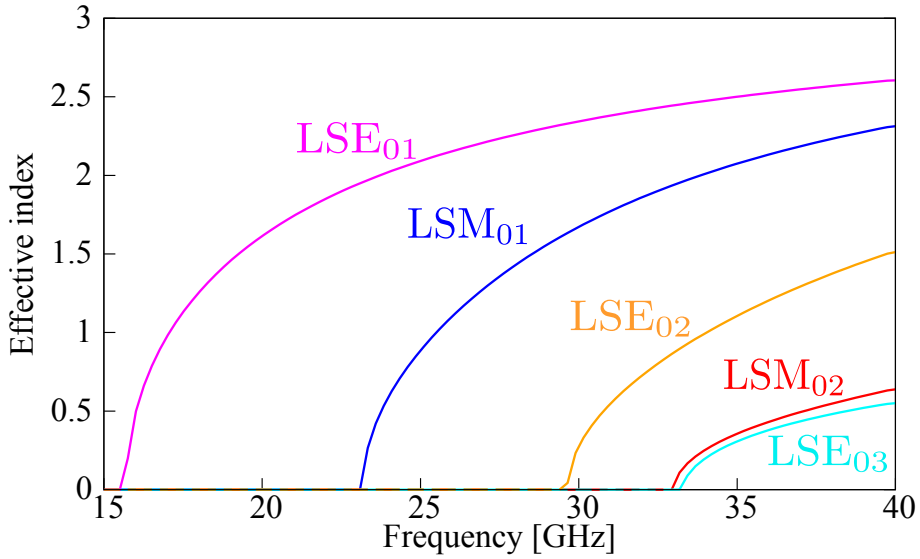

Figure 6.11: Dispersion relation at $a = 4.5$ mm, $b = 2.0$ mm, and $\varepsilon_r = 9.2$.

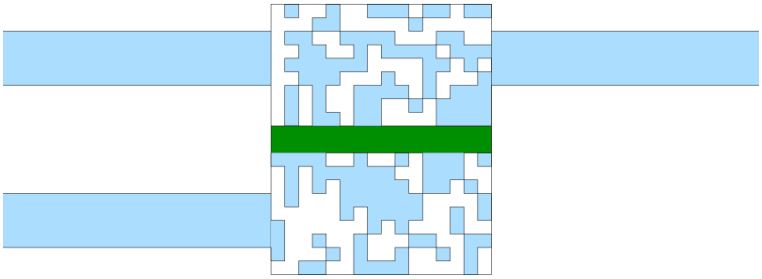

Figure 6.12: Optimal structure of NRD isolator.

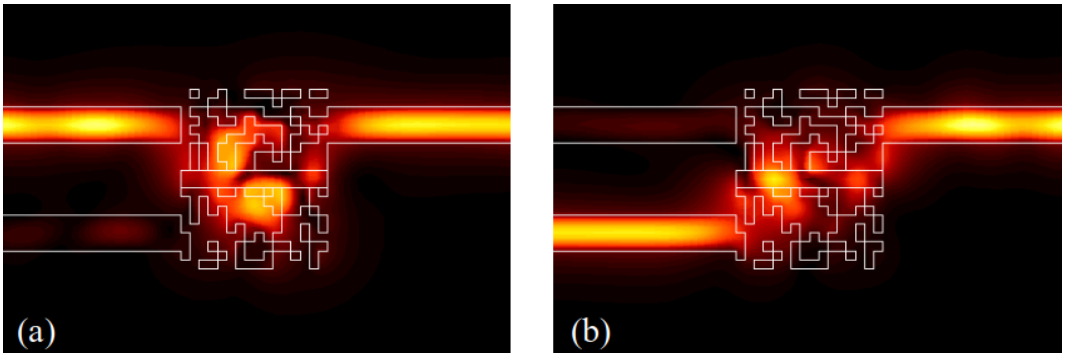

Figure 6.13: The propagating field in the NRD isolator at 26 GHz (a) transmission at port 2 when port 1 is input (b) transmission at port 3 when port 2 is input.

Fig. 6.15 shows the optimal structure of NRD isolator using binary differential evolution algorithm at broadband operation. Fig. 6.16 shows the propagation fields

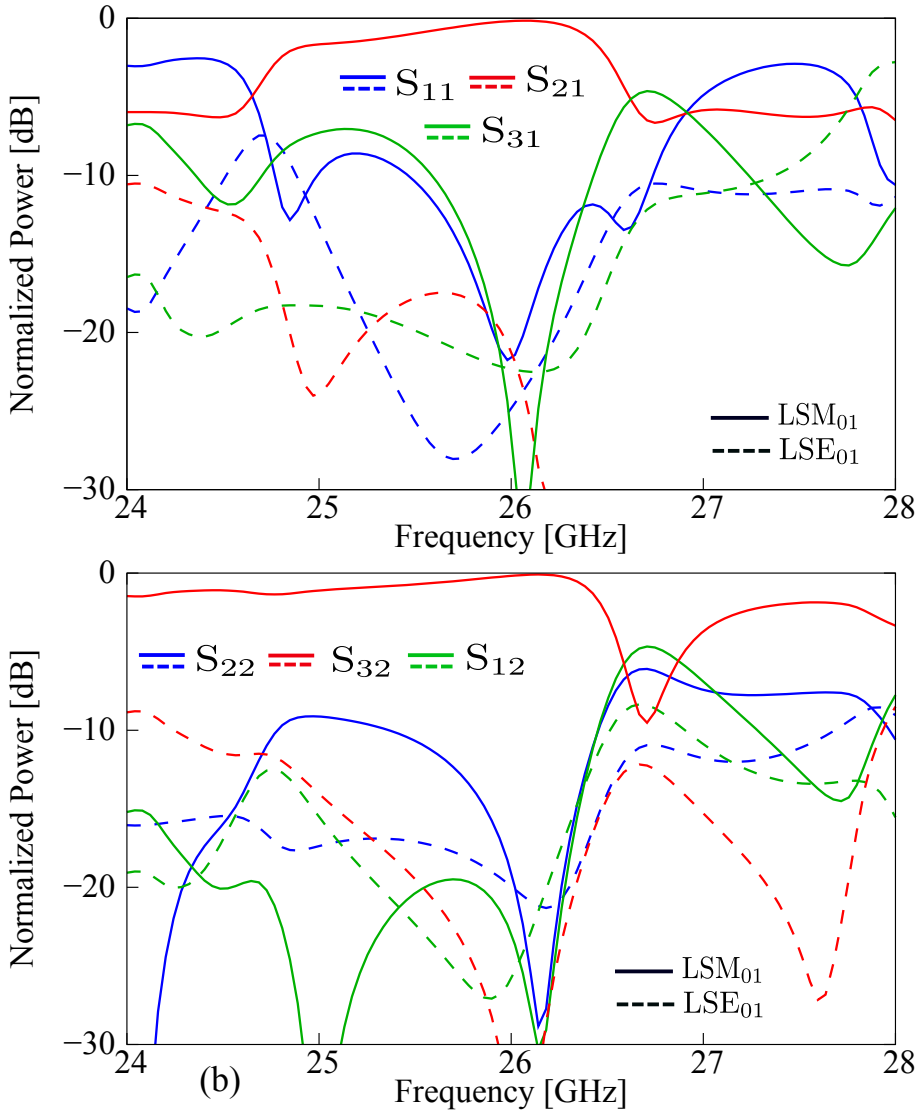

Figure 6.14: Frequency characteristics of the NRD three port isolator (a) when port 1 is input (b) when port 2 is input.

at different frequencies considered in the objective function. The designed device achieved bandwidth around 2.5 GHz and 3 GHz when port 1 and port 2 is input respectively as shown in Fig. 6.17.

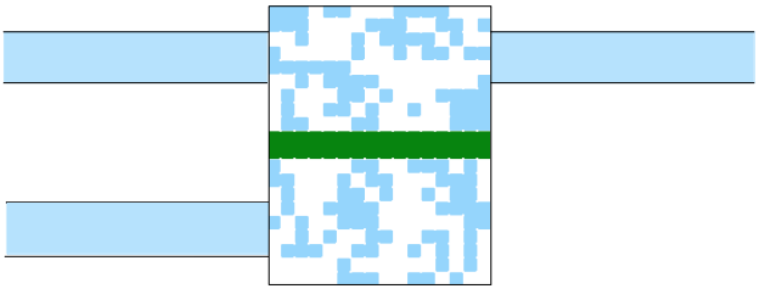

Figure 6.15: Optimal structure of NRD isolator using binary differential evolution algorithm at broadband operation.

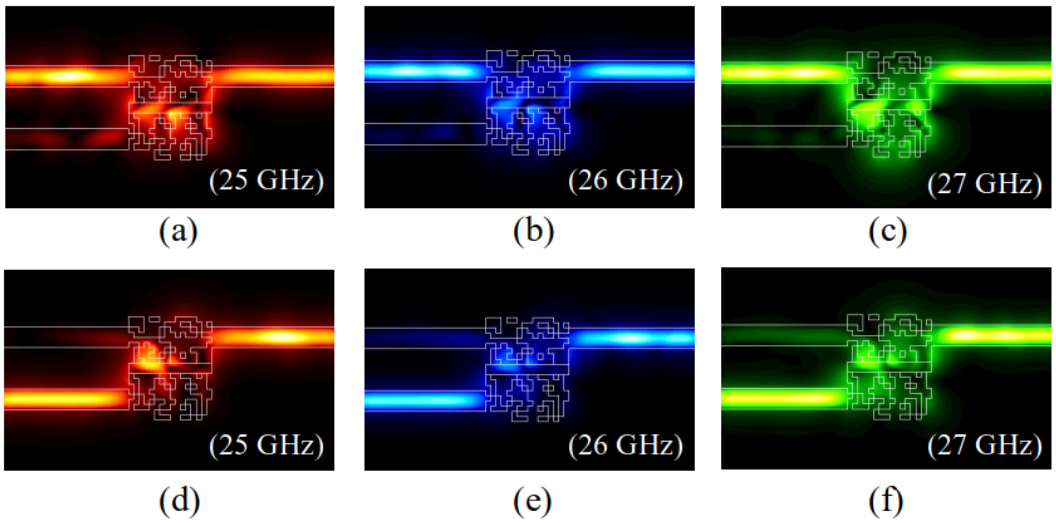

Figure 6.16: The propagating field in the NRD isolator at different frequencies (a-c) transmission at port 2 when port 1 is input (d-f) transmission at port 3 when port 2 is input.

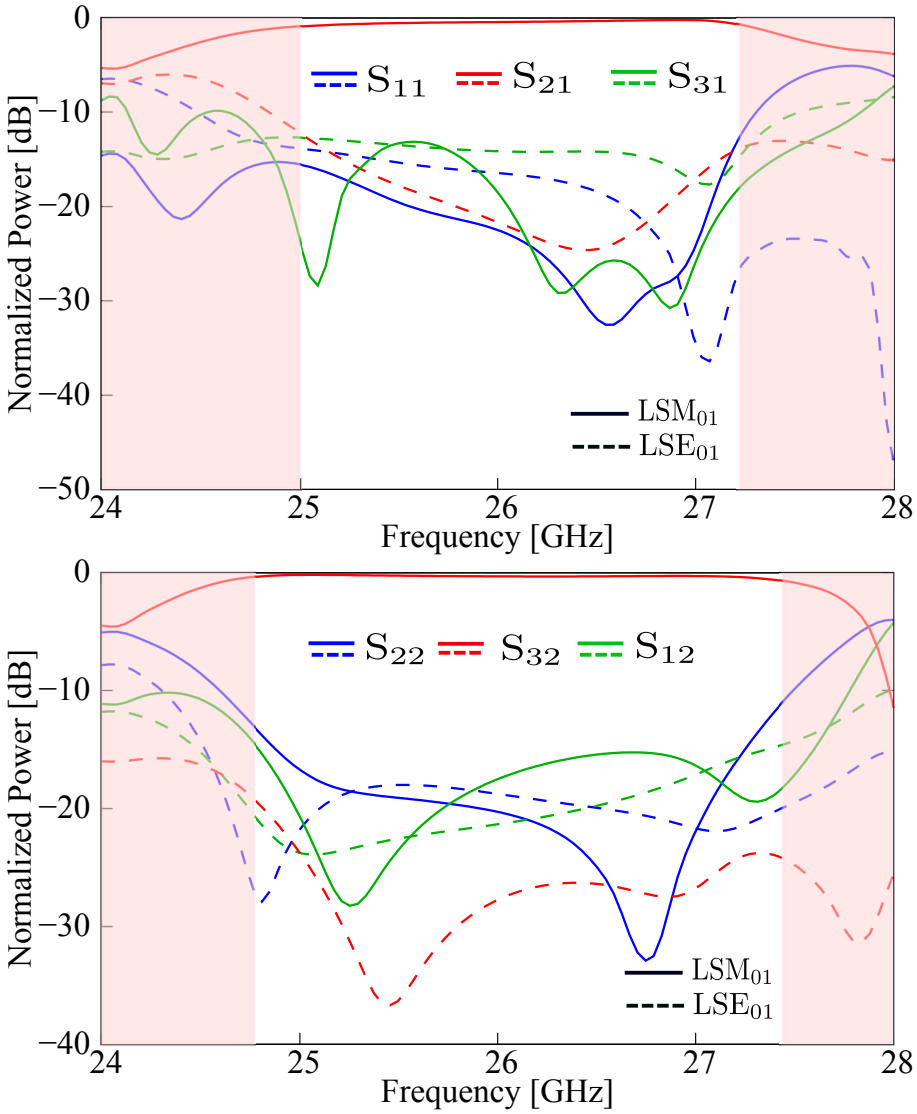

Figure 6.17: Frequency characteristics of the NRD three port isolator at broadband operation (a) when port 1 is input (b) when port 2 is input

Chapter 7

Two-Dimensional Full-Vectorial FDTD Method for NRD Guide

In this chapter we present two-dimensional full-vectorial finite difference time domain method for the efficient analysis of NRD guide devices with three-dimensional structure. Various kinds of electromagnetic simulation techniques have been developed so far. Among them, the finite element method (FEM) [110]-[112] and the finite-difference time-domain (FDTD) [113] method are probably most popular ones. Recently, we have developed two-dimensional full vectorial finite element method (2D-FV-FEM), which can efficiently analyze NRD guide devices without sacrificing numerical accuracy. The 2D-FV-FEM has been successfully utilized for several optimal design of NRD guide devices including dielectric and magnetic materials.

On the other hand, time-domain simulation method is useful for analyzing broadband device properties. The 2D-FV-FEM can be extended into a time domain analysis 2D-FV-FETD, but it could be more challenging as compared to 2D-FV-FDTD. The FDTD scheme is explicit, whereas the 2D-FV-FETD scheme is implicit and requires a long computational time to solve the linear equations. The conventional 2D-FDTD solves only three field components in a two-dimensional waveguide or parallel plate dielectric waveguide with TE wave. It cannot be applied directly to the analysis of hybrid modes LSM_{01} and LSE_{01} in NRD guide. As a result, 3D-FDTD is widely used, but it requires a significant amount of computational time and simulation resources. Two-dimensional full vectorial FDTD (2D-FV-FDTD), has been developed considering out-of-plane oscillation in 1990's [114],[115]. In recent years, few 2D-FDTD methods for various applications have

been proposed in the literature [116]-[120]. However, the applications of 2D-FV-FDTD have been limited to the analysis of rectangular waveguides in microwave band so far.

Therefore, we develop 2D-FV-FDTD method which can rigorously treat NRD guide structures with finite height. In terms of application, our 2D-FV-FDTD method is developed for the analysis of millimeter-wave circuits based on NRD guides. From an algorithmic viewpoint, the proposed method can solve all six field components to treat hybrid modes, such as LSM_{01} and LSE_{01} modes where conventional 2D-FDTD fails to deal with these modes. We use analytic relation to the perpendicular direction of the parallel plates to reduce the spatial dimension to 2D. The forward and backward propagation in all three directions can be considered in our 2D-FV-FDTD method. In our formulation, convolutional perfectly matched layer (CPML) boundary condition developed in 2000's is employed.

Furthermore, we establish a rigorous formulation for estimating the modal power of LSM_{01} and LSE_{01} modes contained in arbitrary propagation fields, which is validated by comparing the results of the proposed 2D-FV-FDTD with recently developed 2D-FV-FEM. The accuracy of 2D-FV-FEM has been verified by 3D-FV-FEM. In this method, the variations of electromagnetic fields are separated into parallel and vertical directions to metal plates and FDTD discretization is applied only to the field variation in the parallel direction. This approach can greatly reduce a computational effort because 3D analysis is not required without sacrificing rigorousness. This method can be used in 5G and beyond 5G to design the NRD waveguide devices with a similar structure in the THz band, but caution is required where conductor loss cannot be ignored. The validity of our approach is confirmed through numerical examples of crossing and T-branch NRD guides.

7.1 FDTD Formulation for NRD Guide Devices

7.1.1 Basic Equation and FDTD Discretization

In NRD guide devices with no structural variation along the z-direction between parallel plates, the dependence of electric and magnetic fields on z can be expressed as follows:

$$E_x, E_y, H_z \propto \sin\left(\frac{\pi}{a}z\right), \quad H_x, H_y, E_z \propto \cos\left(\frac{\pi}{a}z\right). \tag{7.1}$$

Then, Maxwell's equations can be written as (3.5)-(3.10). After discretization using Yee lattice as shown in Fig. 7.1, we can get the following FDTD update equations:

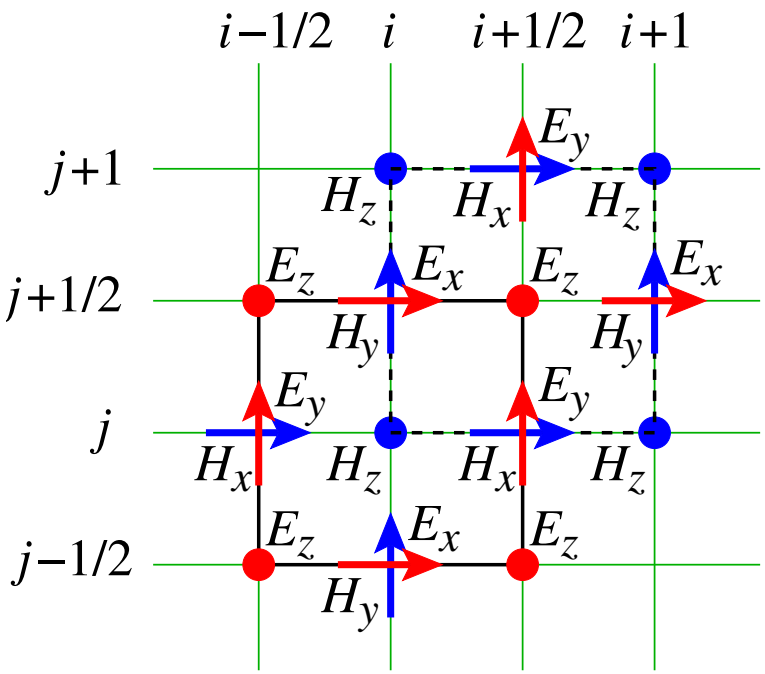

Figure 7.1: Yee lattice used in FDTD method.

$$\frac{\phi_z^{(i+\frac{1}{2},j+\frac{1}{2},n+\frac{1}{2})} - \phi_z^{(i+\frac{1}{2},j-\frac{1}{2},n+\frac{1}{2})}}{\Delta y} - \left(\frac{\pi}{a}\right)\phi_y^{(i+\frac{1}{2},j,n+\frac{1}{2})} = \mu_0 \frac{\psi_x^{(i+\frac{1}{2},j,n+1)} - \psi_x^{(i+\frac{1}{2},j,n)}}{\Delta t} \tag{7.2}$$

$$\left(\frac{\pi}{a}\right)\phi_x^{(i,j+\frac{1}{2},n+\frac{1}{2})} - \frac{\phi_z^{(i+\frac{1}{2},j+\frac{1}{2},n+\frac{1}{2})} - \phi_z^{(i-\frac{1}{2},j+\frac{1}{2},n+\frac{1}{2})}}{\Delta x} = -\mu_0 \frac{\psi_y^{(i,j+\frac{1}{2},n+1)} - \psi_y^{(i,j+\frac{1}{2},n)}}{\Delta t} \tag{7.3}$$

$$\frac{\phi_y^{(i+\frac{1}{2},j,n+\frac{1}{2})} - \phi_y^{(i-\frac{1}{2},j,n+\frac{1}{2})}}{\Delta x} - \frac{\phi_x^{(i,j+\frac{1}{2},n+\frac{1}{2})} - \phi_x^{(i,j-\frac{1}{2},n+\frac{1}{2})}}{\Delta y} = -\mu_0 \frac{\psi_z^{(i,j,n+1)} - \psi_z^{(i,j,n)}}{\Delta t} \tag{7.4}$$

$$\frac{\psi_z^{(i,j+1,n)} - \psi_z^{(i,j,n)}}{\Delta y} + \left(\frac{\pi}{a}\right)\psi_y^{(i,j+\frac{1}{2},n)} = \varepsilon_0\varepsilon_r \frac{\phi_x^{(i,j+\frac{1}{2},n+\frac{1}{2})} - \phi_x^{(i,j+\frac{1}{2},n-\frac{1}{2})}}{\Delta t} \tag{7.5}$$

$$-\left(\frac{\pi}{a}\right)\psi_x^{(i+\frac{1}{2},j,n)} - \frac{\psi_z^{(i+1,j,n)} - \psi_z^{(i,j,n)}}{\Delta x} = \varepsilon_0\varepsilon_r \frac{\phi_y^{(i+\frac{1}{2},j,n+\frac{1}{2})} - \phi_y^{(i+\frac{1}{2},j,n-\frac{1}{2})}}{\Delta t} \tag{7.6}$$

$$\frac{\psi_y^{(i+1,j+\frac{1}{2},n)} - \psi_y^{(i,j+\frac{1}{2},n)}}{\Delta x} - \frac{\psi_x^{(i+\frac{1}{2},j+1,n)} - \psi_x^{(i+\frac{1}{2},j,n)}}{\Delta y} = \varepsilon_0\varepsilon_r \frac{\phi_z^{(i+\frac{1}{2},j+\frac{1}{2},n+\frac{1}{2})} - \phi_z^{(i+\frac{1}{2},j+\frac{1}{2},n-\frac{1}{2})}}{\Delta t} \tag{7.7}$$

The simplified equations are written as follow by replacing the $\phi \to \phi/\sqrt{\varepsilon_0}, \psi \to \psi/\sqrt{\mu_0}, t = cdt$ and $c = 1/\sqrt{\varepsilon_0\mu_0}$ for the actual analysis.

$$\frac{\phi_z^{(i+\frac{1}{2},j+\frac{1}{2},n+\frac{1}{2})} - \phi_z^{(i+\frac{1}{2},j-\frac{1}{2},n+\frac{1}{2})}}{\Delta y} - \left(\frac{\pi}{a}\right)\phi_y^{(i+\frac{1}{2},j,n+\frac{1}{2})} = -\frac{\psi_x^{(i+\frac{1}{2},j,n+1)} - \psi_x^{(i+\frac{1}{2},j,n)}}{\Delta\tau} \tag{7.8}$$

$$\left(\frac{\pi}{a}\right)\phi_x^{(i,j+\frac{1}{2},n+\frac{1}{2})} - \frac{\phi_z^{(i+\frac{1}{2},j+\frac{1}{2},n+\frac{1}{2})} - \phi_z^{(i-\frac{1}{2},j+\frac{1}{2},n+\frac{1}{2})}}{\Delta x} = -\frac{\psi_y^{(i,j+\frac{1}{2},n+1)} - \psi_y^{(i,j+\frac{1}{2},n)}}{\Delta\tau} \tag{7.9}$$

$$\frac{\phi_y^{(i+\frac{1}{2},j,n+\frac{1}{2})} - \phi_y^{(i-\frac{1}{2},j,n+\frac{1}{2})}}{\Delta x} - \frac{\phi_x^{(i,j+\frac{1}{2},n+\frac{1}{2})} - \phi_x^{(i,j-\frac{1}{2},n+\frac{1}{2})}}{\Delta y} = -\frac{\psi_z^{(i,j,n+1)} - \psi_z^{(i,j,n)}}{\Delta\tau} \tag{7.10}$$

$$\frac{\psi_z^{(i,j+1,n)} - \psi_z^{(i,j,n)}}{\Delta y} + \left(\frac{\pi}{a}\right)\psi_y^{(i,j+\frac{1}{2},n)} = \varepsilon_r\frac{\phi_x^{(i,j+\frac{1}{2},n+\frac{1}{2})} - \phi_x^{(i,j+\frac{1}{2},n-\frac{1}{2})}}{\Delta\tau} \tag{7.11}$$

$$-\left(\frac{\pi}{a}\right)\psi_x^{(i+\frac{1}{2},j,n)} - \frac{\psi_z^{(i+1,j,n)} - \psi_z^{(i,j,n)}}{\Delta x} = \varepsilon_r\frac{\phi_y^{(i+\frac{1}{2},j,n+\frac{1}{2})} - \phi_y^{(i+\frac{1}{2},j,n-\frac{1}{2})}}{\Delta\tau} \tag{7.12}$$

$$\frac{\psi_y^{(i+1,j+\frac{1}{2},n)} - \psi_y^{(i,j+\frac{1}{2},n)}}{\Delta x} - \frac{\psi_x^{(i+\frac{1}{2},j+1,n)} - \psi_x^{(i+\frac{1}{2},j,n)}}{\Delta y} = \varepsilon_r\frac{\phi_z^{(i+\frac{1}{2},j+\frac{1}{2},n+\frac{1}{2})} - \phi_z^{(i+\frac{1}{2},j+\frac{1}{2},n-\frac{1}{2})}}{\Delta\tau} \tag{7.13}$$

7.1.2 Convolutional Perfectly Matched Layer (CPML)

The stretching coefficient $s\omega\,(\omega = x, y, z)$ in CPML are expressed below

$$s_w = k_w + \frac{\sigma_w}{\alpha_w + j\omega}$$

where k is stretching coefficient, σ is a medium conductivity, α is a complex frequency shift parameters and $j\omega = j\omega\varepsilon_0$ where ε_0 is permittivity and its equal to 1. Stretched coordinates in complex form is as follow.

$$\frac{j\omega}{c}\varepsilon_r\boldsymbol{E} = \boldsymbol{i}_x\left(\frac{1}{s_y}\frac{\partial\boldsymbol{H}_z}{\partial y} - \frac{1}{s_z}\frac{\partial\boldsymbol{H}_y}{\partial z}\right) + \boldsymbol{i}_y\left(\frac{1}{s_z}\frac{\partial\boldsymbol{H}_x}{\partial z} - \frac{1}{s_x}\frac{\partial\boldsymbol{H}_z}{\partial x}\right) + \boldsymbol{i}_z\left(\frac{1}{s_x}\frac{\partial\boldsymbol{H}_y}{\partial x} - \frac{1}{s_y}\frac{\partial\boldsymbol{H}_x}{\partial y}\right) \tag{7.14}$$

$$-\frac{j\omega}{c}\mu_r\boldsymbol{H} = \boldsymbol{i}_x\left(\frac{1}{s_y}\frac{\partial\boldsymbol{E}_z}{\partial y} - \frac{1}{s_z}\frac{\partial\boldsymbol{E}_y}{\partial z}\right) + \boldsymbol{i}_y\left(\frac{1}{s_z}\frac{\partial\boldsymbol{E}_x}{\partial z} - \frac{1}{s_x}\frac{\partial\boldsymbol{E}_z}{\partial x}\right) + \boldsymbol{i}_z\left(\frac{1}{s_x}\frac{\partial\boldsymbol{E}_y}{\partial x} - \frac{1}{s_y}\frac{\partial\boldsymbol{E}_x}{\partial y}\right) \tag{7.15}$$

The time domain conversion of stretched coordinates is given below

$$\varepsilon_r \frac{\partial \boldsymbol{E}}{\partial \tau} = \boldsymbol{i}_x \left(\bar{s}_y * \frac{\partial \boldsymbol{H}_z}{\partial y} - \bar{s}_z * \frac{\partial \boldsymbol{H}_y}{\partial z} \right) + \boldsymbol{i}_y \left(\bar{s}_z * \frac{\partial \boldsymbol{H}_x}{\partial z} - \bar{s}_x * \frac{\partial \boldsymbol{H}_z}{\partial x} \right) + \boldsymbol{i}_z \left(\bar{s}_x * \frac{\partial \boldsymbol{H}_y}{\partial x} - \bar{s}_x * \frac{\partial \boldsymbol{H}_x}{\partial y} \right) \tag{7.16}$$

$$-\mu_r \frac{\partial \boldsymbol{H}}{\partial \tau} = \boldsymbol{i}_x \left(\bar{s}_y * \frac{\partial \boldsymbol{E}_z}{\partial y} - \bar{s}_z * \frac{\partial \boldsymbol{E}_y}{\partial z} \right) + \boldsymbol{i}_y \left(\bar{s}_z * \frac{\partial \boldsymbol{E}_x}{\partial z} - \bar{s}_x * \frac{\partial \boldsymbol{E}_z}{\partial x} \right) + \boldsymbol{i}_z \left(\bar{s}_x * \frac{\partial \boldsymbol{E}_y}{\partial x} - \bar{s}_x * \frac{\partial \boldsymbol{E}_x}{\partial y} \right) \tag{7.17}$$

Where $*$ indicate the convolutional integral and $\bar{s}_\omega$ is the inverse fourier transform of $1/\bar{s}_\omega$. To derive the CPML in time domain, the fourier transform of $\bar{s}_\omega$ is required.

$$\bar{s}(t) = \mathcal{F}^{-1} \left\{ \frac{1}{k_w + \frac{\sigma_w}{\alpha_w + j\omega}} \right\} = \frac{\delta(t)}{k_w} - \frac{\sigma_w}{k_w^2} \exp\left(- \left(\frac{\sigma_w}{k_w} + \alpha_w \right) t \right) U(t) = \frac{\delta(t)}{k_w} + \eta_w(t) \tag{7.18}$$

Where $\delta(t)$and $U(t)$ are unit impulse and unit step function respectively. Substitute (7.18) into (7.16) and (7.17) gives the following time domain expression

$$\varepsilon_r \frac{\partial \boldsymbol{E}}{\partial \tau} = \boldsymbol{i}_x \left(\frac{1}{k_y} \frac{\partial \boldsymbol{H}_z}{\partial y} - \frac{1}{k_z} \frac{\partial \boldsymbol{H}_y}{\partial z} \right) + \boldsymbol{i}_y \left(\frac{1}{k_z} \frac{\partial \boldsymbol{H}_x}{\partial z} - \frac{1}{k_x} \frac{\partial \boldsymbol{H}_z}{\partial x} \right) + \boldsymbol{i}_z \left(\frac{1}{k_x} \frac{\partial \boldsymbol{H}_y}{\partial x} - \frac{1}{k_y} \frac{\partial \boldsymbol{H}_x}{\partial y} \right) + \boldsymbol{i}_x \left(\eta_y * \frac{\partial \boldsymbol{H}_z}{\partial y} - \eta_z * \frac{\partial \boldsymbol{H}_y}{\partial z} \right) + \boldsymbol{i}_y \left(\eta_z * \frac{\partial \boldsymbol{H}_x}{\partial z} - \eta_x * \frac{\partial \boldsymbol{H}_z}{\partial x} \right) + \boldsymbol{i}_z \left(\eta_x * \frac{\partial \boldsymbol{H}_y}{\partial x} - \eta_y * \frac{\partial \boldsymbol{H}_x}{\partial y} \right) \tag{7.19}$$

$$-\mu_r \frac{\partial \boldsymbol{H}}{\partial \tau} = \boldsymbol{i}_x \left(\frac{1}{k_y} \frac{\partial \boldsymbol{E}_z}{\partial y} - \frac{1}{k_z} \frac{\partial \boldsymbol{E}_y}{\partial z} \right) + \boldsymbol{i}_y \left(\frac{1}{k_z} \frac{\partial \boldsymbol{E}_x}{\partial z} - \frac{1}{k_x} \frac{\partial \boldsymbol{E}_z}{\partial x} \right) + \boldsymbol{i}_z \left(\frac{1}{k_x} \frac{\partial \boldsymbol{E}_y}{\partial x} - \frac{1}{k_y} \frac{\partial \boldsymbol{E}_x}{\partial y} \right) + \boldsymbol{i}_x \left(\eta_y * \frac{\partial \boldsymbol{E}_z}{\partial y} - \eta_z * \frac{\partial \boldsymbol{E}_y}{\partial z} \right) + \boldsymbol{i}_y \left(\eta_z * \frac{\partial \boldsymbol{E}_x}{\partial z} - \eta_x * \frac{\partial \boldsymbol{E}_z}{\partial x} \right) + \boldsymbol{i}_z \left(\eta_x * \frac{\partial \boldsymbol{E}_y}{\partial x} - \eta_y * \frac{\partial \boldsymbol{E}_x}{\partial y} \right) \tag{7.20}$$

Here, the calculation of the convolution integral should be performed by recursive convolution (RC) as follows

$$\Phi_{w,v} = \eta_w * \frac{\partial H_v}{\partial w} \tag{7.21}$$

and considering that $\eta_w(t)$ and $H_v(t)$ have values only at $t > 0$

$$\Phi_{w,v}(t) = \int_{-\infty}^{\infty} \eta_w(t-u)\frac{\partial H_v(u)}{\partial w}du = \int_0^t -\frac{\sigma_w}{k_w^2}\exp\left[-\left(\frac{\sigma_w}{k_w}+\alpha_w\right)(t-u)\right]\frac{\partial H_v(u)}{\partial w}du \tag{7.22}$$

$$\begin{aligned}
\Phi_{w,v}(t+dt) &= \int_0^{t+\Delta t} -\frac{\sigma_w}{k_w^2}\exp\left[-\left(\frac{\sigma_w}{k_w}+\alpha_w\right)(t+\Delta t-u)\right]\frac{\partial H_v(u)}{\partial w}du \\
&= \int_0^t -\frac{\sigma_w}{k_w^2}\exp\left[-\left(\frac{\sigma_w}{k_w}+\alpha_w\right)(t+\Delta t-u)\right]\frac{\partial H_v(u)}{\partial w}du \\
&\quad + \int_t^{t+\Delta t} -\frac{\sigma_w}{k_w^2}\exp\left(-\left(\frac{\sigma_w}{k_w}+\alpha_w\right)(t+\Delta t-u)\right)\frac{\partial H_v(u)}{\partial w}du \\
&\simeq \exp\left[-\left(\frac{\sigma_w}{k_w}+\alpha_w\right)\Delta t\right]\int_0^t -\frac{\sigma_w}{k_w^2}\exp\left[-\left(\frac{\sigma_w}{k_w}+\alpha_w\right)(t-u)\right]\frac{\partial H_v(u)}{\partial w}du \\
&\quad + \left\{\int_t^{t+\Delta t} -\frac{\sigma_w}{k_w^2}\exp\left[-\left(\frac{\sigma_w}{k_w}+\alpha_w\right)(t+\Delta t-u)\right]du\right\}\left.\frac{\partial H_v(u)}{\partial w}\right|_{u=t+\Delta/2} \\
&= b_w\Phi_{w,v}(t) - \left[\frac{\sigma_w}{k_w^2}\frac{\exp\left[-\left(\frac{\sigma_w}{k_w}+\alpha_w\right)(t+\Delta t-u)\right]}{\frac{\sigma_w}{k_w}+\alpha_w}\right]_t^{t+\Delta t}\left.\frac{\partial H_v(u)}{\partial w}du\right|_{u=t+\Delta/2} \\
&= b_w\Phi_{w,v}(t) + \frac{\sigma_w}{k_w(\sigma_w+\alpha_w k_w)}(b_w-1)\left.\frac{\partial H_v(u)}{\partial w}du\right|_{u=t+\Delta/2} \\
&= b_w\Phi_{w,v}(t) + c_w\left.\frac{\partial H_v(u)}{\partial w}du\right|_{u=t+\Delta/2}
\end{aligned} \tag{7.23}$$

where b_w and c_w are

$$b_w = \exp\left[-\left(\frac{\sigma_w}{k_w}+\alpha_w\right)c\Delta t\right] \tag{7.24}$$

$$c_w = \frac{\sigma_w}{k_w(\sigma_w+\alpha_w k_w)}(b_w-1) \tag{7.25}$$

FDTD time and space discretization of Amperes law with CPML yields explicit update of filed components are as follow.

$$E_x^{(n+1/2)} = C_{ax}E^{(n-1/2)} + C_{bx}\left(\frac{1}{k_y}\frac{\partial H_z^{(n)}}{\partial y} - \frac{1}{k_z}\frac{\partial H_y^{(n)}}{\partial z} + \Phi_{y,z}^{(n)} - \Phi_{z,y}^{(n)}\right) \quad (7.26)$$

$$E_y^{(n+1/2)} = C_{ay}E^{(n-1/2)} + C_{by}\left(\frac{1}{k_z}\frac{\partial H_x^{(n)}}{\partial z} - \frac{1}{k_x}\frac{\partial H_z^{(n)}}{\partial x} + \Phi_{z,x}^{(n)} - \Phi_{x,z}^{(n)}\right) \quad (7.27)$$

$$E_z^{(n+1/2)} = C_{az}E^{(n-1/2)} + C_{bz}\left(\frac{1}{k_x}\frac{\partial H_y^{(n)}}{\partial x} - \frac{1}{k_y}\frac{\partial H_x^{(n)}}{\partial y} + \Phi_{x,y}^{(n)} - \Phi_{y,x}^{(n)}\right) \quad (7.28)$$

$$H_x^{(n+1)} = D_{ax}E^{(n-1)} - D_{bx}\left(\frac{1}{k_y}\frac{\partial E_z^{(n+1/2)}}{\partial y} - \frac{1}{k_z}\frac{\partial E_y^{(n+1/2)}}{\partial z} + \Psi_{y,z}^{(n+1/2)} - \Psi_{z,y}^{(n+1/2)}\right) \quad (7.29)$$

$$H_y^{(n+1)} = D_{ay}E^{(n-1)} - D_{by}\left(\frac{1}{k_z}\frac{\partial E_x^{(n+1/2)}}{\partial z} - \frac{1}{k_x}\frac{\partial E_z^{(n+1/2)}}{\partial x} + \Psi_{z,x}^{(n+1/2)} - \Psi_{x,z}^{(n+1/2)}\right) \quad (7.30)$$

$$H_z^{(n+1)} = D_{az}E^{(n-1)} - D_{bz}\left(\frac{1}{k_x}\frac{\partial E_y^{(n+1/2)}}{\partial x} - \frac{1}{k_y}\frac{\partial E_x^{(n+1/2)}}{\partial y} + \Psi_{x,y}^{(n+1/2)} - \Psi_{y,x}^{(n+1/2)}\right) \quad (7.31)$$

Coefficients $C_{a\xi}$, $C_{b\xi}$, $D_{a\xi}$, and $D_{b\xi}$ are written as follow

$$C_{a\xi} = 1, \quad C_{b\xi} = \frac{\Delta\tau}{\varepsilon_r}, \quad D_{a\xi} = 1, \quad D_{b\xi} = \frac{\Delta\tau}{\mu_r} \quad (7.32)$$

When dealing with a conductive medium or a magnetically permeable medium, let the conductivity be σ_e and the magnetic permeability be σ_m

$$\varepsilon_r\frac{\partial \boldsymbol{E}}{\partial\tau} \quad \rightarrow \quad \varepsilon_r\frac{\partial \boldsymbol{E}}{\partial\tau} + \sigma_e\boldsymbol{E} \quad (7.33)$$

$$\mu_r\frac{\partial \boldsymbol{H}}{\partial\tau} \quad \rightarrow \quad \mu_r\frac{\partial \boldsymbol{H}}{\partial\tau} + \sigma_m\boldsymbol{H} \quad (7.34)$$

Therefore, $C_{a\xi}$, $C_{b\xi}$, $D_{a\xi}$, and $D_{b\xi}$ can be written as follow

$$C_{a\xi} = \frac{1 - \frac{\sigma_e\Delta\tau}{2\varepsilon_r}}{1 + \frac{\sigma_e\Delta\tau}{2\varepsilon_r}}, \quad C_{b\xi} = \frac{\frac{\Delta\tau}{\varepsilon_r}}{1 + \frac{\sigma_e\Delta\tau}{2\varepsilon_r}},$$

$$D_{a\xi} = \frac{1 - \frac{\sigma_m\Delta\tau}{2\mu_r}}{1 + \frac{\sigma_m\Delta\tau}{2\mu_r}}, \quad D_{b\xi} = \frac{\frac{\Delta\tau}{\mu_r}}{1 + \frac{\sigma_m\Delta\tau}{2\mu_r}} \quad (7.35)$$

7.1.3 Evaluation of Frequency Spectrum using Fourier Transform

In order to evaluate frequency characteristics of transmission and reflection power, we have to calculate Fourier transform of time-dependent modal amplitude at reference plane. The modal amplitude of reference plane is calculated by the following overlap integral with each modal field at each time step:

$$a_{\mathrm{LSM}_{01}} = \int_{\Gamma} \frac{1}{\varepsilon_r} \tilde{H}_z^{\mathrm{LSM}_{01}} \tilde{H}_z d\Gamma \quad \text{for LSM}_{01} \text{ mode} \tag{7.36}$$

$$a_{\mathrm{LSE}_{01}} = \int_{\Gamma} \tilde{E}_z^{\mathrm{LSE}_{01}} \tilde{E}_z d\Gamma \quad \text{for LSE}_{01} \text{ mode} \tag{7.37}$$

After calculating time evolutions of modal amplitudes and their Fourier transforms, normalized power of target mode (MODE : LSM_{01} or LSE_{01}) is calculated as follows:

$$P_{\mathrm{MODE}} = \frac{\beta_{\mathrm{LSM}_{01}} \left\{(\pi/a)^2 + \beta_{\mathrm{MODE}}^2\right\}}{\beta_{\mathrm{MODE}} \left\{(\pi/a)^2 + \beta_{\mathrm{LSM}_{01}}^2\right\}} \frac{\left|A_{\mathrm{MODE}}\right|^2}{\left|A_{\mathrm{LSM}_{01}}^{(\mathrm{in})}\right|^2} \tag{7.38}$$

where A_{MODE} and $A_{\mathrm{LSM}_{01}}^{(\mathrm{in})}$ are Fourier transforms of a_{MODE} and the modal amplitude of the incidence wave, respectively.

7.2 Numerical Examples

In order to verify the accuracy of the proposed 2D-FV-FDTD method, we consider two types of NRD guide components. The separation between metal plates of NRD guide is assumed to be $a = 2.25$ mm and width of the dielectric strip between these plates is $b = 2$ mm with relative permittivity $\varepsilon_r = 2.2$. The surrounding region is assumed to be air with relative permittivity $\varepsilon_{\mathrm{air}} = 1$. Furthermore, LSM_{01} Gaussian pulse with center frequency of 60 GHz is considered for excitation at input port 1.

7.2.1 Crossing Waveguide

First, we consider an NRD crossing waveguide whose geometrical parameters are as follow: $W_x = 60$ mm, $W_y = 40$ mm, $l_1 = 5$ mm, $l_2 = 24$ mm, and $d_{\mathrm{PML}} = 10$ mm as shown in Fig. 7.2. The computational region is discretized using Yee lattice with size of $\Delta x = \Delta y = 0.05$ mm and time step $\Delta t = \Delta x/2c$ ($< \Delta t_{\mathrm{CFL}}$) where c is the light velocity and $\Delta t_{\mathrm{CFL}} = \Delta x/(\sqrt{2}c)$ is the upper limit for the time step under the CFL condition. The time step size is Δt = 83.4 fs and the total number of time steps

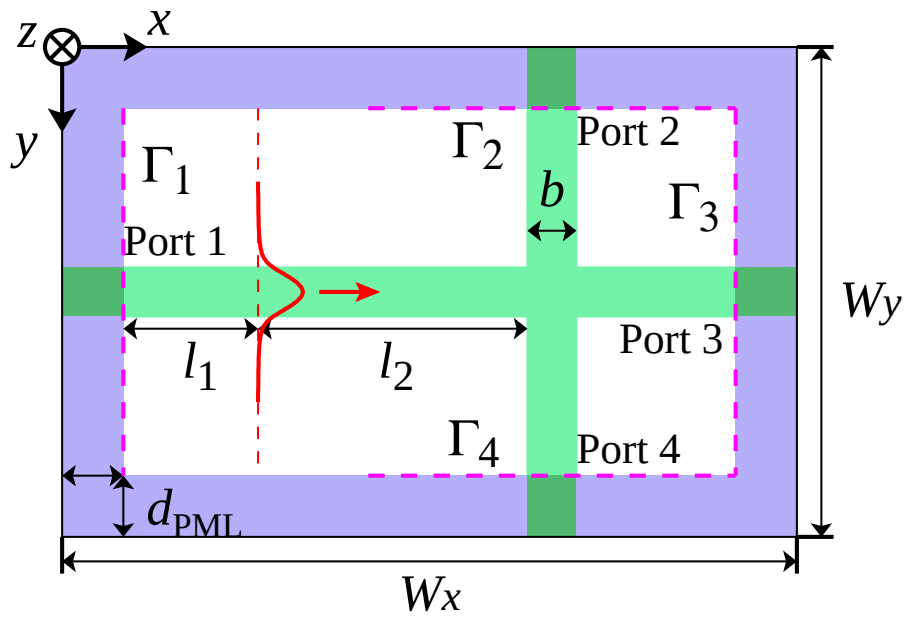

Figure 7.2: Schematic diagram of NRD crossing waveguide.

is 80,000 for the developed 2D-FV-FDTD. In this numerical example, Gaussian time pulse is excited at $x = 15$ mm and time evolution of modal amplitudes are observed at four reference planes, $\Gamma_{1\sim4}$, in port $1 \sim 4$ as shown in Fig. 7.3. Since the excitation is symmetrically given to $\pm x$-directions, the first peak in the port 1 corresponds to the incident pulse and the following wave corresponds to reflected wave. The propagation fields in the crossing waveguide at some different time steps are shown in Fig. 7.3. Fig. 7.4 shows the frequency characteristics of the crossing waveguide calculated by the proposed method and the 2D-FV-FEM whose validity is confirmed by comparing with 3D-FV-FEM. In Fig. 7.4, LSM_{01} mode of 2D-FV-FDTD is slightly off with 2D-FV-FEM due to strong frequency dependence around 60 GHz as compare to LSE_{01} mode. The accuracy may degrade more at lower frequencies due to strong modal dispersion near the cut-off frequency. Although LSM_{01} mode is slightly off but both results are in good agreement and the effectiveness and usefulness of the proposed method are confirmed.

7.2.2 T-branch Waveguide

As an another numerical example, we consider a T-branch waveguide as shown in Fig. 7.5. The analysis model is the same as the previous one except that

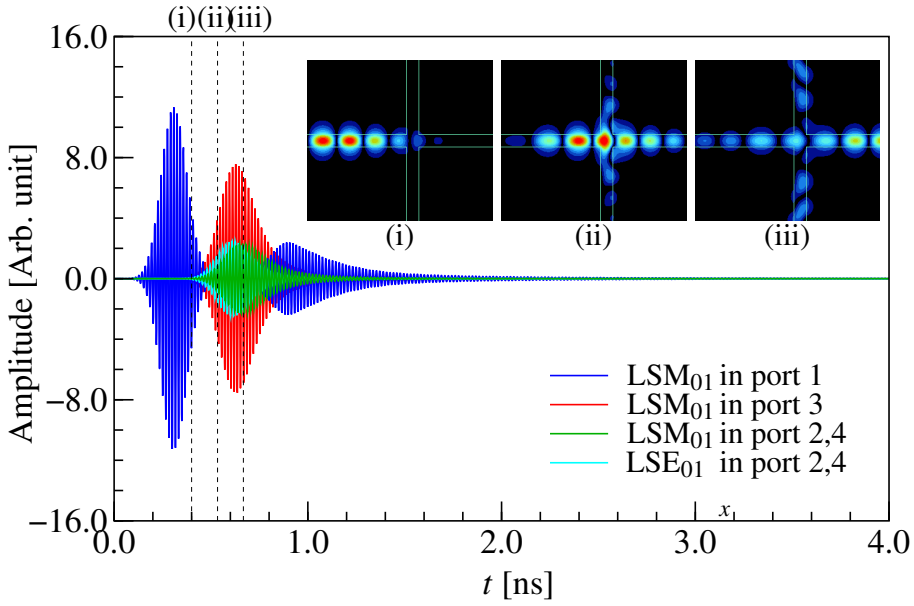

Figure 7.3: Time evolutions of modal amplitudes at the reference plane 1 ($x = 10$ mm), reference plane 2 ($y = 10$ mm), reference plane 3 ($y = 30$ mm) and reference plane 4 ($y = 30$ mm). Time evolutions of both LSM_{01} and LSE_{01} modes are evaluated.

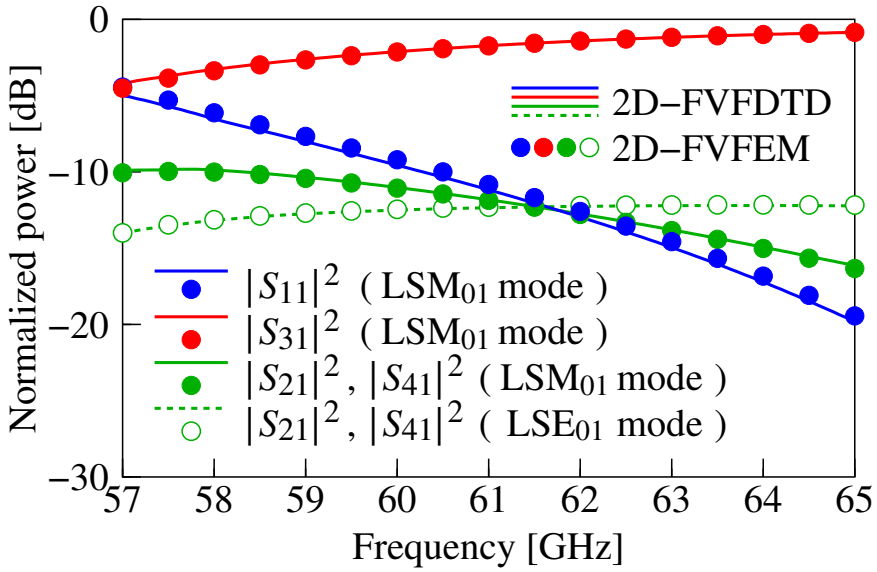

Figure 7.4: Frequency characteristics of crossing waveguide.

port 3 is removed. The time evolutions at reference planes and propagating fields at three different time steps are shown in Fig. 7.6. Fig. 7.7 shows the frequency characteristics of the T-branch waveguide calculated by the proposed method and the 2D-FV-FEM. We can see that both results are in good agreement in this numerical

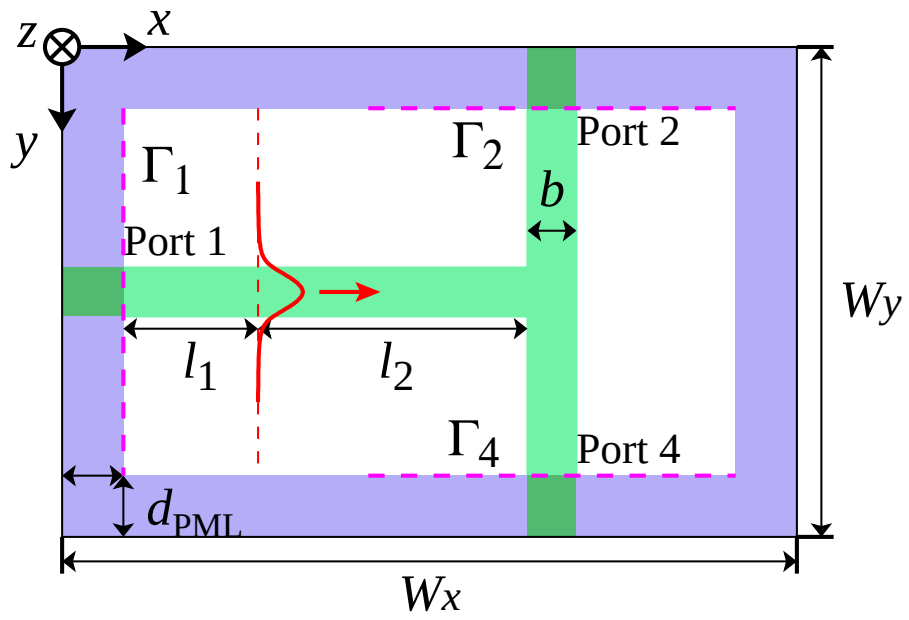

Figure 7.5: Schematic diagram of NRD T-branch waveguide.

Table 7.1: Comparison of computational cost between different simulation methods

Methods	Time [min.]	Memory [GB]
2D-FVFDTD	7.32	1.1
3D-FVFDTD	329.4	49.5
2D-FVFEM	2.24	0.2
3D-FVFEM	628.3	78.8

The above times are for calculating 80,000 time steps in FDTD and for 100 frequencies in FEM.

example too. If 3D analysis is necessary in the numerical examples considered here, 45 times more unknowns are required than with our 2D-FVFDTD method, because the parallel plate separation is 2.25 mm and the Yee lattice size is 0.05 mm in each direction is used. As a result, when compared to the 3D-FDTD approach, both computing time and memory requirements can be reduced by a factor of 45. The computational cost of the proposed 2D-FV-FDTD method and comparison with other simulation methods is shown in Table 7.1. The 2D-FV-FDTD analysis used only 7.32 min. with 1.1 GB of memory for computation at Intel(R) Xeon(R) Gold 6242 CPU @ 2.80 GHz. We can see how efficient our originally developed 2D algorithms are for 3D structures.

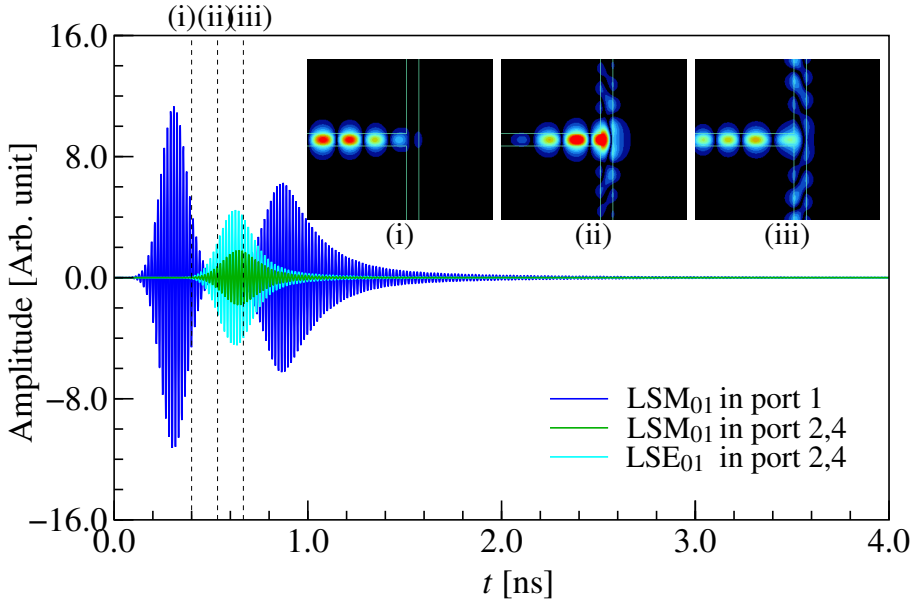

Figure 7.6: Time evolutions of modal amplitudes at the reference plane 1 ($x = 10$ mm), reference plane 2 ($y = 10$ mm), and reference plane 4 ($y = 30$ mm). Time evolutions of both LSM_{01} and LSE_{01} modes are evaluated.

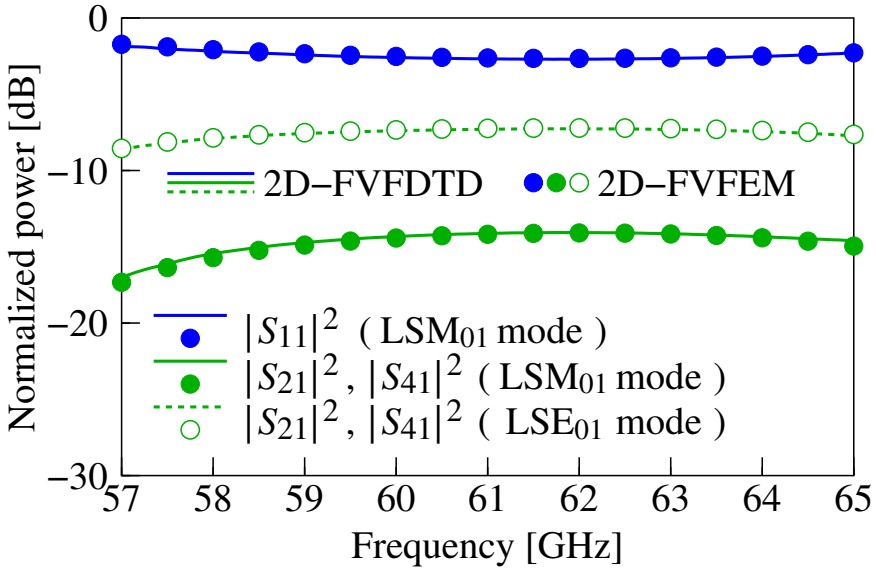

Figure 7.7: Frequency characteristics of T-branch waveguide.

Chapter 8

Conclusion and Future Work

8.1 Conclusion

In this thesis, several optimal design approaches based on mosaic optimization concepts have been developed for the material distribution in the design region of NRD guide devices. In order to improve the design efficiency, we proposed two-dimensional simulation methods including finite element and time domain methods for the efficient analysis of NRD guide devices. In order to show the accuracy and usefulness of simulation and optimization methods we considered several NRD guide devices in microwave and millimeter-wave band. Using the originally developed simulation and optimization methods we have designed several optimal NRD guide devices. The ultimate goal beyond the development of these methods is to develop the high-performance compact microwave and millimeter-wave circuit using basic NRD circuit components.

In chapter 1, we presented the background of different guiding technologies and their limitation in microwave and millimeter-wave band. We also discussed how NRD guide technology is better than these conventional technologies. In order to show, how our thesis research work is unique and different we also investigated the literature of NRD guide in detail.

In chapter 2, first, we have introduced the NRD guide with its operational principle and propagating modes. Then, the advantages and limitations of NRD guide. After that, we have fully described the purpose and goals of our research work.

In chapter 3, we developed two-dimensional full-vectorial finite element methods with uniformity structure of NRD guide along metal parallel plates. Our 2D-FV-FEM can rigorously treat the 3D structure of NRD guide in 2D space. We

have explained the detailed formulation of 2D-FV-FEM using mixed edge/nodal element. To show the validity of developed simulation methods we also studied the guided mode and propagation analysis by considering NRD guide device. The accuracy and efficiency is confirmed by comparing the simulation results of 2D-FV-FEM with 3D-FV-FEM. In this chapter, we confirmed that the originally developed 2D-FV-FEM is highly efficient and can be useful for the optimal design of NRD guide devices.

In chapter 4, we developed two optimal design approaches based on mosaic optimization concepts which includes direct binary search algorithm and genetic algorithm for NRD guide devices. We coupled the originally developed 2D-FV-FEM with these optimization algorithms. In order to demonstrate the usefulness and effectiveness of these approaches, we considered several NRD guide devices including crossing waveguide, 90°-bend, T-branch, and Z-bend waveguide at 60 GHz. After detailed investigation, we confirmed that the DBS algorithm have enough ability only to optimize the design region of simple NRD guide structure at single frequency operation. However, GA is more appropriate choice over DBS for complex device structures and for broadband operation. In this chapter, we confirmed that our approaches are applicable to design other integrated NRD based guide devices and also contributes to increase the device functionality.

In chapter 5, we developed a set of evolutionary approaches using digital material concept for the efficient optimization of NRD guide devices. Binary representation-based GA, DEA, HSA, FA, and PSO are developed to efficiently optimize the material distribution in the design region of NRD guide devices. Four NRD circuit components including low crosstalk waveguide crossing, T-branch power splitter, bending waveguide and frequency demultiplexer are designed, and achieved high transmission throughput greater than 99.9%, 49.9%:49.9%, 99.9% at 60 GHz and 96.4%, 98.5% at 59 GHz and 61 GHz respectively. Furthermore, same devices except frequency demultiplexer are designed at broadband operation using modified objective function. Through comparative study we found that developed evolutionary approaches are highly efficient for single frequency operation. However, it is quite challenging for broadband operation because of several frequencies in the objective function and structural limitation. We have achieved quite impressive results from proposed devices with minimal reflection and crosstalk level due to

highly efficient optimization approaches. The proposed NRD guide devices may also have a potential to realize a high-performance NRD based millimeter wave circuit.

In chapter 6, we extended two-dimensional full-vectorial finite element method for the analysis of NRD guide devices using magnetic material with structural uniformity in the normal direction. In order to show the validity of the proposed method, NRD cross-shaped circulator and isolator are considered at 26 GHz. Binary harmony search algorithm and differential evolution algorithms based on mosaic optimization concepts are considered for single frequency and broadband operation respectively. The circulator is designed by imposing 90 degree rotational symmetry in the design region. In this design example, the wave is directed from port 1 to port 2, and may be reversed by changing the direction of the applied magnetic field. The considered design example is efficiently simulated by developed 2D-FV-FEM and it achieve maximum transmission about -0.3 dB and maximum crosstalk in LSM_{01} mode is -17.7 dB at 26 GHz. The same device at broadband operation achieved bandwidth around 2 GHz. On the other hand, a rod-shaped ferrite post is inserted in the mid of the design region of NRD three port isolator. Excellent forward transmission and backward rejection are achieved by the proposed device, -0.18 dB and -23 dB respectively. The designed device achieved bandwidth at broadband operation around 2 GHz and 3 GHz when port 1 and port 2 is input respectively.

In chapter 7, we proposed rigorous two-dimensional full-vectorial finite difference time domain methods for the efficient analysis of NRD guide devices. We have explained the detailed formulation of developed 2D-FV-FDTD method. Convolutional perfectly matched layer (CPML) is employed as an absorbing boundary condition. A rigorous formulation for estimating the modal power of each LSM_{01} and LSE_{01} mode is derived as well. The validity is confirmed by considering two NRD guide devices including crossing waveguide and T-branch waveguide. Excellent accuracy is achieved by the cross comparison of 2D-FV-FDTD results with 2D-FV-FEM described in chapter 3.

8.2 Future Work

In the future work, we will design more efficient, sensitive and sophisticated optimal design approaches and numerical simulation methods for NRD guide devices. Our future research directions are as follow:

- Design of sub-wavelength grating NRD guide using single mode operation by suppressing LSE mode.
- Optimal design of more advanced and functional devices based on NRD guide.
- Optimal design of broadband NRD guide devices using 2D-FV-FDTD method for millimeter-wave applications.
- Optimal design of ultra-compact and ultra-broadband NRD guide devices at THz band for future communication systems.

Reference

[1] H. H. Meinel, "Commercial applications of millimeter-waves, history, present status and future trends," *IEEE Trans. Microwave Theory and Tech.*, vol. 43, no. 07, pp. 1639 – 1653, July 1995.

[2] P. Russer, "Si and SiGe millimeter-wave integrated circuits," *IEEE Trans. Microwave Theory and Tech.*, vol. 46, no. 05, pp. 590 – 603, May 1998.

[3] T. Yoneyama, "Millimeter-wave research activities in Japan," *IEEE Trans. Microwave Theory and Tech.*, vol. 46, no. 06, pp. 727– 733, June 1998.

[4] S. K. Koul, "Millimeter wave and optical dielectric integrated guides and circuits," *John Wiley Sons*, New York, 1997.

[5] K. Wu and L. Han, "Hybrid integration technology of planar circuits and NRD-guide for cost-effective microwave and millimeter-wave applications," *IEEE Trans. Microwave Theory and Tech.*, vol. 45, no. 6, pp. 946-954, Dec. 1997.

[6] J. Luy, K. Strohm, H. Sasse, A. Schuppen, J. Buechler, M. Willitzer, A. Gruhle, F. Schaffler, U. Guettich, and A. Klaaben, "Si/SiGe MMIC's," *IEEE Trans. Microwave Theory and Tech.*, vol. 43, no. 7, pp. 705-713, April 1995.

[7] C. Warns, W. Menzel, and H. Schumacher, "Transmission lines and passive elements for multilayer coplanar circuits on silicon," *IEEE Trans. Microwave Theory and Tech.*, vol. 46, no. 7, pp. 616-621, May 1998.

[8] T. Yoneyama and S. Nishida, "Nonradiative dielectric waveguide for millimeter-wave integrated circuits," *IEEE Trans. Microwave Theory and Tech.*, vol. 29, no. 11, pp. 1188-1192, Nov. 1981.

[9] J. W. E Griemsmann and L. Birenbaum, "A low-loss H-guide for millimeter wavelengths," *In Proc. Symposium on Millimeter Waves, Polytechnic Institute of Brooklyn, NY, USA*, March 1959.

[10] T. Yoneyama and S. Nishida, "Nonradiative dielectric waveguide T-juctions for millimeter-wave application," *IEEE Trans. Microwave Theory and Tech.*, vol. 33, no. 11, pp. 1239-1241, Nov. 1985.

[11] T. Yoneyama, H. Tamaki, and S. Nishida, "Analysis and measurements of nonradiative dielectric waveguide bends," *IEEE Trans. Microwave Theory and Tech.*, vol. 34, no. 8, pp. 876-882, Aug. 1986.

[12] T. Yoneyama, "Millimeter-wave integrated circuits using nonradiative dielectric waveguide," *IEICE Trans. Electron. (Jananese Ed.).*, vol. J73-C, no. 3, pp. 87-94, Mar. 1990.

[13] F. Xu and K. Wu, "Substrate integrated nonradiative dielectric waveguide structures directly fabricated on printed circuit boards and metallized dielectric layers," *IEEE Trans. Microwave Theory and Tech.*, vol. 59, no. 12, pp. 3076-3086, Dec. 2011.

[14] K. Wu and L. Han, "Hybrid integration technology of planar circuits and NRD-guide for cost-effective microwave and millimeter-wave applications," *IEEE Trans. Microwave Theory and Tech.*, vol. 45, no. 6, pp. 946-954, Jun. 1997.

[15] F. Kuroki, K. Wada, and T. Yoneyama, "Low-loss and small-sized NRD guide ring resonators and their application to channel dropping filter at 60 GHz," *IEICE Trans. Electron.*, vol. E86-C, no. 8, pp. 1601-1606, Aug. 2003.

[16] D. Li, Y. Cassivi, P. Yang, and K. Wu, "Analysis and design of bridged NRD-guide coupler for millimeter-wave applications," *IEEE Trans. Microwave Theory and Tech.*, vol. 53, no. 8, pp. 2546-2551, Aug. 2005.

[17] E. Polat, R. Reese, M. Jost, C. Schuster, M. Nickel, R. Jakoby, and H. Maune, "Tunable liquid crystal filter in nonradiative dielectric waveguide technology at 60 GHz," *IEEE Microw. Wireless Compon. Lett.*, vol. 29, no. 1, pp. 44-46, Jan. 2019.

[18] F. Kuroki, M. Kimura, Y. Murata, and T. Yoneyama, "A compact-sized NRD guide single mixer using band-pass filters at 60 GHz," *IEEE MTT-S Int. Microw. Symp. Dig.*, pp. 2091-2094, Jun. 2005.

[19] F. Kuroki, A. Miyamae, and T. Yoneyama, "Flexible transmission line using high permittivity LSE-NRD guide at 60 GHz," *IEICE Trans. Electron.*, vol. 87, no. 12, pp. 7-2195, Dec. 2004.

[20] F. Kuroki, S. Siunke, and T. Yoneyama, "Modeling of NRD guide beam lead diode devices for millimeter-wave applications," *IEEE Int. Symp. Electron Devices Microw. Optoelectron. Appl.*, pp. 229-233, Nov. 2003.

[21] F. Kuroki, S. Nakamura, T. Fukuchi, and T. Yoneyama, "NRD guide pin diode devices for automotive radar at 77 GHz," *IEICE Trans. Electron.*, vol. 86, no. 2, pp. 199-205, Feb. 2003.

[22] F. Kuroki, S. Shinke, E. Suematsu, H. Sato, and T. Yoneyama, "Wireless multi-channel TV-signal distribution system by using NRD guide transmitter and receiver at 60 GHz," *IEEE MTT-S Int. Microw. Symp. Dig.*, pp. 1813-1816, May 2001.

[23] F. Kuroki, M. Sugioka, S. Matsukawa, K. Ikeda, and T. Yoneyama, "High speed ASK transceiver based on the NRD-guide technology at 60 GHz band," *IEEE Trans. Microw. Theory Techn.*, vol. 46, no. 6, pp. 806-810, Jun. 1998.

[24] F. Kuroki, K. Ikeda, M. Sugioka, S. Matsukara, and T. Yoneyama, "High speed PCM transceiver based on the NRD guide technologies at 60 GHz band," *Proc. Millim. Waves, Top. Symp.*, pp. 119-122, Jul. 1997.

[25] F. Kuroki, Y. Murata, and T. Yoneyama, "A filter-based NRD-guide duplexer with low-loss and high-isolation for wireless broad-band asymmetric digital subscriber line at 60 GHz," *IEEE 34th Eur. Microw. Conf.*, vol. 3, pp. 1281-1284, Oct. 2004.

[26] L. Xu, S. Lin, L. Qi, and Y. Luo, "Theoretical and experimental research on nonradiative dielectric waveguide directional couplers," *Int. J. Infrared Millimeter Waves*, vol. 9, no. 3pp. 265- 372. Mar. 1988.

[27] J. C. Olivier and J. A. G. Malherbe, “Characteristics of coupled non-radiative dielectric waveguide,” *Trans. South Afr. Inst. Electr. Eng.*, vol. 78, no. 2, pp. 43-45, Dec. 1987.

[28] J. A. G. Malherbe and J. C. Olivier, “A bandstop filter constructed in coupled nonradiative dielectric waveguide,” *IEEE Trans. Microwave Theory Tech.*, vol. 34, no. 12, pp. 1408-1412, Dec. 1986.

[29] T. Yoneyama and S. Nishida, “Nonradiative dielectric waveguide circuit components," Int. J. Infrared Millimeter Waves,” *Int. J. Infrared Millimeter Waves*, vol. 4, no. 3, pp. 439-449, May 1983.

[30] T. Yoneyama, F. Kuroki, and S. Nishida, “Design of nonradiative dielectric waveguide filter,” *IEEE/MTT-S Int. Microwave Symp. Digest*, vol. 32, no. 12, pp. 243-244, Dec. 1984.

[31] Y. Ping and M. Jingfeng, “An investigation of NRD waveguide grating,” *IEEE/MTTS Int. Microwave Symp. Digest*, vol. 1, pp. 499-502, June 1989.

[32] T. Yoneyama, S. Nishida, and F. Kuroki, “Experimental design of millimeter-wave nonradiative dielectric waveguide filters,” *Electron. Commun. Jpn. Part 1*, vol. 69, no. 5, pp. 83-89, 1986.

[33] K. Solbach, “The fabrication of dielectric image lines using casting resins and the properties of the lines in the millimeter-wave range,” *IEEE Trans. Microwave Theory Tech.*, vol. 24, no. 11, pp. 879-881, Nov. 1976.

[34] J. A. G. Malherbe, J. H. Cloete, and I. E. Losch, “A transition from rectangular to non-radiating dielectric waveguide,” *IEEE Trans. Microwave Theory Tech.*, vol. 36, no. 6, pp. 539-543, Jun. 1985.

[35] T. Yoneyama, “Millimeter-wave transmitter and receiver using the nonradiative dielectric waveguide,” *IEEE/MTT-S Int. Microwave Symp. Digest*, vol. 3, pp. 1083-1086, June 1989.

[36] H. Yoshinaga and T. Yoneyama, “Design and fabrication of a nonradiative dielectric circulator,” *IEEE Trans. Microwave Theory Tech.*, vol. 36, no. 11, pp. 1526-1529, Nov. 1988.

[37] A. C. Csar and R. F. Souza, "Dispersion in anisotropic NRD waveguide," *IEEE/MTT-S Int. Microwave Symp. Digest*, vol. 3, pp. 1271-1272, June 1989.

[38] J. A. G. Malherbe, "The design of a slot array in non-radiating dielectric waveguide, Part I: Theory," *IEEE Trans. Antennas Propagat.*, vol. 32, no. 12, pp. 1335-1340, Dec. 1984.

[39] J. A .G. Malherbe and H. F. V. Boshoff, "Planar slot array fed by coupled dielectric lines in a metal waveguide," *IEEE Int. Symp. Digest Antennas Propagat.*, vol. 1, pp. 372-375, June 1987.

[40] A. Sanchez and A. A. Oliner, "Microwave network analysis of a leaky-wave structure in non-radiative dielectric waveguide," *IEEE/MTT-S Int. Microwave Symp. Digest*, pp. 118-120, May 1984.

[41] A. Sanchez and A. A. Oliner, "Accurate theory for a new leaky-wave antenna for millimeter waves using non-radiative dielectric waveguide," *Radio Sci.*, vol. 19, no. 5, pp. 1225-1228, Sep. 1984.

[42] A. Sanchez and A. A. Oliner, "A new leaky waveguide for millimeter waves using nonradiative dielectric (NRD) waveguide - Part I: Accurate theory," *IEEE Trans. Micro. Theory Tech.*, vol. 35, no. 8, pp. 737-747, Aug. 1987.

[43] J. A. G. Malherbe, "An integrated antenna for non-radiative dielectric waveguide," *IEICE proceeding series*, pp. 69-72, Aug. 1985.

[44] C. E. Tong, R. Blundell, and M. Carter, "An NRD fed dielectric rod antenna for the short millimeter wave band," *Int. J. Infrared Millimeter Waves*, vol. 10, no. 9. pp. 1153-1163, Sep. 1989.

[45] L. Han, Ke Wu, and R.G. Bosisio, "An integrated transition of microstrip to nonradiative dielectric waveguide for microwave and millimeter-wave circuits," *IEEE Trans. Microwave Theory and Tech.*, vol. 44, no. 7, pp. 1091-1096, July 1996.

[46] C.D. Nallo, F. Ferezza, A. Galli, and P. Lampariello, "Comparative modal analysis of NRD parallelepiped dielectric resonators," *Int. j. infrared millim. waves*, vol. 17 no. 8, pp. 1403-1418, March 1996.

[47] M. Davidowitz, "A model for slot-coupled nonradiative dielectric waveguide and microstrip line," *Int. j. microw. millim.*, vol. 7, no. 5, pp. 388-396, July 1997.

[48] J. Huang, K. Wu, F. Kuroki, and T. Yoneyama, "Filter-like design and optimization of NRD-guide mode suppressors," *IEEE MTT-S Int. Microw. Symp. Dig.*, pp. 995-998, May 1996.

[49] J. Rodrigues , V. Almeida, "Geometric optimization of radiation pressure in dielectric waveguides," *OSA Cont.*, vol. 2, no. 4, pp. 1188-1197, 2019.

[50] J. Byun, I. Park, "Design of dielectric waveguide filters using topology optimization technique," *IEEE Trans. on Magnet.*, vol. 43, no. 4, pp. 1573-1576, 2007.

[51] J. Jung, "Optimal design of dielectric-loaded surface plasmon polariton waveguide with genetic algorithm," *Journal of the Optical Society of Korea*, vol. 14, no. 3, pp. 277-281, 2010.

[52] M. Kaliberda, S. Pogarsky, L. Kaliberda, "SLL Reduction in Planar Dielectric Waveguide with Graphene Strips Using Genetic Algorithm," *2021 15th European Conference on Antennas and Propagation (EuCAP)*, pp. 1-5, 2021.

[53] C. Petrescu, L. Ferariu, "Mode Analysis In Planar Dielectric-Conductor Waveguides Using Genetic Algorithms," *2020 International Conference and Exposition on Electrical And Power Engineering (EPE)*, pp. 259-264, 2020.

[54] R. Shiratori, M. Nakata, K. Hayashi, T. Baba, "Particle swarm optimization of silicon photonic crystal waveguide transition," *Opt. Lett.*, vol. 46, no. 8, pp. 1904-1907, 2021.

[55] J. Avad, M. Demirtaş, N. Perkgöz, F. Ay, "Realistic approach for designing a single-mode Y-branch for weakly guiding material system using particle swarm algorithm," *Opti. and Quant. Elec.*, vol. 52, no. 2, pp. 1-10, 2020.

[56] D. Marcuse, "Length optimization of an S-shaped transition between offset optical waveguides," *Appl. opt.*, vol. 17, no. 5, pp. 763-768, 1978.

[57] P. Wang, R. Menon, "Optimization of generalized dielectric nanostructures for enhanced light trapping in thin-film photovoltaics via boosting the local density of optical states," *Opt. Exp.*, vol. 22, no. 101, pp. A99-A110, 2014.

[58] C. Pan, Z. Liu, Y. Pang, X. Zheng, H. Cai, Y. Zhang, Z. Huang, "Design of a high-performance in-coupling grating using differential evolution algorithm for waveguide display," *Opt. Exp.*, vol. 26, no. 20, pp. 26646-26662, 2018.

[59] L. Sanchis, A. Håkansson, D. López-Zanón, J. Bravo-Abad, J. Sánchez-Dehesa, "Integrated optical devices design by genetic algorithm," *Opt. Exp.*, vol. 84, no. 22, pp. 4460-4462, 2004.

[60] S. Jafar-Zanjani, S. Inampudi, H. Mosallaei, "Adaptive genetic algorithm for optical metasurfaces design," *Sci. Rep.*, vol. 8, no. 1, pp. 1-8, 2018.

[61] P. Sanchis, P. Villalba, F. Cuesta, A. Håkansson, A. Griol, JV. Galán, A. Brimont, J. Martí, "Highly efficient crossing structure for silicon-on-insulator waveguides," *Opt. Lett.*, vol. 34, no. 18, pp. 2760-2762, 2009.

[62] R. Coccioli, G. Pelosi, S. Selleri, "Optimization of bends in rectangular waveguide by a finite-element genetic-algorithm procedure," *Microw. Opt. Technol. Lett.*, vol. 16, no. 5, pp. 287-290, 1997.

[63] A. Iguchi, Y. Tsuji, T. Yasui, K. Hirayama, "Efficient topology optimization of optical waveguide devices utilizing semi-vectorial finite-difference beam propagation method," *Opt. Express.*, vol. 25, no. 23, pp. 28210-28222, 2017.

[64] A. Iguchi, Y. Tsuji, T. Yasui, K. Hirayama, "Topology optimization of optical waveguide devices based on beam propagation method with sensitivity analysis," *J. Light. Technol.*, vol. 34, no. 18, pp. 4214-4220, 2016.

[65] A. Iguchi, Y. Tsuji, T. Yasui, K. Hirayama, "Efficient shape and topology optimization based on sensitivity analysis for optical waveguide devices utilizing full-vectorial BPM," *J. Light. Technol.*, vol. 38, no. 8, pp. 2328-2335, 2020.

[66] P. Sanchis, P. Villalba, F. Cuesta, A. Håkansson, A. Griol, JV. Galán, A. Brimont, J. Martí, "Highly efficient crossing structure for silicon-on-insulator waveguides," *Opt. Lett.*, vol. 34, no. 18, pp. 2760-2762, 2009.

[67] M. Panduro, C. Brizuela, "Comparative analysis of the performance of GA, PSO and DE for circular antenna arrays," *IEEE Antennas and Propagation Society International Symposium*, pp. 1-4, June 2009.

[68] M. Panduro, "Design of coherently radiating structures in a linear array geometry using genetic algorithms," *Int. J. of Electron. and Commun.*, vol. 61, no. 8, pp. 515-520, 2007.

[69] S. Jafar-Zanjani, S. Inampudi, H. Mosallaei, "Adaptive genetic algorithm for optical metasurfaces design," *Sci. Rep.*, vol. 8, no. 1, pp. 1-6, 2018.

[70] L. Sanchis, A. Håkansson, D. López-Zanón, J. Bravo-Abad, J. Sánchez-Dehesa, "Integrated optical devices design by genetic algorithm," *Appl. Phys. Lett.*, vol. 84, no. 22, pp. 4460-4462, 2004.

[71] R. Coccioli, G. Pelosi, S. Selleri, "Optimization of bends in rectangular waveguide by a finite element genetic algorithm procedure," *Microw. Opt. Technol. Lett.*, vol. 16, no. 5, pp. 287-290, 1997.

[72] J. Jung, "Optimal design of plasmonic waveguide using multi objective genetic algorithm," *Opt. Eng.*, vol. 55, no. 1, pp. 017103- 017105, 2016.

[73] P. Fu, L. Shu-Cheng, T. Po-Cheng, L. Kuang, and W. Pei-Kuen, "Optimization for gold nanostructure-based surface plasmon biosensors using a microgenetic algorithm," *ACS Photon.*, vol. 5, no. 6, pp. 2320-2327, 2018.

[74] J. Jiang, J. Cai, G. Nordin, L. Li, "Parallel microgenetic algorithm design for photonic crystal and waveguide structures," *Opt. Lett.*, vol. 28, no. 23, pp. 2381-2383, 2003.

[75] G. Nordin, J. Jiang, S. Kim, J. Cai, "Microgenetic-algorithm-based design of combined conventional waveguide and photonic crystal devices in photonic crystal materials and devices," *Int. j. opt. photonics.*, vol. 5000, pp. 152-160, 2003.

[76] A. Iguchi, Y. Tsuji, T. Yasui, and K. Hirayama, "Efficient topology optimization of optical waveguide devices utilizing semi-vectorial finite-difference

beam propagation method," *Opt. Express,* vol. 25, no. 23, pp. 28210-28222, Nov. 2017.

[77] J. C. Mak, C. Sideris, J. Jeong, A. Hajimiri, and J. K. Poon, "Binary particle swarm optimized 2×2 power splitters in a standard foundry silicon photonic platform," *Opt. lett.,* vol. 41, no. 16, pp. 3868-3871, Aug. 2016.

[78] W. Chen, B. Zhang, P. Wang, S. Dai, W. Liang, H. Li, Q. Fu, J. Li, Y. Li, T. Dai, and H. Yu, "Ultra-compact and low-loss silicon polarization beam splitter using a particle-swarm-optimized counter-tapered coupler," *Opt. express,* vol. 28, no. 21, pp. 30701-30709, Oct. 2020.

[79] T. Fujisawa and K. Saitoh, "Ultrasmall two-mode dividers based on mosaic structure designed by direct-binary-search algorithm aided by artificial neural network," *IEEE Opto-Electronics and Communications Conference,* pp. 1-3, Oct. 2020.

[80] T. Fujisawa and K. Saitoh, "Bayesian direct-binary-search algorithm for the efficient design of mosaic-based power splitters," *OSA Cont.,* vol. 4, no. 4, pp. 1258-1270, Apr. 2021.

[81] W. Chang, L. Lu, X. Ren, D. Li, Z. Pan, M. Cheng, D. Liu, and M. Zhang, "Ultracompact dual-mode waveguide crossing based on subwavelength multimode-interference couplers," *Photonics Research,* vol. 6, no. 7, pp. 660-665, June 2018.

[82] Y. Xu, H. Ma, T. Xie, J. Yang, and Z. Zhang, "Ultra-Compact Power Splitters with Low Loss in Arbitrary Direction Based on Inverse Design Method," *Photonics,* vol. 8, no. 11, pp. 516-526, Nov. 2021.

[83] W. Chang, L. Lu, X. Ren, L. Lu, M. Cheng, D. Liu, and M. Zhang, "An ultra-compact multimode waveguide crossing based on subwavelength asymmetric Y-junction," *IEEE Photon.,* vol. 10, no. 4, pp. 1-8, June 2018.

[84] J. H. Holland, "Adaptation in Natural and Artificial Systems," University of Michigan Ann Arbor, Michigan: *MIT Press,* 1992.

[85] R. Storn and K. Price, "Differential evolution–a simple and efficient heuristic for global optimization over continuous spaces," *J. Glob. Optim.,* vol. 11, no. 4, pp. 341-59, Dec. 1997.

[86] Z. W. Geem, J. H. Kim, and G. V. Loganathan, "A new heuristic optimization algorithm: Harmony search," *Simulation,* vol. 76, no. 2, pp. 60-68, Feb. 2001.

[87] R. Eberhart, and J. Kennedy, "A new optimizer using particle swarm theory," *IEEE Proceedings of the Sixth International Symposium on Micro Machine and Human Science,* pp. 39-43, Oct. 1995.

[88] X. S. Yang, "Firefly algorithms for multimodal optimization," *International Symposium on Stochastic Algorithms,* pp. 169-178, Oct. 2009.

[89] V. Dmitriev, M. N. Kawakatsu, and F. J. M. de Souza, "Compact three-port optical two-dimensional photonic crystal-based circulator of W-format," *Opt. Lett.,* vol. 37, no. 15, pp. 3192–3194, Aug. 2012.

[90] S. John, "Strong localization of photons in certain disordered dielectric superlattices," *Phys. Rev. Lett.,* vol. 58, pp. 2486–2489, Jun. 1987.

[91] Z. Wang and S. Fan, "Optical circulators in two-dimensional magnetooptical photonic crystals," *Opt. Lett.,* vol. 15, pp. 1989–1991, Aug. 2005.

[92] E. Yablonovitch, "Inhitited spontaneous emission in solid-state physics and electronics," *Phys. Rev. Lett.,* vol. 58, pp. 2059–2062, May 1987.

[93] D. S. Sundar, C. Umamaheswari, T. Sridarshini, M. Karthikeyan, R. Sitharthan, A. S. Raja, and M. F. Carrasco, "Compact four-port circulator based on 2D photonic crystals with a 90° rotation of the light wave for photonic integrated circuits applications," *Laser Phys.,* vol. 29, no. 6, p. 066201, Jun. 2019.

[94] Y. Wang, D. Zhang, S. Xu, B. Xu, Z. Dong, and Q. Xue, "Microwavefrequency experiment validation of a novel magneto-photonic crystals circulator," *IEEE Photon. J.,* vol. 10, no. 3, Feb. 2018,

[95] Y. Wang, D. Zhang, S. Xu, B. Xu, and Z. Dong, "H-plane cross-shaped waveguide circulator in magneto-photonic crystals with five ferrite posts," *Chin. Opt. Lett.,* vol. 15, no. 10, pp. 1116011-1–1116011-4, Nov. 2017.

[96] F. Fan, S.-J. Chang, C. Niu, Y. Hou, and X.-H. Wang, "Magnetically tunable silicon ferrite photonic crystals for terahertz circulator," *Opt. Commun.,* vol. 285, no. 18, pp. 3763–3769, Aug. 2012.

[97] Y. Wang, B. Xu, D. Zhang, W. He, H. Ian, "Compact photonic-crystals based isolator using Ni–Zn gyromagnetic ferrite posts," *Appl. Sci.,* vol. 11, no. 3, July 2021.

[98] S. A. Oliver, P. M. Zavracky, N. E. McGruer, and R. Schmidt, "A monolithic single-crystal yttrium iron garnet/silicon X-band circulator," *IEEE. Microw. Guided Wave Lett.,* vol. 7, no. 8, pp. 234–239, Aug. 1997.

[99] Y. Akaiwa, "Operation modes of a waveguide Y circulator," *IEEE Trans. Microw. Theory Techn.,* vol. MTT-22, no. 11, pp. 954–960, Nov. 1974.

[100] S. W. Y. Mung and W. S. Chan, "Active three-way circulator using transistor feedback network," *IEEE Microw. Wireless Compon. Lett.,* vol. 27, no. 5, pp. 476–478, May 2017.

[101] S. Wang, C.-H. Lee, and Y.-B. Wu, "Fully integrated 10-GHz active circulator and quasi-circulator using bridged-T networks in standard CMOS," *IEEE Trans. Very Large Scale Integr. Syst.,* vol. 24, no. 10, pp. 3184–3192, Oct. 2016.

[102] P. Pintus, D. Huang, C. Zhang, Y. Shoji, T. Mizumoto, and J. E. Bowers, "Microring-based optical isolator and circulator with integrated electromagnet for silicon photonics," *J. Lightw. Technol.,* vol. 35, no. 8, pp. 1429–1437, Apr. 15, 2017.

[103] P. Pintus, F. Di Pasquale, and J. E. Bowers, "Integrated TE and TM optical circulators on ultra-low-loss silicon nitride platform," *Opt. Express,* vol. 21, no. 4, pp. 5041–5052, Feb. 2013.

[104] E. J. Denlinger, "Design of partial height ferrite waveguide circulators," *IEEE Trans. Microw. Theory Techn.,* vol. MTT-22, no. 8, pp. 810–813, Aug. 1974.

[105] M. Muraguchi, K. Araki, Y. Naito, "A new type of isolator for millimeter-wave integrated circuits using a nonreciprocal traveling-wave resonator," *IEEE Trans. Microw. Theory Techn.,* vol. 11, no. 30, pp. 1867-73, Nov. 1982.

[106] Y. Wang, B. Xu, D. Zhang, S. Xu, Z. Dong, X. Zeng, X. Lu, J. Pei, "Magneto-optical isolator based on ultra-wideband photonic crystals waveguide for 5G communication system," *Crystals,* vol. 11, no. 2, Oct. 2019.

[107] Y. Wang, B. Xu, D. Zhang, W. He, H. Ian, "Compact Photonic-Crystals Based Isolator Using Ni–Zn Gyromagnetic Ferrite Posts," *Appl. Sci.,* vol. 13, no. 11, Jul. 2021.

[108] M. Noferesti, T. Djerafi, "A tunable ferrite isolator for 30 GHz millimeter-wave applications," *IEEE Trans. Magn.,* vol. 7, no. 57, Apr. 2021.

[109] K. Fang, Z. Yu, V. Liu, S. Fan, "Ultracompact nonreciprocal optical isolator based on guided resonance in a magneto-optical photonic crystal slab," *Opt. Lett.,* vol. 21, no. 36, pp. 4254–4256, Nov. 2021.

[110] B. Rahman, F. Fernandez, J. Davies, "Review of finite element methods for microwave and optical waveguides," *Proceedings of the IEEE,* vol. 79, no. 10, pp. 1442-1448, 1991.

[111] JM. Jin, "The Finite Element Method in Electromagnetics," *Wiley-IEEE Press,* 2014.

[112] Y. Tsuji, M. Koshiba, "Finite element method using port truncation by perfectly matched layer boundary conditions for optical waveguide discontinuity problems," *J. Light. Technol.,* vol. 20, no. 3, pp. 463-468, 2002.

[113] A. Taflove, SC. Hagness, "Computational electromagnetics – the finite difference time-domain method," *Artech House,* 2005.

[114] C. Mroczkowski, WK. Gwarek, "Microwave Circuits Described by Two-Dimensional Vector Wave Equation and their Analysis by FD-TD Method," *21st European Microwave Conference,* pp. 866-871, 1991.

[115] W. Gwarek, T. Morawski, C. Mroczkowski, "Application of the FD-TD method to the analysis of circuits described by the two-dimensional vector wave equation," *IEEE Trans. Microw. Theory Tech.,* vol. 41, no. 2, pp. 311-317, 1993.

[116] L. Yechou, A. Tribak, M. Kacim, A. Serroukh, J. Tarhzaz, "Waveguide High-pass filter Design and 2D-FDTD Analysis method," *Revue Méditerranéenne des Télécommunications,* vol. 9, no. 1, 2019.

[117] G. Ramzi, T. Hichem, G. Ali, "2-D FDFD method analysis to NRD-guide bandpass filter design," *IEEE 1st International Conference on Advanced Technologies for Signal and Image Processing,* pp. 560-563, 2014.

[118] S. Luo, A. Z. Chen, "A New 2D FDTD Method for Solving 3D Guided-wave Structures," *IEEE MTT-S International Microwave Symposium Digest,* pp. 1473-1476, 2006.

[119] N. Mehennaoui, A. Merzouki, D. Slimani, "2D-FDTD-UPML simulation of wave propagation on dispersive media," *IEEE 3rd International Conference on Control, Engineering Information Technology,* pp. 1-5, 2015.

[120] R.s El Shamy, M. Swillam, S. Obayya, "Full 3D electromagnetic wave analysis using 2D simulation," *IEEE International Applied Computational Electromagnetics Society Symposium,* pp. 1-2, 2017.

Acknowledgements

I would like to express my deepest gratitude to my honorable supervisor, Prof. Yasuhide Tsuji, for his endless efforts and for advising me during this study. Their knowledge in this research field, as well as their encouragement in my research at Muroran Institute of Technology, were critical factors in my success with this thesis.

I am especially grateful to Prof. Tatsuya Kashiwa, the Department of Information and Communication Engineering, Kitami Institute of Technology, Prof. Akito Iguchi, the Department of Information and Electronic Engineering, Muroran Institute of Technology, and Prof. Keita Morimoto, the Department of Electronics and Computer Science, University of Hyogo, for their helpful discussions and suggestions.

I would like to thanks my teachers who have taught me in my education carrier Prof. Xiong Han the Department of Microelectronics and Communication Engineering, Chongqing university, China, Prof. Muhammad Ali Qureshi, and Prof. Abdul Aziz the Department of Information and Communication Engineering, Islamia University Bahawalpur, Pakistan. I would also like to express my gratitude to Muroran Institute of Technology, the Japanese government, and the Ministry of Education, Culture, Sports, Science and Technology (MEXT) for providing financial assistance during my doctoral studies. I would like to thank all of my laboratory members and friends who always help me and support me in this study period.

I am eternally grateful to my father, mother, and my whole family for their love, support, and encouragement throughout my educational career. May Allah bless my parents with a long, beautiful, healthy life. Finally, this thesis is dedicated to my parents.

List of Author's Publication

Peer-Reviewed Papers

- **T. Bashir**, K. Morimoto, A. Iguchi, Y. Tsuji, T. Kashiwa, and S. Nishiwaki, "Analysis of NRD Guide Devices Using Rigorous Two-Dimensional Full-Vectorial FDTD Method," *Microwave and Optical Technology Letter*, Nov. 2022, (doi:10.1002/mop.33510.).

- **T. Bashir**, K. Morimoto, A. Iguchi, Y. Tsuji, and T. Kashiwa, "Mosaic Based Optimization of NRD Guide Devices Using Binary Evolutionary Approaches and 2D-FVFEM," *IEEE ACCESS*, vol. 10, pp. 60682-60695, June. 2022.

- **T. Bashir**, K. Morimoto, A. Iguchi, Y. Tsuji, T. Kashiwa, and S. Nishiwaki, "Optimal design of broadband non-radiative dielectric guide devices using binary genetic algorithm and 2D-FVFEM," *International Journal of Numerical Modeling, Electronic Network, Devices and Fields*, vol. 35, no. 4, Jan. 2022.

- **T. Bashir**, K. Morimoto, A. Iguchi, Y. Tsuji, T. Kashiwa, and S. Nishiwaki, "Optimal design of NRD guide devices using 2D full-vectorial finite element method," *IEICE Electron. Express,* vol. 18, no. 15, Art. no. 20210243, Aug. 2021.

Conference Papers

- **T. Bashir**, K. Morimoto, A. Iguchi, Y. Tsuji, T. Kashiwa, and S. Nishiwaki, "Optimal Design of NRD Isolator Using Ni-Zn Ferrite Post

for Millimeter-Wave Integrated Circuit Applications," Asia-Pacific Microwave Conference (APMC), Yokohama, Japan, to be published 2022.

- **T. Bashir**, A. Iguchi, Y. Tsuji, and T. Kashiwa, "Design of Mosaic-like NRD Guide Devices with Magnetic Material," IEICE Technical Report, Vol. 122, no. 120, pp. 122-126, June 2022.

- **T. Bashir**, K. Morimoto, A. Iguchi, Y. Tsuji, T. Kashiwa, and S. Nishiwaki, "Optimal Design of 90°-Bend in NRD Guide Using DBS Algorithm and 2D-FVFEM," IEEE International Symposium Antennas and Propagation USNC-URSI Radio Science Meeting (APS/URSI), Singapore, Dec. 2021.

Conference Presentations

- **T. Bashir**, K. Morimoto, A. Iguchi, Y. Tsuji, and T. Kashiwa, "Optimal Design of NRD Non-Reciprocal Guide Device for Millimeter-Wave Applications," Chitose International Forum on Science and Technology, Hokkaido, Japan, 2022.

- **T. Bashir**, K. Morimoto, A. Iguchi, Y. Tsuji, and T. Kashiwa, "Comparative Study of Optimization Method for Design of NRD Guide Devices with Mosaic-like Structure," Progress In Electromagnetics Research Symposium, Hangzhou, China, 2021.